MOSQUITO FLIGHT ADAPTATIONS TO PARTICULATE ENVIRONMENTS

A Dissertation
Presented to
The Academic Faculty

by

Andrew Keith Dickerson

In Partial Fulfillment
of the Requirements for the Degree
Doctor of Philosophy in the
Woodruff School of Mechanical Engineering

Georgia Institute of Technology
May 2014

MOSQUITO FLIGHT ADAPTATIONS TO PARTICULATE ENVIRONMENTS

Approved by:

Professor David Hu, Advisor
Woodruff School of Mechanical Engineering
Georgia Institute of Technology

Professor G. Paul Neitzel
School of Mechanical Engineering
Georgia Institute of Technology

Professor Robert Dudley
Department of Integrative Biology
University of California at Berkeley

Professor Alexander Alexeev
School of Mechanical Engineering
Georgia Institute of Technology

Professor Athanasios Nenes
School of Earth and Atmospheric Sciences
Georgia Institute of Technology

Date Approved: 20 December 2013

To my grandfathers,

Jack B. Dickerson *&* **Dr. John L. Ruehle***,*

whose character, courage, and achievements inspired my academic path.

May my intellectual endeavors honor their legacy.

PREFACE

Why mosquitoes? Brainstorming sessions are commonplace in the Hu lab as we search for the next story to tell. Towards the close of my first year in graduate school, Dr. Hu and I were participating in such a session when he raised a burning question, "Do you think insects can fly in the rain?" I did not realize at this moment the extent to which I would build appreciation and a relationship with the humble mosquito, seemingly the most obnoxious insect to ever evolve. We set about to determine the ideal model organism and the feasibility of a study that would answer the rain-insect mystery. The model organism needed to be easily raised (or attained), active, and scientifically relevant. Our journey led us to the CDC's entomology department, which raises mosquitoes and not much else. Fortunately, the mosquito is the perfect model organism. The mosquito is easily excitable, and scientists are very interested in any result pertaining to the survival and behavior of the world's most dangerous animal. In the CDC's labs we were given a mesh cage full of mosquitoes promised to be disease free. Armed with a high-speed camera and dropper, we took the first insect-drop impact footage known to man. Three years and four articles later, the CDC is still anxious to provide as many mosquitoes as we can use.

ACKNOWLEDGEMENTS

To David Hu, for his endless creativity, and pushing me to go places I did not want to go, but was glad I went; without him this work and my degree would not have been possible.

To Jaime Dickerson, my wife, for always asking me about my day and comforting me when the answer was not positive; it takes a special woman to be married to a doctoral student.

To Tracy and Kim Dickerson, my parents, for a better childhood than I deserved and for supporting any venture I pursued.

To Hamid Marvi, Nathan Mlot, Guillermo Amador, James Black, and Jeff Fisher for your light-hearted banter and for making the work more tolerable.

To Edward Keene and Timothy Dietz, for your company and support during my first semesters at Georgia Tech.

To Peter Shankles, for spending hours hitting styrofoam with raindrops and collecting most of the videos that made our first publication a success, and for your contributions on the fog project for two semesters.

To Bruce Berry Jr., for your tireless efforts on the fog project for two semesters.

To Nihar Madhavan, for an enthusiastic high school researcher, filming mosquitoes being hit by raindrops, and for introducing Tracker to the lab.

To Luke Telljohann, Sam Beadles, and Courtney Clement, for allowing me to mentor you and for experimental contributions. I hope Westminster High School continues to send good students to the lab.

To Caitlin Moyer and Lee-Ellen Thornton for first observing mosquitoes cannot fly in dense fog.

To Paul Foster, for his wise guidance on a number of issues.

To Laura O'Farrell for laboratory assistance with rats, rabbits, cats, and the like.

To Rob DeBernard, for capturing the first dog videos and teaching me how to use a high-speed camera.

To Tim Nowack, for his many beautiful photographs and creative means.

To Paul Howell, and the rest at the CDC's entomology department, for the endless supply of mosquitoes.

To Peter Kottke, for giving me my first taste of thermodynamics, fluid mechanics, and heat transfer. I may not have been an ME student without his class.

To God, for steering me on His course and for giving me countless blessings, not the least of which is patience, endless hope for a marvelous future, and a Savior.

I offer my heartfelt thanks.

TABLE OF CONTENTS

LIST OF TABLES

LIST OF FIGURES

SUMMARY

Flying insects face challenging conditions such as rainfall, fog, and dew. In this theoretical and experimental thesis, we investigate the survival mechanisms of the mosquito, *Anopheles*, through particles of various size. Large particles such as falling raindrops can weigh up to fifty times a mosquito. Mosquitoes survive such impacts by virtue of their low mass and strong exoskeleton. Smaller particle sizes, as present in fog and insecticide, pose the greatest danger. Mosquitoes cannot fly through seemingly innocuous household humidifier fog or other gases with twice the density of air. Upon landing, fog accumulates on the mosquito body and wings, which in small quantities can be shaken off in the manner of a wet dog. Large amounts of dew on the wings create a coalescence cascade ultimately folding the wings into taco shapes, which are difficult to dry. The insights gained in this study will inform the nascent field of flapping micro-aerial vehicles.

CHAPTER I

INTRODUCTION

"For wisdom will enter your heart, and knowledge will be pleasant to your soul. Discretion will protect you, and understanding will guard you." -Proverbs 2:10-11 (New International Version)

1.1 Motivation

Man has marveled at insects for centuries. Their number, richness in form and function, and robustness is unmatched. They are worthy of our attention and still have so much to teach us. The motive behind this thesis is twofold: technological and biological. Technological advancements in manufacturing and control systems means that robots are becoming smaller, even at the scale of insects. Micro-aerial vehicles (MAVs) range in size from 10 cm down to a few millimeters[1–7]. These small flying machines are appealing for the role they will play in search-and-rescue and military operations. In parallel with the engineering of MAVs, vigorous efforts continue to be made into understanding flight in the natural world, such as by birds and insects[8–11]. Much progress has been made in understanding straight-path flight in unidirectional flow. However, much remains to be understood about the abilities of birds and insects to fly through complex conditions such as wind and rain. Such knowledge has implications for ecology in terms of understanding the evolution of animals in rain forests and near waterfalls. The adaptations of these animals may also serve engineering via biological inspiration for the design of robust MAVs.

An understanding of how flying insects survive perturbations from impacting particles will also lead to new biophysics that incorporates both mesoscale biology and hydrodynamics. Organisms are multi-degree-of-freedom, hierarchically organized, nonlinear systems.

They respond to their environments through a combination of feedback between their visual, chemical, and strain-based sensory systems[8,12]. The notion of robustness emerges from the combination of their muscular and neural connections, and the physical structure of the organisms including form, material, and surface properties. It remains unknown which parts of these intricate systems are programmed to respond to varying environmental conditions such as particle collisions. Flying insects are particularly specialized organisms. They thrive in environments latent with perturbations[13], but remain very capable flyers. A crucial part of the ecosystem, flying insects act as pollination catalysts and food for larger organisms. Some species, however, are a danger to society, indiscriminately transmitting disease. An understanding of insect locomotion in particle environments will also benefit the arsenal we have to manage flying insects.

1.2 Background & Previous Work

1.2.1 Rain & Drop Impact

One of the technological feats of the twenty-first century is the construction of insect-sized flying robots, made possible by rapidly shrinking manufacturing and electronics[1–7]. These robots have numerous applications such as deployment in swarms for surveillance and search-and-rescue operations. Inspiration for robust and efficient flight is readily found in nature. For millions of years, flying insects have been challenged by in-flight collision with falling drops. Though the insects in **Fig.1** are resting on a solid surface, they provide perspective on how in-flight collisions may appear. Rain of various intensity, dripping from overhanging leaves, dewfall, and splashes from cascades all generate drops that may strike an insect mid-flight[14,15]. A raindrop[16], can have a mass $m_1 = 4 - 100$ mg, radius $R_1 = 1 - 4$ mm, and speed u_1 up to 10 m/s. Their shapes can vary from a sphere for small drops, to flattened shapes for large drops.

Previous studies of bats have shown that rain doubles their energetic cost of flight[17]. Hummingbirds will fly in rain to feed, and can shake off accumulated water mid-flight to

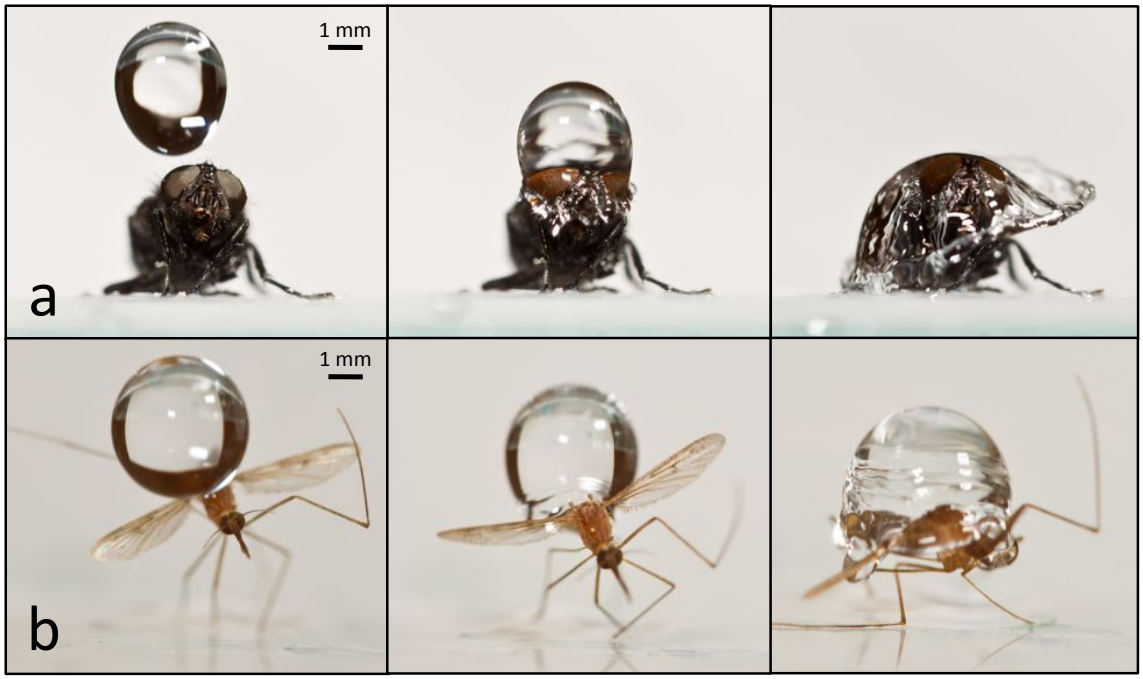

Figure 1: Raindrop impacts upon (a) a house fly, recently deceased and untethered, and (b) a live, tethered mosquito.

reduce the cost of carrying wet feathers[18]. These animals are so large that they will suffer multiple raindrops in a single wingbeat. Such studies are likely not applicable to understanding how insects fly in the rain because of the insect's much smaller size compared with vertebrate flyers.

Many insects such as mosquitoes thrive in wet, humid locations such as the tropics, where it rains often[13]. In rainforests, which encapsulate 40-75% of the species diversity of earth, rainfall occurs daily. Flying insects likely perceive raindrop impacts as in-flight perturbations. There have been many studies of such perturbations, although none have considered the influence of a wetting fluid such as rain. For instance, bees exposed to turbulent air resist rolling instabilities by extending their legs to increase their moment of inertia[19]. Following in-flight perturbation, fruit flies actively re-stabilize themselves by flapping[12,20]. Symmetric wing beats of a rotating insect will dampen insect rotation[21]. Many of these re-stabilizing maneuvers rely upon delaying stall and interacting with wakes

created by flapping wings[22]. They are thus sensitive to the wing's ability to deform under flapping[23]. Altogether, these studies indicate that flying insects are highly maneuverable and able to quickly correct many kinds of perturbations (roll, pitch, yaw). However, such abilities may be affected if the wing is wet or must flap through a field of drops. Thus, to truly gain insight on the ability to fly through rain, we turn to in-flight experiments with wetting drops of fluid.

The remainder of our knowledge of the effect of precipitation is restricted to large aircraft, although they operate upon very different principles from flapping fliers. Field testing on the effects of heavy rain on aircraft[24] confirms that precipitation generally hinders locomotion. Aircraft experience greater drag (2-5%), reduced lift (7-29%), a reduction in stall angle of 1-5°, as measured[25,26] during a rainfall intensity of 100-1000 mm/hr. Aircraft can reduce these losses by using wing designs that can funnel rivulets and control their diameter. These design principles may explain some of the water-repellent features common in birds' wings[27]. However, they clearly do not apply for much smaller fliers such as insects which are closer in size to raindrops.

Although drop impact has been studied for decades[28,29], little is known regarding impact upon a small free body. The closest situations to the one of interest are impact between two drops and impact between a drop and an immovable solid. In the first, several outcomes are possible, including bouncing, coalescence, disruption, and fragmentation. The choice of outcome depends exclusively on drop size, their relative velocity, and degree of offset at collision, known as the impact parameter[30]. Other studies focus on collision of two drops of differing size, viscosity, and surface tension[31]. The topics of Chapters 3 & 4 of this thesis, the impact of a drop upon a small free body, may be considered as the impact between two drops of vastly different viscosity.

Drop impact upon an immoveable solid surface may also be considered as a limiting case of drop impact on a free body. As the free body grows in size to that of a large bird or aircraft, it is clear raindrops will splash upon collision. It is not yet clear, however, where

the splashing threshold lies in terms of free body properties such as density, curvature, and impact speed. Drops striking solid surfaces experience one of multiple modes of impact: deposition, splashing, receding breakup, partial rebound, or complete rebound[29,32]. Mode selection depends upon drop size, speed, impact orientation, as well as properties of the solid such as surface texture and curvature[33–38]. In Chapter 4 of this thesis, we clarify the onset of splashing in terms of free body properties such as density, curvature, and impact speed.

In this thesis, we will focus on small flying insects as model organisms, whose length-scales on the order of the capillary length, make them particularly interesting in their interaction with water surfaces. Most research on water-repellency has centered upon material properties[39,40]. The canonical water-repellent organism is the sacred lotus plant, known as a symbol of purity. During rainstorms, it is self-cleaning by virtue of its hierarchical fractal-like surface that permits drops to remain spherical and roll off easily, by virtue of the associated high contact angles and low contact angle hysteresis[41]. Since then, a flurry of experimental and theoretical efforts have been made to build super-hydrophobic surfaces, and to characterize their abilities theoretically. The insights made have been used to design hydrophobic fabrics and paint, Gore-Tex and Lotusan. However, most of these surfaces are designed to be static. The means by which rapidly moving organisms or devices can repel water while propelling themselves remains unknown. Such understanding is important for building autonomous devices.

Nearly all flying insects are adapted for contact with water. Previous experiments on flying insects through fields of drops were conducted towards the development of insecticides. Such experiments show that many insects possess adaptations to contend with water, including a dense layer of wax-coated hairs that repels water. This layer causes flying insects to be considerably more water-repellent than both aquatic and terrestrial insects[27]. For instance, water drops on mosquitoes have contact angles of approximately 180° on the thorax and 75-95° on the legs and wings[42]. Insect wings, in particular, have evolved

highly specific structures and surface chemistries to attain hydrophobic, and occasionally superhydrophobic, wetting properties that enable macro-scale drop mobility and wing self-cleaning[43–47]. A combination of microscopic surface structure, and a lipid layer, causes drops to spontaneously roll off and carry away contaminants. Altering the surface structure via micro-scale contaminants such as dust, or dissolution of the lipid layer rapidly degrades their ability to stay clean and dry.

1.2.2 Insect wetting properties

Drops much larger than the microstructures on the wing surface will exhibit the Cassie-Baxter wetting state such that the drop sits atop the structures with a thin layer of air underneath[48]. This is a favorable wetting state for the insect, allowing for easy drop removal. When drops are comparable in size to the microstructures, a groove-filling Wenzel-like behavior is observed[49], pinning drops to the surface and decreasing their mobility (**Fig.2**). Small droplet deposition and vapor condensation between hairs are very similar[50], and both ultimately result in a wet insect.

The ability of materials to generate Cassie states is sensitive to contaminants. Altering the wing microstructure by deposition of micro-scale contaminants such as dust rapidly degrades their ability to stay clean and dry. A thin application of a thin layer of Al_2O_3, causes butterfly wings to change from a superhydrophobic state (Cassie-Baxter) to a hydrophilic state (Wenzel). However, a similar coating causes water strider legs to remain superhydrophobic, even under applied water pressure[51]. The water strider's robustness against surfactants may be due to the greater evolutionary pressure these insects face as they walk on water[52,53]. Butterfly wings, in particular, have directional adhesion which aids in shedding drops[54]. The adaptations of these animals suggest a primal relationship between insects and rainfall. It remains unknown how a mosquito's water-repellency is beneficial during high-speed impacts of much larger drops such as rain.

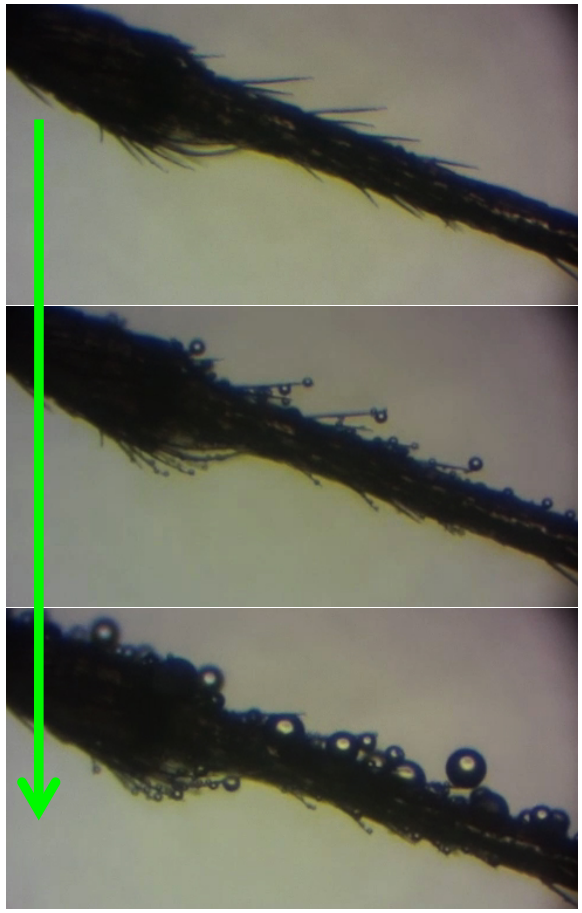

Figure 2: Photo sequence of droplets forming on a mosquito leg through the deposition of 15 μm fog particles.

1.2.3 Fog, Dew, & Insecticide

In many areas of the world, fog is necessary for life. At high altitudes, trees and organisms in "cloud forests" collect much of their water and nutrients from fog[55]. Desert insects such as the Namib beetle and plants such as cacti gather fog in order to drink[56–58]. This is often accomplished using an array of hydrophobic and hydrophilic surfaces to funnel collected water. Fog in natural conditions contains drops of size range $1-10$ microns and concentrations of 100 drops/cm^3.

Airborne particles can broadly be characterized into one of two categories, haze and fog. Fog is defined as providing less than 1 km of visibility[59]; in natural conditions[60] fog consists of small water droplets, in the liquid or frozen state, of size $1-10$ μm in

diameter and concentrations 25 - 100 mg/m^3. These parameters are dependent on altitude. Fog has a bimodal distribution; the larger fog particles close to the ground have an average diameter of 5 μm, whereas the higher altitude particles have a diameter of 0.3 - 0.6 μm. On the other hand, haze consists of 0.2 μm dust and smog particles, with little vertical variation. Fog and haze particle size can be measured much like insecticide particle size, through light scattering and holographic techniques[61,62]. In comparison to natural fogs, insecticides involve drop sizes comparable to that of natural fogs, but of one millionth the density, less than 100 ng/m^3 when dispersed, rendering them invisible.[63]. However, during dispersion, fogs and sprays at output nozzles are very dense and visible.

the primary water source for some plants[58]. Dew condenses on such surfaces because of temperature gradients between air and ground. Poikilothermic insects too will experience such condensation. Such condensation was observed on the semi-aquatic Fisher spider, showing that drops tend to bead up[64]. Little is known on how terrestrial or flying insects cope with dew.

The development of insecticide involves drop size comparable to that of natural fogs, but of much lower density (ounces per acre). Mosquito control methods include intermittent preventative treatment, insecticide-treated nets, indoor residual spraying, chemical larviciding, and insecticide fogging or spraying. The latter technique works by depositing toxins on the insect cuticle, through encounters with airborne particles or insecticide-ridden surfaces. Toxins are carried by water or oil micro-droplets. While these insecticides possess acceptably low toxicity to humans, strict regulations govern their use and application. Spraying and fogging should be done at the peak of adult mosquito activity, which is highly variable among species and requires repetition, which can be expensive. By studying the vulnerabilities of mosquito flight, unforeseen strategies for mosquito mitigation free of insecticides may be found. The chosen model organism in this thesis is the *Anopheles freeborni* mosquito, an established malaria vector. A mosquito's flight performance in arrays of very small drops such as in a dense fog is poorly understood, despite the common use of

insecticide foggers. Little is known of how small particles can affect the insect's air-wing interactions and sensing of its environments.

1.2.4 Insect Flight Sensors

Dense fog has been known to disrupt avian vision and navigation ability[65]. Like birds, insects also use a combination of visual and force-mediated feedback to navigate[66]. Tethered fruit flies and houseflies use an optomotor response to adjust their thrust and torque for visual cues positioned in front of their eyes[67]. Insects without gyroscopes, like the desert locust, employ other means of flight sensing[68,69] such as sensitive hairs on their hind limbs to detect wind direction. The small tortoiseshell butterfly uses its antenna to detect flight speed[70,71], while the hawkmoth vibrates its large antennae to detect Coriolis forces[72]. Mosquitoes rely heavily on olfactory cues to find food and mates[73]. The effect of airborne particles on these sensing systems has not been systematically studied, and sensing systems are very species specific. Only recently has any work been done on how particles affect olfactory sensors on cockroaches[74].

Halteres, small knobbed structures evolved from hind wings, flap with the same frequency as wings and serve several in-flight functions[75–77] (**Fig.3**). Halteres, provide proprioceptive feedback by detecting Coriolis forces and play a crucial role in the neuromuscular circuit generating the wingbeat rhythm in Dipterans[66,78]. By activating the motor neurons of minuscule steering muscles, halteres help regulate wing motion through a reflexive feedback loop with these muscles. Haltere-bearing insects have irregular fields of campaniform sensilla imbedded in their cuticle at the base of the haltere shaft[79]. The architecture of the campaniform structures give them the ability to detect small strains in the cuticle as the haltere flaps. Historically, halteres have been thought to sense inertial, centrifugal, and gravitational forces in addition to Coriolis forces[76].

Mosquito halteres have not been the focus of much investigation, but the function and dynamics of fruit fly halteres has been well studied. In tethered fruit flies, adding mass

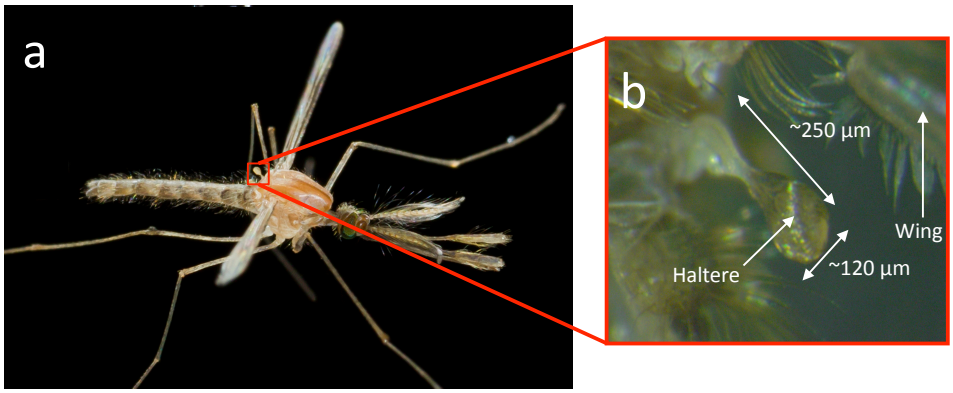

Figure 3: **(a)** An *Anopheles freeborni* mosquito in flight. The location of mosquito's haltere boxed in red. **(b)** A mosquito haltere.

to one haltere using glue acts to reduce peak velocity and amplitude of body saccades[66]. Ablating one fruit fly haltere has the opposite effect by accelerating in-flight maneuvers. In some situations, haltere augmentation results in the adoption of a flapping frequency different from that of the wings[80,81]. Sensory feedback from the haltere is read by the wing control mechanisms on a stroke-by-stroke basis, even in steady flight[82,83], so the effects of haltere augmentation in fruit flies may be due to the disruption in synchronous wing-haltere signals[66]. Houseflies with halteres removed show a complete lack of control over flight[75].

1.2.5 Folding Wings & Capillarity

Folding is a way to reduce the size of functional components when in storage. The most fantastic examples of folding in technology are the solar panels on satellites and appendages in robotics. In micro-fabrication, folding is an auspicious method to produce three-dimensional structures from planar sheets. At such a small scale, capillary forces are sufficient to orient thin membranes or assemble tiny parts[84]. In this study, we turn to the biological world: we investigate mosquito wing folding by capillary forces. We begin by reviewing structural and wetting properties of wings, and the roles these properties play in insect wing folding.

All organisms have elastic properties tuned to either encourage or resist folding. Plants have flower petals which are perennially tightly folded in a bud[85] or those which open and close daily[86]. Insects in the Coleoptera order (ladybugs, sun beetle, cockroach) possess

wings that fold through complex crease patterns, allowing the wings to be stored below the outer shell when not in use[87,88]. While most insect wings are not intended to be folded so tightly, all insect wings experience bending due to aerodynamic forces. Insect wings possess specially tuned stiffnesses to maximize aerodynamic lift during flight[89]. For example, bumblebees exhibited an 8.6% reduction in lift when their wings were stiffened with extra-fine polyester glitter.

The flexibility and resiliency of insect wings is provided by the elastic protein[90], resilin, which enables a wing to store mechanical potential energy when bent[91]. Resilin is also found in mobile wing joints, facilitating energy recovery and leading edge wing twisting[92]. In general, wings are purposefully stiff in certain regions, such as the leading edge[93].

Anisotropic bending is a common property of insect wings. A wing's veins provide resistance against aerodynamic bending moments[94], creating span-chord stiffness anisotropy. Stiffness in the chordwise direction is 1-2 orders of magnitude higher than in the spanwise direction[95], indicating a wing more folds more naturally in the spanwise direction. Finite element models based on *Manduca sexta* forewings show spatial variation in flexural stiffness, firming proximal regions and facilitating bending of edges, where subtle changes in shape are critical to lift production[93]. Due to the highly specialized relationship between an insect's wing shape and its flexural stiffness, it follows that wings are susceptible to failure by changes in curvature, mass, and edge geometry, all of which can arise by the deposition of dew drops.

To resist the accumulation of water drops, insect wings have evolved complex microstructures and surface chemistries. This combination yields hydrophobic, and often superhydrophobic, wetting properties that enable macro-scale drop mobility and wing self-cleaning[43–47]. The hydrophobicity of the wing, however, depends on the size of the drops deposited. Drops much larger than the microstructure exhibit a Cassie-Baxter wetting state such that the drop sits atop a thin layer of air permeating the spaces between the microstructures[48]. These pearl drops are in a favorable wetting state for the insect, as they are easy

to remove. However, if drops are comparable in size to the microstructures, a groove-filling Wenzel-like behavior is observed, pinning drops to the surface and decreasing their mobility[49].

Once insect wings are wetted in the Wenzel state, they can be easily folded by emplaced water drops. Elastocapillarity is the study of the interaction between water surfaces and thin elastic sheets and fibers[96–100]. Much work has been done both on the theoretical level as well as on experiments using synthetic flexible materials. Neukirch *et al.*. (2013) use a variational approach with pinned and mobile contact lines to characterize the resulting shape of an elastic beam underneath a liquid drop. Honschoten *et al.*. (2009) uses picoliter sized droplets to fold micrometric structures separated by discrete hinges to enforce the location of folds. Py *et al.*. (2007) investigate the effects of elasticity and capillarity in folding three-dimensional, millimetric scale structures composed of PDMS. They use modeling to predict the equilibrium shapes of two-dimensional beams under capillary forces. In our study, we show that an approach similar to theirs can predict the folded shapes of mosquito wings.

Most observations of elastocapillarity are done in the laboratory, but such phenomena can also be easily observed in nature. Organisms are susceptible to deposition from mists expelled by waterfalls, dense fogs, and most commonly, nocturnal dewfall. In some areas of the world, dewfall is sufficient to be the sole water source for certain plants[58]. Dew condenses on cooling surfaces as these surfaces radiate heat to the night air and sky. Like plants, poikilothermic insects too will experience condensation due to their low thermal mass. Some insects have adapted to manage condensation, such as the semi-aquatic Fisher spider[64], which is susceptible to dew, but still walks on water. The Namib beetle[57] captures dew so it can drink. The use of dew in generating energy to folding thin surfaces such as insect wings has received little attention.

1.2.6 Water-Rellency & Fur

Water-repellency has previously been viewed as a static property of surfaces such as plant leaves and insect cuticles[101,102]. An equally important trait is dynamic water-repellency, whereby muscular energy is applied to remove water. This paradigm may have use in sensor design. For example, digital cameras already rely upon internal shakers for removing dust from sensors[103]. Such functionality may have improved the capability of the Mars Rover[104,105], which suffered reduced power from accumulation of dust on its solar panels. In the future, self-cleaning and self-drying may arise as an important capability for cameras and other equipment subject to wet or dusty conditions.

Many animals evolved physical adaptations to minimize infiltration of water into their furs or feathers[106,107]. Semi-aquatic mammals possess a dense underfur that maintains large air pockets to insulate the body during a dive[108]. Fur itself often has specialized geometries, such as the grooved interlocking hairs of otters that mechanically resist infiltration of water[109]. Certain animals, such as sheep, additionally secrete oily substances like lanolin that act to increase the hydrophobicity of hair and so discourage fluid-fur contact. In order to arrange their hairs regularly and to uniformly coat them with oil, many animals groom[110] by preening, licking and shaking. Such behaviors may also remove particles in addition to water: birds have been observed to remove dust by shaking after dust-bathing[105] and perform aerial shakes to remove water[18].

Shaking water from an animal surface reduces the combined energetic costs of carrying this water and evaporating it. Small animals may trap substantial volumes of water in their fur for their size[111–113]: emerging from a bath, a human carries 1 pound of water, a rat 5% its mass, and an ant three times its mass. Wet fur is a poor insulator because water's conductivity of 0.6 $\mathrm{Wm^{-1}K^{-1}}$ is 25 times greater than that of air and 12 times greater than that of dry fur[114], causing a wet animal to lose heat very quickly. Evaporation of the entrapped water from an animal's fur may sap a substantial portion of the animal's energy reserves. The specific energy required[115] is $e = 0.6\lambda$ where the heat of vaporization of

water λ = 2257 kJ/kg. Consequently, a wet 60-pound dog, with 1 pound of water in its fur, would use 20% of its daily caloric intake simply to air-dry. It is thus a matter of survival that terrestrial animals remain dry in cold weather[116].

1.3 Thesis Outline

In this thesis we will investigate several dynamical phenomena related to insect flight in particulate environments. We here refer to particulates as droplets of water ranging in size from raindrops to the micro-droplets that deposit on a resting insect. We develop novel experimental and theoretical techniques to discover mechanisms by which insects cope with challenging conditions. Most of this thesis is drawn from recent papers and preprints[117–122]. Chapter 2 provides a collection of experimental techniques used in this thesis, as there is an overlap in techniques between individual chapters.

In Chapter 3 we will begin with an experimental investigation of the impacts of raindrops onto mosquitoes. A mosquito's survival is rationalized through consideration of momentum transfer, and the resulting force, from raindrop to insect. Insect mimics with mass and size similar to mosquitoes are used to determine impact dynamics. We give particular attention to evaluating drop deformation upon impact, noting that drops do not splash upon impact with a mosquito. In Chapter 4 we present experimental results for raindrop impacts onto insect mimics with a range of sizes and densities. Such mimics represent a range of insects beyond mosquitoes, and thus the work compliments that presented in Chapter 3. We notice that by introducing differently massed mimics, two additional impact regimes are possible in which the drop does not remain intact. Predictions for each impact regime are made, for any given mimic mass and radius, by considering the drop's various forms of energy, pre- and post-impact.

In Chapter 5 we examine mosquito flight in hyperdense flight mediums. Using high-speed video and microscopy, we characterize complications the hyperdense mediums of fog particles and refrigerant impose on a mosquito's in-flight sensors, the halteres. Using

a simple Newtonian model, we quantify the additional drag forces by gases of various densities. The time-scale for flight complications is too short for significant fog particle deposition on a mosquito's wings and body. However, in Chapter 6, we investigate the effects of prolonged fog, or dew, deposition onto flying insects. Micro-droplets are able to deposit on the body much more effectively than larger drops. The wings on small to moderately sized insects fold into taco shapes upon wetting under surface tension forces. We employ mosquito wings to determine the dependence of folding magnitude to drop size. Our two-dimensional folding model considers the balance of bending stiffness, Laplace pressure, and surface tension. After fog or dew exposure, a wet insect may employ a number of techniques to remove the extra weight. In Chapter 7, we present measurements of the accelerations mosquitoes use in various drying techniques, by tracking particles in high-speed videos.

Chapter 8 expands the work of insect drying mechanisms by examining the technique furry mammals use to self-dry, rapid, oscillatory shaking. By studying a range of species, we draw a relationship between body mass and shaking frequency. Analysis of drop ejection from a single tuft of hair resolves the physical underpinnings of each animal's chosen frequency, and the shake's effectiveness. In Chapter 9, we conclude by discussing the implications of our work and suggesting directions for future research.

CHAPTER II

EXPERIMENTAL TECHNIQUES

2.1 Mosquito Source & Care

Non-blood fed, 2-5 day old adult *Anopheles gambi* and *Anopheles freeborni* mosquitoes were obtained from the Malaria Research and Reference Reagent Resource Center at the Center for Disease Control (CDC). They were housed with cotton balls of sugar water in our lab. Insects were filmed one at a time to avoid pseudo-replication.

2.2 Mosquito Handling

Mosquitoes are transferred to various containers with a John Hock brand aspirator. They are singularly held in place by one of two methods. The first method is by a continuous vacuum pen (Virtual Industries Tweezer Vac) which can pick up and release mosquitoes without removing appendages or rupturing their exoskeleton. The second method, used in tethered experiments, employs liquified wax to attach them to a tether, which is preferable for long-term restraint, as it places no external forces on the exoskeleton. Tethering with wax just behind the head or performing other tedious procedures, such as glue deposition on the halteres, requires the mosquitoes to be incapacitated by inhalation of CO_2. Short exposure to the gas anesthetizes insects, while prolonged exposure causes death. Tethering requires the mosquitoes be exposed to CO_2 for 10 seconds, to remain asleep for roughly 20 seconds.

Wings are removed from freshly dead or anesthetized mosquitoes with scissors by removing a small bit of the thorax connected to the wing. A 50 SWG wire is attached in the base of the wing with Loctite brand superglue. The wing tips are clipped at the tip to create

a flat edge, so that wing edges will appear in sharp focus through our microscope.

2.3 Filming

A Phantom V210 and Phantom Miro 110M high-speed cameras are the primary tool for observing of mosquito flight, and we film over a range of 24 - 10,000 fps. A Nikon AF Nikkor 50 mm 1:18D lens is used to capture the entire flight arena, while a Navitar 1-60135 is used for macro filming. Flight arenas are lit by 4 low temperature LEDs (IDT Honeycomb LED-1). For wing folding videos, the high-speed cameras are attached to an Olympus SZX16 dissection microscope, using up to an 8x zoom. Ablated wings are lit with a single 900420 1×3 LED array by Visual Instrumentation Corporation from above, and a Dedolight DT4.1 from below. The lights provide enough heat to evaporate deposited moisture within 10 minutes, but do not warp dry wings.

Measurement and tracking within videos is done with Tracker, an open source physics program. All reported P-values in this manuscript are results of an unpaired t-test application to our data.

2.4 Insect Mimic Experiments

To capture the effects of drop impact on inanimate objects in flight, we collided them with drops freely and without support. A schematic of the apparatus is shown in **Fig.4**. A syringe was used to generate a single drop from a nozzle suspended as high as 1.5 m above the subject. The falling drop passed through an infrared beam (modified photo-gate) which triggered a high-speed pull-type solenoid leaving the object momentarily airborne, and poised to be struck by a drop. Attached to the solenoid is a supporting arm composed of two thin wires, sufficiently stiff to support insect mimics, but thin enough not to drag the objects down its wake when retracted. The impact is filmed with a Phantom high-speed camera and lit by Schott fiberoptic lights.

We build 18 spherical and 10 cylindrical mimics, whose masses of 1 to 1000 mg and radii of 1 to 10 mm. The mimics span the range of most flying insects (**Fig.5**, Video

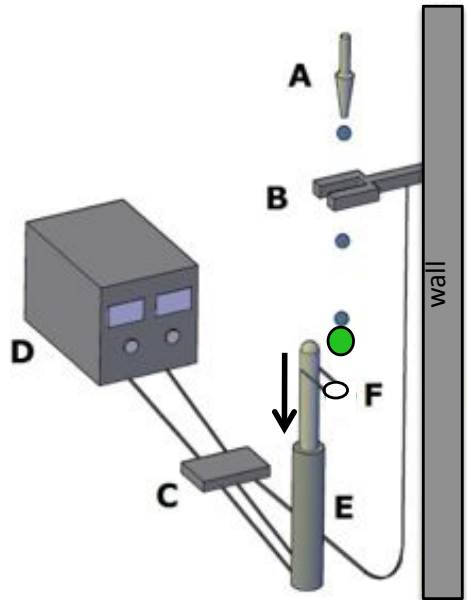

Figure 4: Schematic of apparatus used to strike insect mimics with drops, where (A) Nozzle, (B) Infrared laser sensor, (C) Controller, (D) Power supply, (E) Pull-type solenoid, (F) Material holder.

S2). In designing mimics, we neglect insect wetting properties, legs, and wings. Spherical mimics consist of an assortment of materials, including steel ball bearings, wooden beads, clay balls formed by hand, and styrofoam pellets. Additional mimics of cylindrical shape increase the mass range achievable by spherical mimics. Cylinder mass is easily varied by the insertion of steel or wooden cores and wrapping the outer layer of styrofoam with scotch tape. To ensure at least some similarity to filming of the spherical mimics, cylinders are filmed so that their circular cross-section faces the camera.

Mimic impacts are filmed at 1950 fps with a Phantom Miro 4C. We estimate acceleration of the mimic using the change in velocity over one video frame (513 μs). Acceleration measurements of mimics are performed at two incoming drop speeds, 2.2 m/s and 5 m/s. We combine both data sets in this study. We do not expect this variation in drop speed varying to substantially affect impact acceleration, which varies by several orders of magnitude over the masses considered.

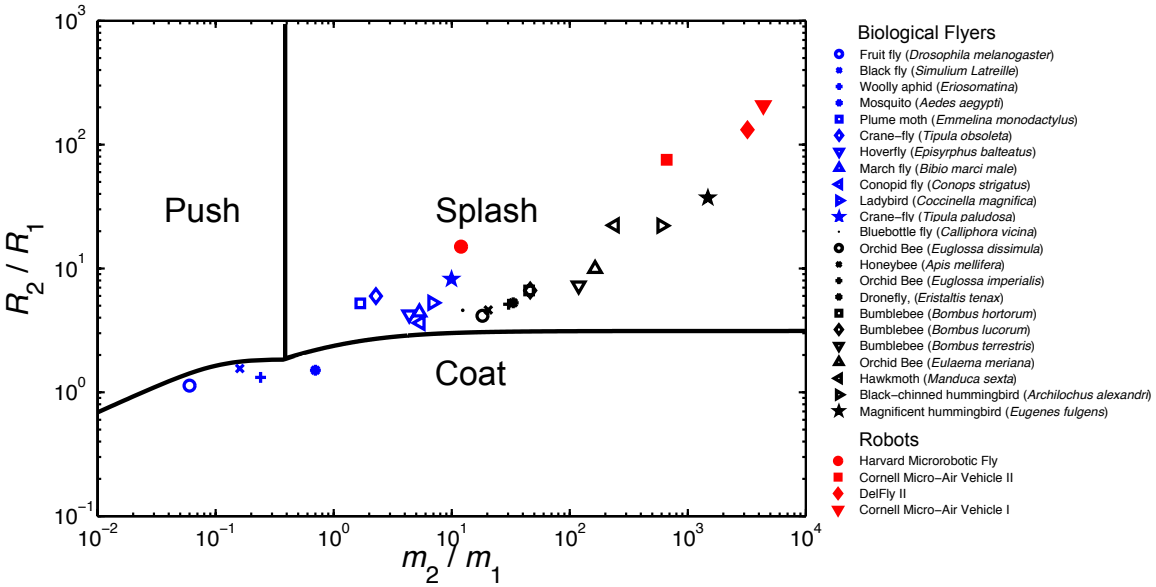

Figure 5: The relation between ratios of insects[123–133] and flying robots[2–4,6] with half-wingspan R_2 with mass m_2, and raindrop with radius R_1 and mass m_1. Boundaries between impact modes are drawn from theory presented in §4.2. Insects and robots are listed in order of increasing mass.

2.5 Rain simulators.

For studying the behavior of living insects, we enclosed a group of insects in a closed acrylic container with 5 cm length and width, 20 cm height for experiments when a high-speed jet is employed. A nozzle is positioned at the roof of the container and jet is produced by a Cole Parmer 75211-10 Gear Pump. The impacts are captured with a Phantom V210 high-speed camera at 4000 fps.

For dripping experiments, the container is reduced to 10 cm to heighten the probability of impact. A nozzle is placed at variable height above the cage, supplied with dripping water of variable speed by the aforementioned pump. The nozzle's flow will transition from jetting to dripping by reducing the flow rate. Wet plastic mesh is placed at the top of the container, so that drops hitting the mesh release water collected upon it, allowing high speed drops to enter the cage without letting mosquitoes escape. Impacts occur opportunistically, and the recovery of the insects is captured with a Phantom Miro 4C high-speed

camera at 6400 fps.

2.6 Fog Experiments

Fog is produced with an Air O Swiss 7145 consumer humidifier with continuous adjustability in fog density. A hose attached to the humidifier directs the stream of mist to the subject. A droplet sizing instrument (DC-III; KLD Labs Inc., New York, NY) is used to characterize the spectra of droplets generated by our humidifiers. As seen in **Fig.6**, a miniature wind tunnel (7.5 cm x 5 cm x 11 cm) has been constructed to deliver fog to a mosquito's contained, flight environment. It uses a variable speed computer fan to pull air through a 6.5 cm x 1 cm opening, which uses a square grate to laminarize the incoming air and contain mosquitoes. The air speed at the inlet is 3 cm/s, measured by particle tracking. Control experiments indicate no substantial effect of incoming air on mosquito flight. Flight is evoked from the mosquitoes within by human breath into the tunnel's intake. Human breath excites both male and female *Anopheles freeborni*. We observe no difference in flight failure characteristics between male and female mosquitoes, and no attempt was made to separate the sexes following initial experiments.

2.7 Dense Gas Experiments

For experiments with flight in various gas densities, R134a (1,1,1,2-Tetrafluoroethane), a non-toxic gas[134], with a density of 4.25 kg/m^3 at standard temperature and pressure, is piped into a sealed, transparent, semi-circular container of height 15 cm and width 5.5 cm. Mosquitoes were capable of indefinite perching on the interior walls and ends of the container post-experiment. Subjects used in R134a-based experiments are still alive the day following exposure to R134a, when sufficient ambient oxygen is allowed into their container. The density of the gas mixture inside the container is determined by the container's mass reading on an analytical balance. Atmospheric conditions inside our lab remain with

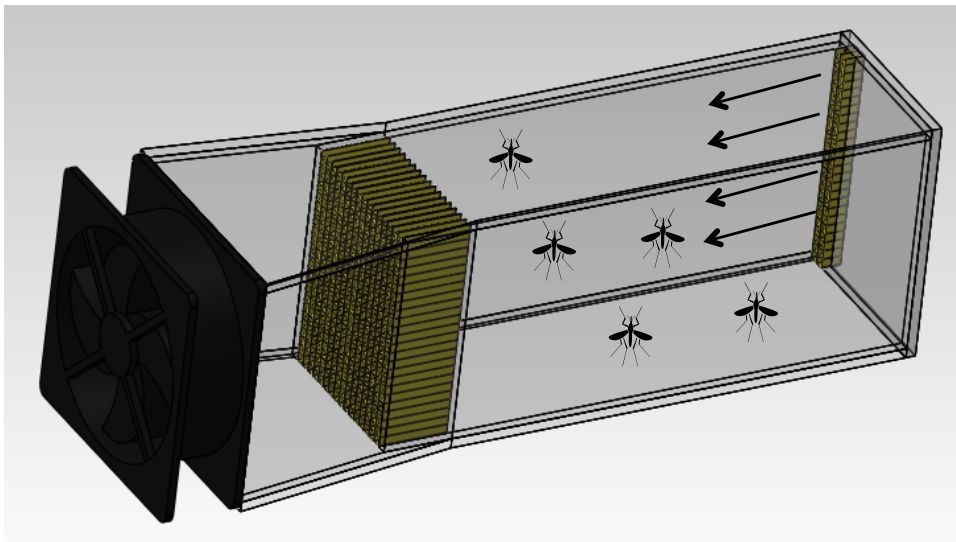

Figure 6: Miniature wind tunnel used to visualized mosquito flight upon entering a dense fog stream and takeoff. A variable speed computer fan pulls in fog at 3 cm/s as denoted by the arrows.

5 °C range. Mosquitoes were introduced through a hole in the top of the container, and allowed to fly freely, or fall to the bottom.

2.8 Haltere Augmentation Experiments

To investigate the effect of altered forcing on mosquito halteres, we laden the halteres of untethered, anesthetized mosquitoes with UV curable glue with density ρ_{glue}=960 kg/m^3, a the haltere tip. The glue's density is measured by massing a disc of cured glue whose volume is measured by digital calipers. The glue is deposited onto unconscious mosquitoes via a thin wire, by hand, under a microscope. Glue is cured with a UV flashlight. Mosquitoes are given 10 minutes to recover from anesthesia and released for observation. Mosquitoes anesthetized by the same manor as those with glue on halteres recovered to resume qualitatively normal flight after approximately 5 minutes in atmospheric air. Post-flight, mosquitoes are imaged in a Phenom Pro G2 scanning electron microscope (SEM), which provides a reference scale in frame, to measure the volume of glue deposited. Glue dollops are traced with Tracker to calculate the irregular shape's area and thickness.

2.9 Wing Measurements

Measurements of wing dimensions and wing cross-sectional shape within videos is done digitally with Tracker, an open source physics program. Drop areas are found by tracing the drops in Tracker, creating an irregularly-shaped polygon of more than 100 sides. The polygon's coordinates are exported to MATLAB for area calculation.

Experiments pertaining to wet mammals in Chapter 8

2.10 Animal measurements

We and the Zoo Atlanta staff measured by hand the masses and torso radius of 28 of the 33 animals in our study. The masses and radii of the remaining 5 animals (squirrel, black bear, brown bear, lion, and tiger) were inferred using a combination of methods. Tiger and lion masses were provided by the Zoo staff from recent veterinary procedures in which the animal was anesthetized and weighed. Chest girth measurements for the tiger and lion were not safely measurable by the Zoo staff, and were thus inferred from literature, based on the animals' masses[135,136]. Videos of three species (squirrel, black bear, and brown bear) were obtained from YouTube and BBC, where their masses and radii were estimated based on previous measurements of adults in the literature[137–142].

2.11 Wet-dog simulator.

We built a "wet-dog simulator" apparatus to visualize the motion of drops on a shaking mammal. The apparatus is described further in the Supplementary Info Section. "Dog" fur was provided by three squares of 6.3 cm^2.5 squares of white-tailed deer tanned fur, which were glued with non-water-soluble glue to plastic bases clipped to the rotating axis of our device. Prior to experiments, loose hairs were removed and samples immersed in water for 4 hours to ensure complete saturation into skin and fur. Samples were unidirectionally spun for 30 seconds on the wet-dog simulator at a radius of 2 cm at various frequencies. Between

trials, samples were weighed, resaturated with water, and drip dried for 30 seconds.

2.12 Brush experiments

In order to test Tate's law, we used 19 brushes with round bases (Loew Cornell Nylon 1812 brushes, Loew Cornell Bristle 1812 brushes, and Sterling Studio synthetic brushes SS-100 round set). Originally tapered at a range of slopes, we shaved the brushes to produce a flat tip. We weighed drops dripping from the brushes on an analytical balance. To obtain data in **Fig.45**d, three brushes were placed on the "wet-dog simulator" and the mass of ejected drops at various rotational speeds was determined through image processing with Matlab. The cylindrical shell method was used to determine the volume of elliptical drops.

2.13 Experiments using the "Wet-Dog Simulator"

The spinning apparatus consisted of two parts, a frame and a spinning plate, both of which were constructed from pressure-treated wood. The spinning plate, oriented vertically, holds the camera and subjects, which spin in the same frame. At the top the high-speed camera, Vision Research Miro-4c, is fixed, aimed down. A 5" slot along the center of the plate allows subjects to be placed at variable distances from the lens. This ensured the camera was capable of focusing on the material being studied. The holder for different subject matter was attached to 3/8" bolt, which used a nut to hold it in place once it was positioned. Multiple holes drilled along the slot served as mountings holes for the light, which light the scene from above. It was necessary to position a light above the material, because the high frame rate of the high-speed camera required a large amount of light for the material to be visible. The light was a modified Coleman Max Bubba LED flashlight, which was powered by 6 AA batteries attached to the back of the spinning plate. A Rigid model R7000 corded power drill attached to the spindle at the top provided the torque necessary to spin the plate. The motor was powered from a variable AC power supply. The power supply, Variac Transformer model TDGC-0-5KM, provided an output of 1-130 VAC at 60 Hz. Adjusting the voltage output of the power supply controlled the speed of the drill. A

Laser Tachometer, ES Pro model # 332, was used to determine the rotational velocity of the plate.

2.14 Filming of Rat Shaking with X-Ray Videography

High-speed x-ray videos of shaking rats were captured on a custom built video system. X-rays were emitted from a 97 kV, 2 mA monoblock-160 continuous beam x-ray emitting tube from VJ Technologies. The x-rays passed into a 255 mm diameter input window image intensifier (TH-9438-HX, VJ Technologies), which converted them into visible light. A high-speed video camera (A504k, Basler Vision Technologies) was used to record the converted light. The video was recorded at 200 frames per second and saved to a dedicated computer using digital recording software (Streampix, Norpix Inc.)[143]. The rat was contained in a waterproof box constructed out of acrylic glass sheets. The box was large enough for the rat to retain mobility and rear-up while shaking, but narrow enough to orient the rat in the direction necessary for the experiment. A water reservoir was assembled from 4 diameter PVC pipe. A Rainbird 0.75” inline valve was attached at the base of the reservoir. This valve allowed water to flow when voltage was supplied to a solenoid. The voltage was supplied from three nine-volt batteries, and a simple SPST switched was used to open and close the circuit. This set-up allowed for the flow of water to be controlled at a safe distance, which minimized exposure to radiation. A plastic tube running the length of the box was used to sprinkle water from the reservoir onto the rat. After setup, all the researchers moved a safe distance from the x-ray camera the valve was activated. When the water reached the rat, the camera captured video. The procedure was repeated several times until an adequate video was achieved for a front and side view.

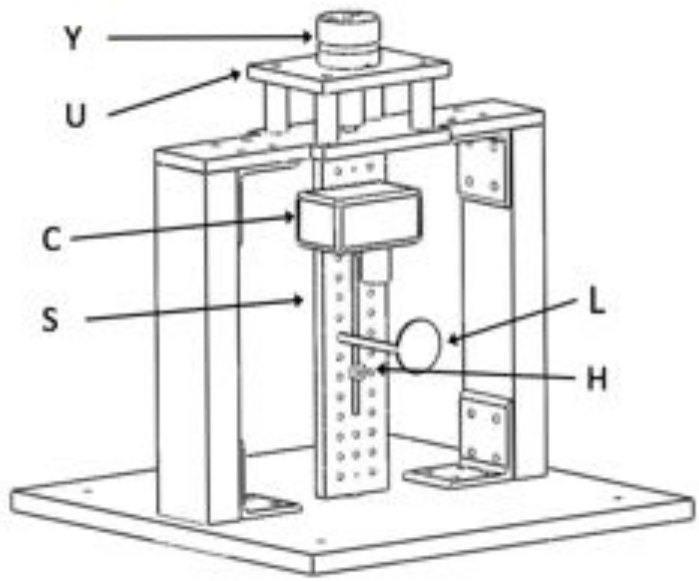

Figure 7: Wet-dog simulator with labeled components: motor (Y), motor mount (U), high-speed camera (C), spinning plate (S), light emitting diode (L), and material holder (H).

CHAPTER III

MOSQUITOES SURVIVE RAINDROP COLLISIONS BY VIRTUE OF THEIR LOW MASS

"If a mosquito has a soul, it is mostly evil. So I don't have too many qualms about putting a mosquito out of its misery." -Douglas Hofstadter

In this combined theoretical and experimental study, we investigate drop impact onto free bodies, free-flying mosquitoes and similarly massed mimics. In §3.1, we begin by presenting preliminary theoretical considerations for impacts on free bodies. In §3.2, we proceed with a description of a mosquito flying into a stream of terminal velocity raindrops, then compare mosquito-drop impacts to those between mimics and raindrops. We measure impact accelerations for various mimics, paying particular attention to drop deformation on impact. We discuss our theoretical simplifications and implications of our research in §3.3, and summarize our conclusions in §3.4.

3.1 Preliminary theoretical considerations

To investigate how flapping flight is affected by rain, we care for and film *Anopheles gambi* mosquitoes, a species that is found in moist climates and is likely to face rainy conditions regularly. These mosquitoes have a body length of 3 mm and a mass of m_2 = 2 mg. As shown in **Fig.8**a, raindrops are of comparable size[144], with a radius $R_1 = 0.1 - 0.4$ cm. However, the raindrops are of much larger mass $m_1 = 4 - 100$ mg: the mass-ratio of the raindrops to mosquitoes is $m_1/m_2 = 2 - 50$. Two objects with the same mass ratio are a person laying underneath the wheel of a bus, a scenario whose outcome suggests that mosquitoes should not survive raindrop collision.

To gain insight into the collision forces, we consider a simplified scenario. Consider raindrop impact force onto a mosquito resting on an unyielding surface such as a tree branch. The dynamics of drop impact onto unyielding surfaces[29] (e.g., of infinite mass) has been well-studied. Upon striking such a surface, raindrops exhibit a spreading stage and a receding stage. Given the terminal velocity of rain, $u_1 = 6-9$ m/s[145], the duration of the spreading is an exceedingly short $\tau = R_1/u_1 \approx 1$ ms, Therefore, the impact force associated with the transfer of momentum on an unyielding surface is $F \sim m_1 u_1/\tau \approx 5\times 10^4$ dynes, which is 10^4 times the weight of a mosquito. This large force further suggests raindrop impacts should be deadly to mosquitoes.

The likelihood of a raindrop impact can be predicted by considering the mosquito as a target for a raindrop. A vertically falling raindrop encounters a plan-view of the insect given by its wings, legs, and remainder of the insect's body, whose total surface area $A_m =$ 30-40 mm^2. During the heaviest rain[146] with drops of mass $m_1 = 16$ mg, falling with an intensity $I \approx 50$ mm/hr, a stationary mosquito will receive an impact on average every $\Delta t = m_1/(I\rho A_m) = 25$ seconds, where ρ is the density of water. Thus it is quite likely that a free-flying mosquito will be struck by a drop during a rainstorm.

The mosquito's long legs and wings account for three-fourths of the potential impact area, with the body accounting for only one-fourth. If a drop falls with uniform probability on these surfaces, impacts on the wings and legs are three times more probable than on the body. We will test this prediction in our experiments.

3.2 Experimental Results

3.2.1 Jet impacts cause mosquitoes to tumble

We constructed a flight arena composed of a small acrylic cage of width 5 cm, covered with a mesh top to both contain the mosquitoes but permit the entry of drops (**Fig.8**b). To prevent the insects from landing on the walls, the cage was vibrated manually every few seconds. In this confined environment, we observed insects made no attempt to escape

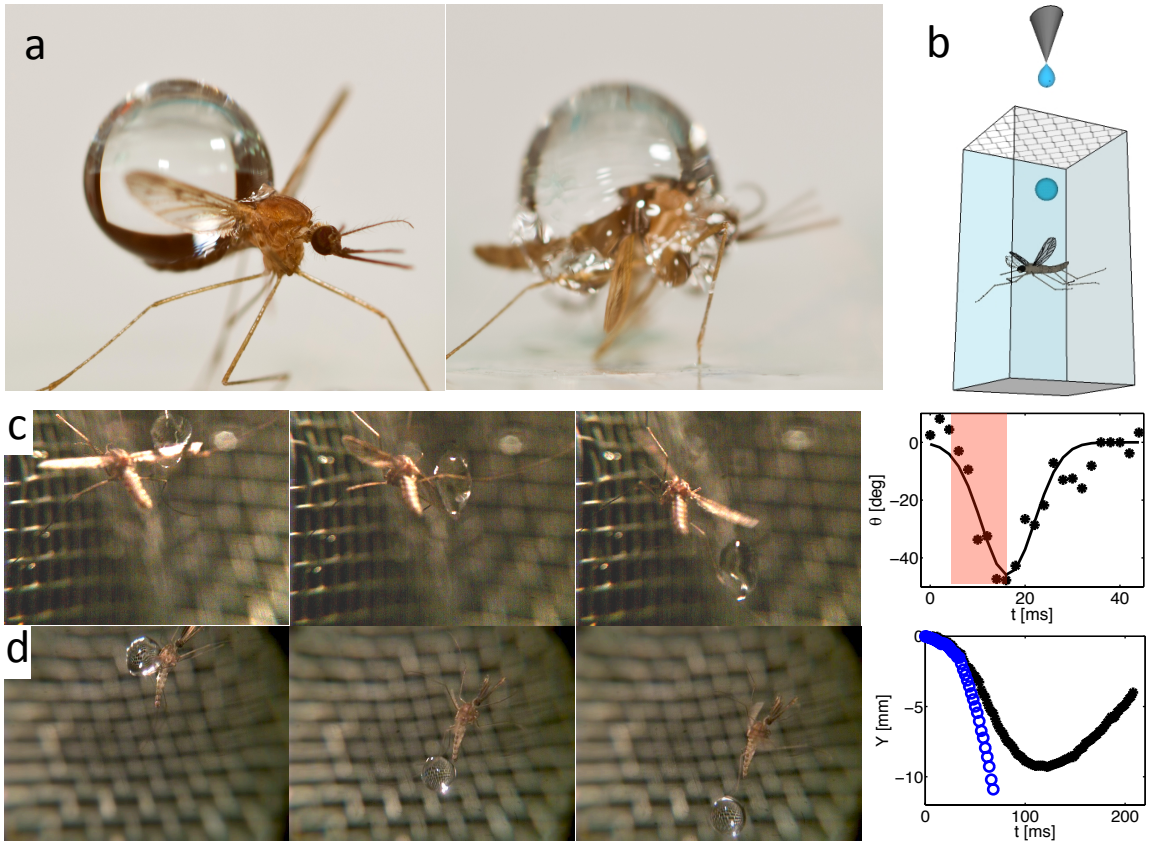

Figure 8: **(a)** Impact of a 3 mm drop on a mosquito supported from below, meant to show the relative size of raindrop to a mosquito. **(b)** Schematic of our drop impact chamber. **(c)** Time sequence of a mosquito spun by a falling drop. Graph shows the time course of angular position of a mosquito where the pink shaded area denotes the duration of contact with the drop. **(d)** Time sequence of a mosquito pushed by a drop. Graph shows the time courses of vertical positions of the mosquito (black) and drop (blue). In both impacts (c-d), the mosquito easily recovers and continues flying.

being struck by drops (Video S1). In our first series of experiments, we desired to strike a mosquito with a terminal velocity raindrop. This requires releasing drops at a height of about 10 m, which was nearly impossible to aim into our flight arena. Instead, we employed a jet of water to simulate rainfall. We used a gear pump to shoot a 9 m/s jet of water into a container of flying mosquitoes (**Fig.9**). Jet speed and mosquito position were confirmed using high-speed filming at 4000 fps (see Methods). Due to fortuitous cavitation in the pump, the jet was pulsatile, a combination of drops and jetting streams.

Using this setup, we observed 6 mosquitoes struck with high-speed jets. A mosquito is

rapidly accelerated downwards upon collision with the jet. Continued perturbations with the jet tumble the mosquito repeatedly. **Fig.9** shows one example: impact by a 9 m/s jet accelerates the mosquito to a velocity of 2.1 m/s within a duration of 1.5 ms. After tumbling a distance of 39 mm, or 13 body lengths, the mosquito finally separates laterally from the jet and lands on the side of the container. The 6 mosquitoes tested each separated from the jet before striking the bottom of the 20-cm tall chamber. It was noteworthy that all the mosquitoes survived the collision, as shown by their flight after a brief resting period. We estimate the drops in our jetting streams have a diameter of $4-6$ mm, and mass $33-113$ mg, corresponding to kinetic energies ranging from $1.36-4.58$ mJ. The fastest recorded drop falling through quiescent fluid in literature[145] was 102 mg, traveling at 9.17 m/s, with kinetic energy 4.30 mJ. By comparison, a 1 mm diameter raindrop will fall at 4.03 m/s, with a kinetic energy of 0.021 mJ. These experiments confirm that mosquitoes can survive impact with terminal-velocity raindrops.

3.2.2 Drop impacts on mosquitoes

To obtain films at higher resolution as well as more accurate body tracking, we filmed free-flying mosquitoes subjected to drops falling at a lower speed than the jets. A small nozzle of variable height ejected individual drops of radius 0.15 - 0.25 cm at speeds of 10 - 260 cm/s (**Fig.8**c-d).

We observed impacts on the wings and legs are far more likely (N=13) than on the body (N=4), as predicted. These glancing blows cause a pitch, yaw or roll rotation to the insect, depending on the point of impact. An impact on the wing is shown in **Fig.8**c and Video S1. The mosquito rolls an amplitude of $\theta \approx 50^\circ \approx 0.9$ rad with a contact duration $\tau = 10^{-2}$ s with the drop. The insect subsequently recovered its original position in 10^{-2} s. We can estimate the forces involved using the geometry of the insect and neglecting aerodynamic losses in this short duration. The torque applied by the drop is $r \times F = I\alpha$, where the mass moment of inertia of the insect $I = m_2 R_e^2/2 \approx 4 \times 10^{-5}$ g·cm^2, R_e is the

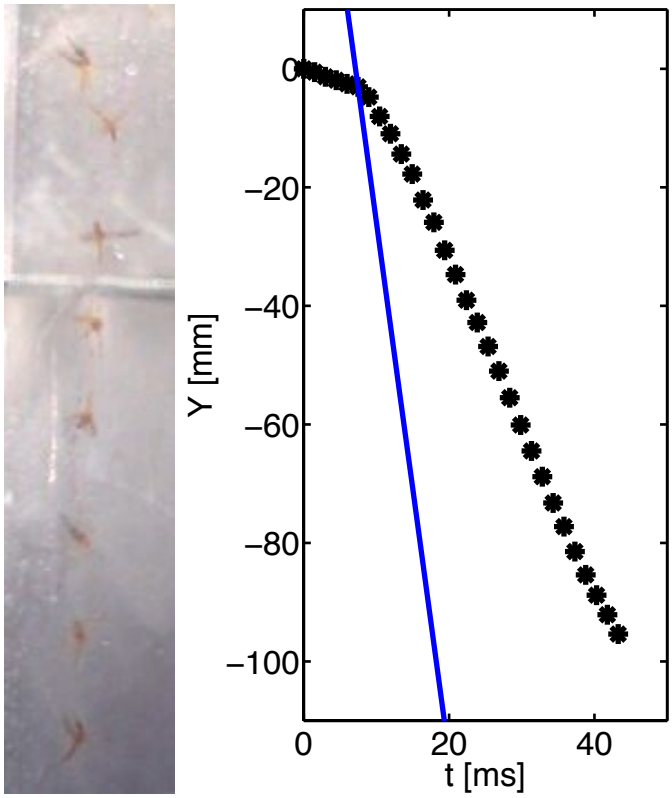

Figure 9: Mosquito being pushed and tumbled by a vertical jet traveling at 9 m/s. The graph indicates the time course of the vertical position of the jet and mosquito, shown in blue and black respectively.

effective radius of its mass, and the force is applied to the wing at a distance $r \sim 1$mm from the center of mass. Using the observed angular acceleration of $\alpha = \theta/\tau^2 \sim 10^4$ rad/s^2, we find the impact force is $F \approx 3.5$ dynes, or nearly two mosquito masses, and from which the mosquito easily recovered.

If the drop makes a direct hit with the insect's center of mass, such as between the wings, a very different outcome from a glancing blow occurs. The insect is pushed downward a distance of several body lengths at the same speed of the drop. This is shown in **Fig.8**d and the Video S1. Upon impact the drop remains intact and nearly at the same speed. These features suggest little force is imparted, in contrast to the splash observed due to impact upon an immobile surface. A mosquito is always able to laterally separate itself from the drop and recover its flight (N =17). The mosquito's falling distance while pinned

by the drop varies from 5 - 20 body lengths. Thus it is imperative a mosquito does not fly too low during rain or it will suffer an secondary impact with the ground.

3.2.3 Drop impacts on mosquito mimics

Clearly, mosquitoes are able to survive impacts from both low and high speed drops. In the collision of two bodies, the outcome is known to be highly dependent on the masses involved[147]. We thus hypothesize that mosquitoes survive drop impacts by virtue of their low mass: specifically, the low mass of mosquitoes causes a falling drop to maintain most of its speed after impact and apply a correspondingly low impact force to the mosquitoes.

To test this hypothesis, we conducted tests with mimics of the same mass as mosquitoes. We constructed insect mimics using styrofoam spheres of varying mass (0.4-1.8 mg) and radius (1.65-2.75 mm), as shown in **Fig.10**a. Our use of mimics enabled us to investigate the dynamics of drop impact at drop speeds up to 2.60 m/s, which are closer to the terminal velocities of raindrops. The mimics were held in place using a solenoid that was trigged to drop instantaneously by the approaching drop, leaving the sphere momentarily suspended and poised for impact (**Fig.10**c). We tracked the position of the drop and spheres, both before and immediately after impact (**Fig.10**d,e) to determine their change in velocity. Initial drop speeds highlighted in **Fig.10**d,e are 2.3 and 0.31 m/s respectively. We generated drops with mass ratios of m_1/m_2 = 1 - 300 with respect to our mimics. We expect the behavior of the impact within the range m_1/m_2 = 1 - 50 to be dynamically similar to our mosquito experiments.

Consider the collision of a drop of mass m_1 and speed u_1 with a stationary insect of mass m_2 hovering in mid-air. From our experiments of direct hits with mosquitoes, we observed the collision is inelastic, namely, that the insect and drop adhere immediately after impact into a combined lump of mass $(m_1 + m_2)$ of speed u' (**Fig.10**b). Conservation of linear momentum indicates the final velocity u' of the combined mass system is

$$\frac{u'}{u_1} = \left(1 + \frac{m_2}{m_1}\right)^{-1}. \tag{3.1}$$

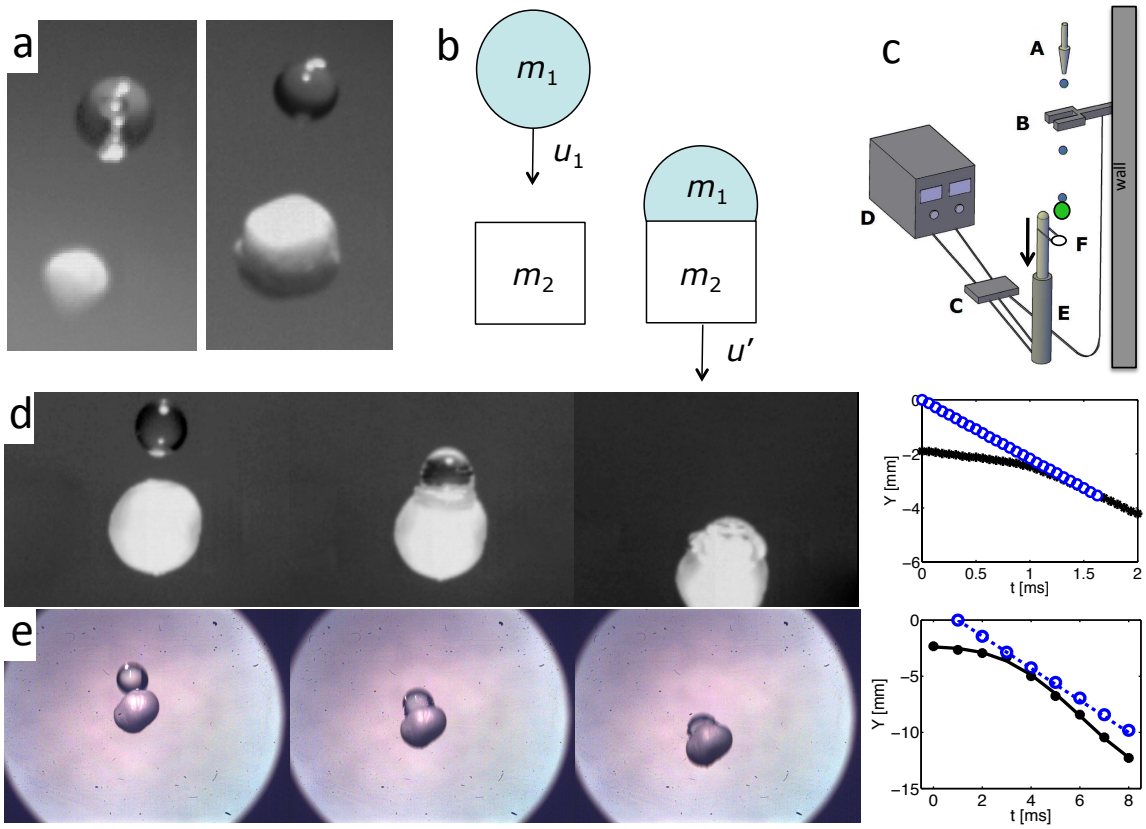

Figure 10: **(a)** Insect mimics composed of variably sized styrofoam spheres. Both small and large size are shown with respect to a drop. **(b)** Schematic of inelastic impact between drop and insect. **(c)** Schematic of apparatus used to strike insect mimics with drops, where (A) Nozzle, (B) Infrared laser sensor, (C) Controller, (D) Power supply, (E) Pull-type solenoid, (F) Material holder. **(d-e)** Video sequences of drop impact onto small (d) and large (e) insect mimics with respect to the drop. Graphs indicate the time course of the vertical positions of the drops and mimics, shown in blue and black respectively. Note, in both cases, the velocity of the drop is only slightly influenced.

Measurements of the dimensionless drop speed after impact u'/u_1 are given in **Fig.11**a for a range of dimensionless drop masses m_1/m_2. The drop is only slowed slightly (2-17%). Notice that direct impacts, which cause no rotation, follow the prediction in Eq. (3.1) well. Departure from the prediction occurs when a drop glances the mimic, rotates around it, and pulls it downward. More kinetic energy is lost in this rotation, as compared to the direct impacts.

The blue X in **Fig.11**a corresponds to a direct impact with a mosquito and fits the prediction, Eq. (3.1), well. Here, the final velocity $u' = 0.9u_1$, indicating the drop's speed

decreases only 10%: the drop continues in its path unimpeded by the mosquito. It is noteworthy this result is strongly dependent on the mosquito's low mass. For instance, according to Eq. (4.1), a much heavier dragonfly with a mass of 1 g will cause the drop to decrease in speed by 91%, stopping the drop in its tracks.

From our tests with mimics, we observed raindrops do not splash upon mosquitoes, but simply deform. We rationalize this surprising result by comparing drop deformation χ in our experiments to the results observed by Clanet et al. 2004[148]. For water, Clanet et al. 2004 found a relation for the drop deformation, $\chi/R_1 \sim \mathrm{We}^{1/4}$, when a drop impacts a solid surface, where We$=\rho u_1^2 R_1/\sigma$. In particular, they observed a drop with R_1 = 1.65 mm impacting rigid plastic at u_1 = 0.81 m/s experienced a maximal deformation of χ/R_1 = 1.1 and did not splash. The highest χ/R_1 value we witnessed in our mosquito mimic experiments was a lower value of 0.77 (**Fig.11**b) and so we conclude splashing on mosquitoes is not possible.

Furthermore, we can predict the deformation radius of drops at various impact speeds using methods inspired by those of Okumura et al. 2003[149]. Using a coordinate frame fixed on the drop, the relation between the change in speed of a drop $u_1 - u'$ and its internal pressure p is given by Euler's equation,

$$\rho \frac{\mathrm{D}}{\mathrm{D}t}(u_1 - u') = -\nabla p + \rho g. \tag{3.2}$$

Assuming the drop's radius undergoes a small deformation during impact, we may scale the duration of impact

$$\tau \sim \chi/(u_1 - u') \tag{3.3}$$

and the pressure gradient

$$\nabla p \sim \sigma \chi^2/R_1^3 \tag{3.4}$$

where σ is the surface tension of water. Euler's equation at low Bond numbers (Bo$=\Delta\rho g l^2/\sigma=$ 0.003 - 0.009 as found in our experiments), yields

$$\rho (u_1 - u')^2 R_1^3 \sim \sigma \chi^2. \tag{3.5}$$

The dimensionless deformation may be written as

$$\frac{\chi}{R_1} \sim \mathrm{We}^{\frac{1}{2}} \left(\frac{m_1}{m_2} + 1 \right)^{\gamma} \tag{3.6}$$

where We = $\rho u_1^2 R_1/\sigma$ and the predicted exponent γ from literature is -1. Our measurements of the dimensionless drop deformation χ/R_1 are shown in **Fig.11**b. Our power-law fit for our drop deformations is excellent (with an R^2 value of 0.93), and moreover has an exponent of -0.85, very close to the prediction of -1. Thus we find drop deformation is inversely proportional to drop size: a small drop suffers a larger change in speed and larger deformation than a large drop, keeping all other conditions the same.

3.2.4 Impact force by a raindrop

If drops do not splash on mosquitoes, we can easily estimate the force of direct impacts on the mosquito. During inelastic impact, a mosquito experiences a change in momentum $m_2 u'$ over an impact duration τ, yielding an impact force

$$F = \frac{u' m_2}{\tau} = \frac{u_1 \varphi}{\tau} \tag{3.7}$$

where the reduced mass of the system is $\varphi = m_1 m_2/(m_1 + m_2)$ and the measured range of impact durations was $\tau \approx$ 0.5-1.8 ms. In the limit of $m_1 \ll m_2$, the force scales as $m_1 u_1/\tau$, where m_1 is small. This scaling indicates that the applied force decreases in proportion with insect size, consistent with our hypothesis.

Fig.11c shows the associated acceleration scaled by gravity, experimentally measured on our insect mimics. At first glance it appears that this force is quite high, as shown by the range of accelerations of 100-300 gravities (g), equivalent to 50-150 mosquito weights. However, this range is two orders of magnitude less than impact on a unyielding surface (10,000 dynes); moreover, it amounts to very low absolute values that the insect can clearly survive. For example, a 2 dyne mosquito experiencing 300 g will feel a force of 600 dynes or 0.61 grams-force, the weight of a small feather. Moreover, these estimates remain robust when we increase the speed of the drop to terminal raindrop speeds. The 6 mosquitoes

struck by jets, as demonstrated in **Fig.9**, experienced 80 ± 35 g, a fraction of the force due to a direct impact. Glancing blows, which cause tumbling, vastly reduce impact force.

Although the impact force of $F \approx$ 200-600 dynes is many times the insect's body weight, it is easily survivable because the insect's exoskeleton enables small insects to support large loads[150]. To confirm this, we performed compression tests using an analytical balance and a micromanipulator to determine mosquito's threshold to force. When subjected to a sustained compressive force, a mosquito survived up to about 3,000 - 4,000 dynes (N=3) and was still able to fly. When subjected to a larger force of 8,000 - 10,000 dynes, the mosquito did not survive. Since these values exceed by an order of magnitude the impact forces applied by raindrops, we conclude a flying mosquito cannot be killed by the impact of falling rain.

3.3 Discussion

We performed raindrop-impact experiments on both mosquitoes and their mimics, finding that the momentum and force imparted to the insect is determined entirely by the insect's mass relative to the drop. The mosquito is so lightweight that the resulting force imparted to it is low, enabling a mosquito to survive flying in the rain. This result is in stark contrast to the resulting force on immobile surfaces for which splashing and large momentum transfers occur.

Although the raindrop force imparted to a mosquito is low, the mosquito's low mass causes the concomitant acceleration to be quite high. Insects struck by rain may achieve the highest survivable accelerations (100-300 g) in the animal kingdom. In comparison, the current champions of generating acceleration are fleas, which experience 135 g when jumping[151]. The similarity between these maximal accelerations may suggest a fundamental limit to survival among organisms.

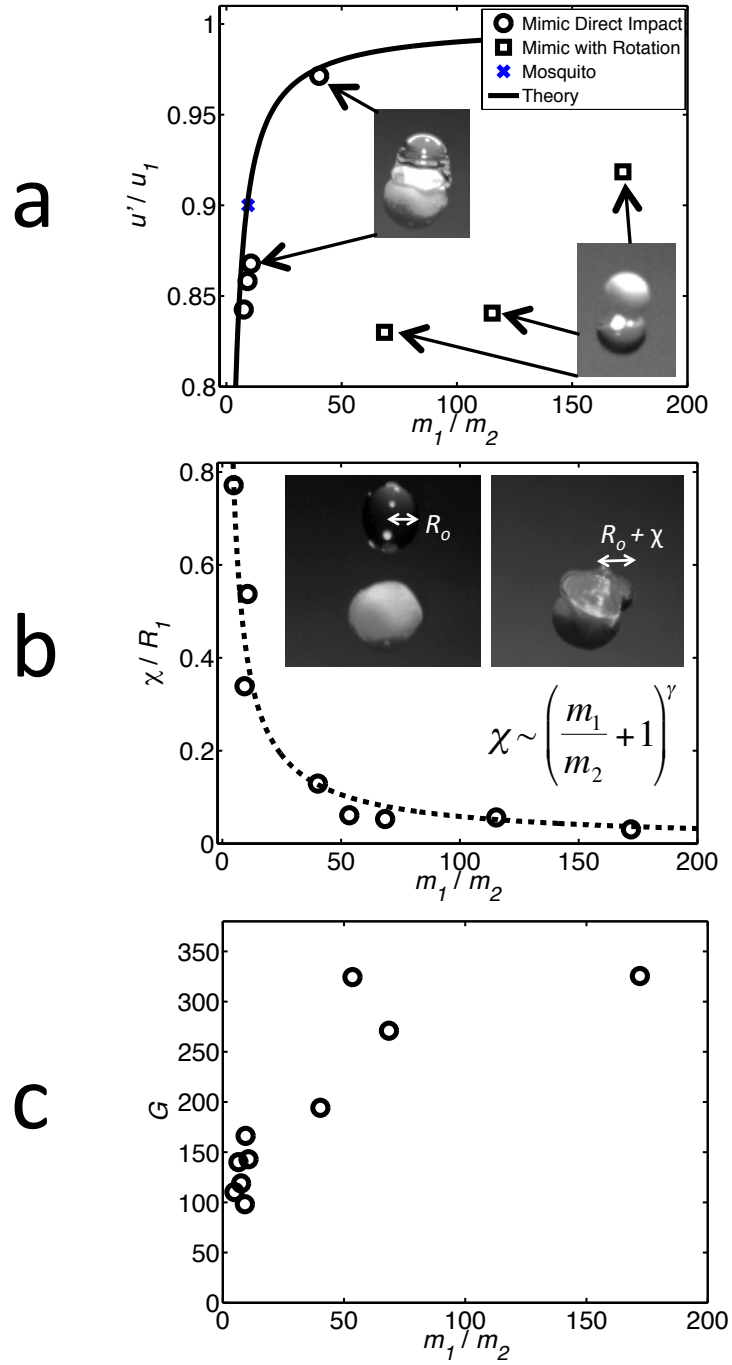

Figure 11: Relations between dimensionless drop mass and **(a)** dimensionless final drop velocity, **(b)** dimensionless drop deformation ratio, and **(c)** object acceleration in gravities.

Mosquitoes may experience life-threatening impacts if flying very low to the ground. Drops impacts in quick succession too pose dangers if the impacts are sufficiently direct to push a mosquito downward. Without sufficient distance to recover from impact, the

insect could strike the ground with the speed of a falling drop or be immersed in pools of water from which it cannot escape. Such an effect was evidenced in our jet and drop chamber experiments. A mosquito which landed into a puddle ultimately perished, not from the impact of drops, but by drowning due to adhesion of its body with the water surface. Although the insect is covered in water-repellent hairs, these hairs do not seem to confer any advantage with respect to the force imparted. The hydrophobicity however may be advantageous in enabling the insect to separate from the drop as is necessary for recovery post-impact. The hairs may also be advantageous in surviving puddles.

It remains unknown whether flying insects can dodge raindrops, given their remarkable abilities to fly sideways and take-off in reverse[11]. Mosquitoes were unable to employ drop-avoidance maneuvers in our experiments. Their maximum flight speed[152] is about 1 m/s, which is far less than the average raindrop speed[145] 6 - 9 m/s. Suppose a mosquito were visually aware of incoming objects within a radius of 10 cm. Given the speed of raindrops, it would have 10 ms to move out of the path of an incoming drop. If the mosquito could achieve half of its maximum speed in avoidance, it would travel a distance of 0.5 cm in 10 ms, which is insufficient to avoid collision in most cases. However, it may make the difference between a direct and a glancing blow.

In this study, we only studied drop impacts from above. If rain falls vertically, the relatively slow flight-speed of mosquitoes will not appreciably increase the frequency of frontal impacts. Even so, it is advantageous for an insect to fly as quickly as possible when flying from one dry area to another through rain to decrease the total number of impacts from above[153].

Studies of aircraft[24–26] and flying animals[17] have shown rain acts to slow flight. In contrast, mosquitoes may be propelled forward by a glancing blow in their hind region. Such events could be a hazardous to the flier when flying close to other objects. Design parameters for MAVs, like those pictured in **Fig.12** may be adapted from the body plan of mosquitoes. For instance, hydrophobicity allows glancing drops to roll off the body

quickly. Sprawled legs create an aerodynamic freeing torque that allows the mosquito to separate from the drop during direct impacts, minimizing the distance pushed upon impact.

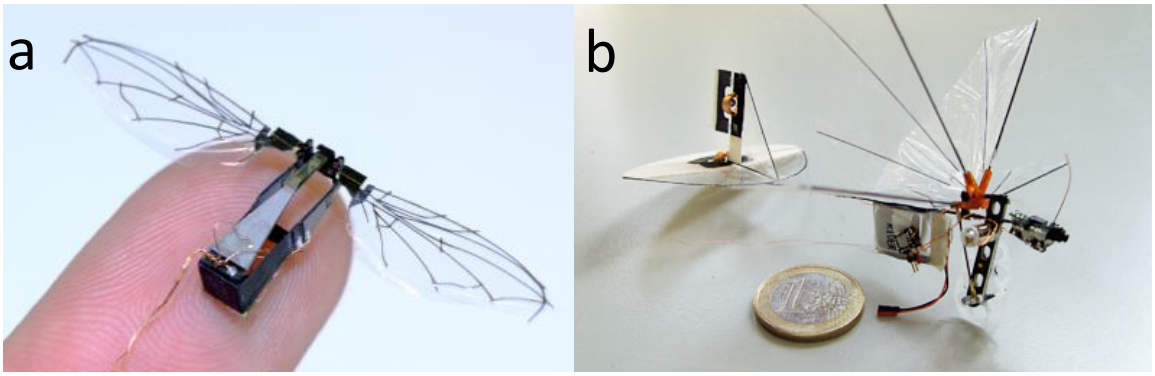

Figure 12: MAVs created by **(a)** R. Wood at Harvard University and **(b)** G. de Croon at the Delft University of Technology.

Calculating impact force using deformation was not possible. Though our experiments show momentum transfer fits theoretical predictions perfectly (**Fig.8**a), we are unable to use deformation data to predict other quantities. Deformation is dependent highly on impact orientation, which is difficult to reproduce consistently, and curvature of insect mimic which our theory lacks.

3.4 Chapter Summary

We perform raindrop impact experiments on free-flying mosquitoes and their mimics. We find mosquitoes can survive, without injury, a collision with a terminal velocity raindrop. Mosquitoes can experience two types of impact, glancing and direct. Glancing impacts, which cause rapid body rotation, vastly reduce impact force. Direct impacts occur when a raindrop impacts a mosquito's center of mass in an inelastic collision, pushing it downward many body lengths. From conservation of momentum, we predict the post-impact velocity of an insect based on its mass for direct impacts. Through a series of videos with similarly sized mimics to mosquitoes, we measure impact acceleration and discover that flying insects with the mass of a mosquito can undergo upwards of 300 g of acceleration upon impact. The acceleration is survivable by mosquitoes because their low mass renders

the impact force minimal, no more than the weight of a small feather. In our supporting theoretical study, we pay particular attention to drop deformation, noting that drops impacting mosquitoes will not splash. Larger insects, and smaller drops, will undergo larger deformations.

CHAPTER IV

RAINDROPS PUSH AND SPLASH FLYING INSECTS

"Rain is grace; rain is the sky descending to the earth; without rain, there would be no life." -John Updike

In this combined theoretical and experimental study, we investigate drop impact onto free bodies of varying mass and size. By varying target mass and size, we are no longer restricted to the pushing impacts observed in Chapter 3. In §4.1, we begin by presenting the observed impact outcomes and corresponding acceleration and forces applied. In §4.2, we proceed with a mathematical model for predicting impact outcomes. We compare these theoretical predictions to our experimental measurements in §4.3, paying particular attention to the prediction of the impact mode outcome and impact force on biological and synthetic flyers. We discuss our theoretical simplifications and avenues for future research in §4.4, and summarize our conclusions in §4.5.

Fig.13 shows the relation between non-dimensional mass m_2/m_1 and effective radius R_2/R_1, where m_1 and R_1 is raindrop mass and radius, respectively, m_2 is the insect mass, and R_2 is taken to be half the wingspan, of 21 insects from literature [123–133]. We find insect wingspan scales with mass as $W \sim m_2^{0.44}$ ($R^2 = 0.91$), where mass spans 1 - 1200 mg and wingspan W spans 2 - 50 mm. In this thesis, we build insect mimics within this range to investigate how the size of insects affects drop collisions.

4.1 Experimental Results

We perform a series of drop impact experiments, filmed using a high speed camera. Drops strike three species of live insects, including mosquitoes, fruit flies and houseflies. In addition, we film the drop impact of 28 insect spherical and cylindrical insect mimics. We

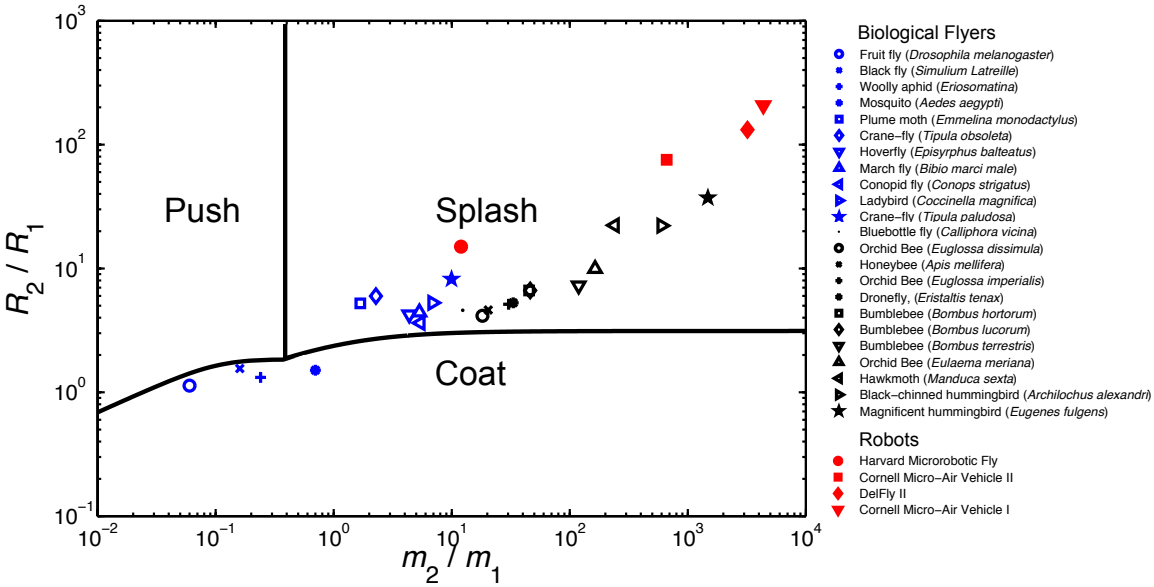

Figure 13: The relation between radius ratio R_2/R_1 and mass ratio m_2/m_1 of insects[123–133] and flying robots[2–4,6]. Boundaries between impact modes are drawn from theory. Insects and robots are listed in order of increasing mass.

categorize the impacts into three distinct modes, pushing, splashing, and coating (Video S2). **Fig.14** shows the observed modes of impact, based upon the mass and size of the mimic. In this section, we introduce each of the modes and provide measurements of the impact force. For the discussion henceforth, we consider an incoming drop of mass $m_1 = 5$ mg, radius $R_1 = 1.1$ mm, and speed u_1. Our choice of raindrop size corresponds to an average raindrop in nature[16,145,154]. The drop collides with a spherical insect of mass m_2 and radius R_2 hovering in mid-air.

4.1.1 Pushing

Mimics of mass less than 3 mg represent the smallest insects, such as mosquitoes, blackflies, and fruit flies, which account for 20% of the mimics considered. These mimics are shown by the seven blue points in **Fig.14**, and the insects they represent by the four leftmost symbols in **Fig.13**. Such insects have less mass than raindrops, but comparable wingspan to a raindrop. (Table 5). Experiments in this mass range reveal that drops, surprisingly, remain intact during impact. **Fig.15**a shows a pushing impact with a 1 mg mosquito; **Fig.15**b

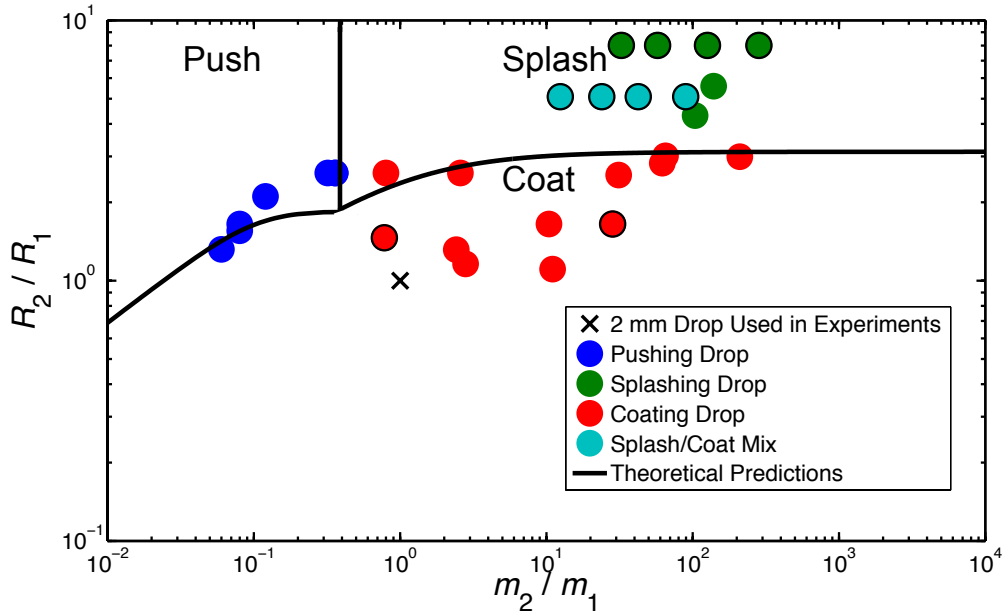

Figure 14: The relation between radius ratio R_2/R_1 and mass ratio m_2/m_1 of insect mimics used in our experiments. Colors of data points, as listed in the legend, represent experimental observations of impact mode. Experiments are performed using a drop of radius $R_1 = 1.1$ mm depicted by the cross. Boundaries between regions are calculated using theory. Black outlines surrounding data points indicate a cylindrical mimic was used, while the data points without borders indicate a sphere was used.

shows a qualitatively similar impact with a styrofoam sphere of mass 0.6 mg.

During impact, the drop is deformed, increasing in radius as much as 80%, but still insufficient to cause breakup, which requires a radius increase[148] of more than 300%. The contact region of the impact remains small, constrained to the top hemisphere of the mimic. After impact, the mimic remains trapped under the drop, and relative motion ceases between the two. Neglecting aerodynamic drag, conservation of linear momentum yields the final velocity u' of the combined mass system is

$$\frac{u'}{u_1} = \left(1 + \frac{m_2}{m_1}\right)^{-1}. \tag{4.1}$$

Thus, the new falling speed of the combined drop-mimic is determined by the masses of each. For the smallest insects, this falling speed is often quite close to the initial raindrop speed. In this regime, fruit flies fall the fastest with 95% percent of the raindrop speed; mosquitoes and black flies the slowest with 80-90% the speed. We will apply the model

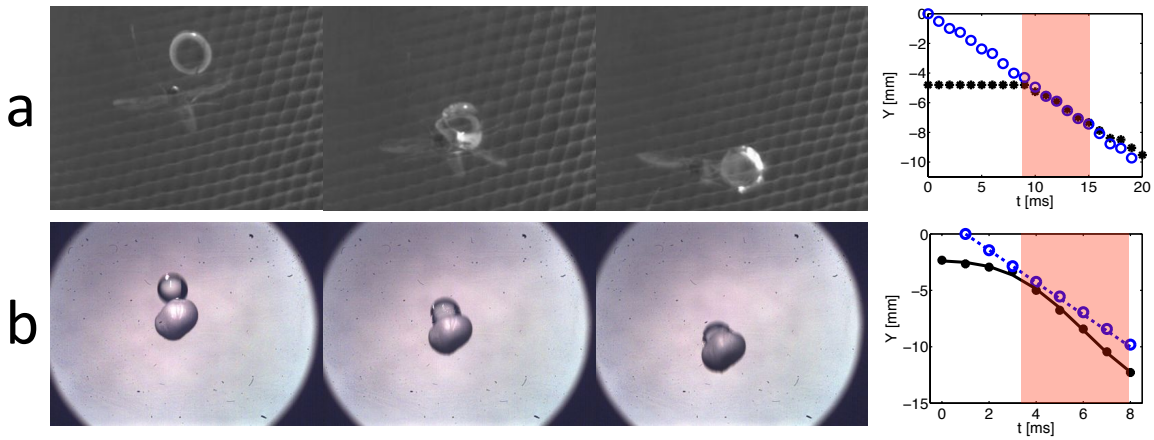

Figure 15: Pushing. (a) A mosquito and (b) a styrofoam mimic pushed downward by a falling drop. The graphs show the time course of position of the targets (black) struck by a drop (blue). The pink shaded area denotes the duration of contact with the drop.

of inelastic impact, given in Eq. (4.1), as an estimate of other drop-mimic speeds in our modeling in §4.

4.1.2 Splashing

The vast majority of insects in **Fig.13** have mass 10 mg to 1 g and wingspans ranging from 2 mm to 50 mm. Examples include the plume moth, crane-fly, and bumblebee. These insects are generally heavier than raindrops and have wingspans much larger than a raindrop diameter (Table 5). **Fig.16**a shows a tethered housefly which causes an impacting drop to shatter. **Fig.16**b shows splashing on a wooden sphere, where the drop begins to break apart prior to the entire drop making contact. This mimic is accelerated only slightly on impact. Mimics which are splashed are denoted by the green points in **Fig.14**.

4.1.3 Coating

Since flying insects are all less dense than water, insects of comparable size to a raindrop, but heavier in mass, do not exist. For the sake of completeness, we investigated the impact of raindrops on objects of mass 1 mg to 1 g but of comparable size to a raindrop (Table 5). Such objects would correspond to an insect standing atop a hard unyielding surface such as

a branch.

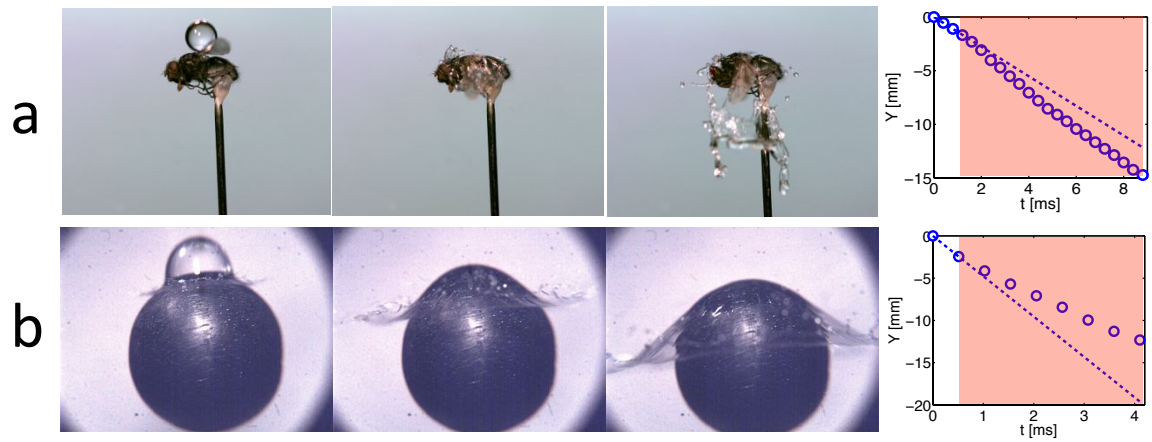

Figure 16: Splashing. (a) A tethered housefly and (b) wooden sphere experiencing a splashing impact. Graphs (a) and (b) show the position (open points) of the bottom edge of a raindrop. The dashed lines show the position of mimic if no impact occurred. The pink shaded area denotes the duration of contact with the drop.

Table 1: Impact mode requirements and characteristics in relation to drop mass m_1 and radius R_1, and target mass m_2 and radius R_2.

Impact Mode	Definition of Mode	Conditions for Mode		Acceleration of Target	Targets	
					Insects	Mimics
Push	drop remains intact	$\frac{m_2}{m_1} \ll 1$	$\frac{R_2}{R_1} \leq 1$	high	mosquitoes, gnats	styrofoam
Coat	drop surrounds object	$\frac{m_2}{m_1} \gtrsim 1$	$\frac{R_2}{R_1} \lesssim 1$	medium - low	tethered fruit flies	metals
Splash	drop fragments upon impact	$\frac{m_2}{m_1} > 1$	$\frac{R_2}{R_1} \gg 1$	negligible	bees, cicadas, dragonflies	woods, metals

One example is shown by the fruit fly tethered to a thin wire in **Fig.17**a. If the insect were untethered, a pushing impact would occur. However, the wire resists the motion of the insect, causing it to be coated by the drop. As shown by **Fig.13**, most insects are too large and lightweight to be coated. Coating impacts would be maladaptive to insects because they increase the surface area in contact with the fluid.

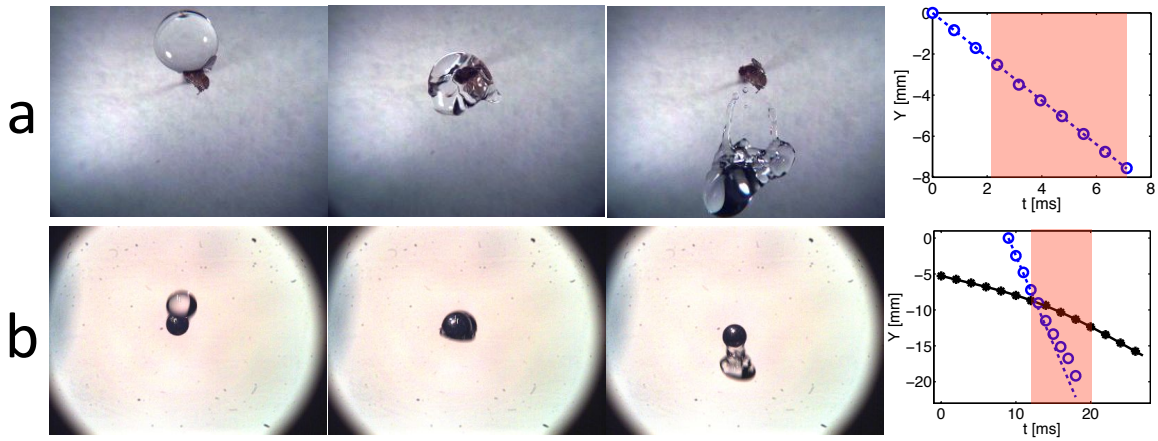

Figure 17: Coating. (a) A fruit fly and (b) steel sphere mimic coated upon impact. Graphs (a) and (b) show the position (open points) of the bottom edge of a raindrop. The dashed lines show the position of mimic if no impact occurred. Closed points show the vertical position of the mimic. The pink shaded area denotes the duration of contact with the drop.

Fig.17b shows an untethered steel sphere coated by a raindrop. The drop flows around the mimic, covering its entire surface before continuing onward. During this process, the 2.2 m/s drop accelerates the mimic only slightly, increasing its velocity from 0.26 to 0.58 m/s. Most of the momentum of the drop is not transferred to the mimic, but instead flows around the target. After striking the object, the fluid re-forms into a drop, momentarily encapsulating the mimic before draining. Mimics which were coated are denoted by the red points in **Fig.14**.

We further recognize a mode of impact which is a combination of splashing and coating, shown by the turquoise points in **Fig.14**. In this mode, part of the drop coats the insect while part splashes, and we denote such impacts as a coating-splashing transition.

Rain is known to capture airborne particles, such as pollen and dust, as it falls[155]. Based on our observations, small particles impacted dead-on by raindrops will be encapsulated by a drop until collision with the ground. One of the very smallest insects, the parasitic wasp with a mass of about 0.03 mg[123], would likely succumb to the same fate.

4.1.4 Impact acceleration

We rate impacts based on acceleration and impact force, which we discuss in turn. **Fig.18** shows the mimic's acceleration in terms of number of gravitational accelerations, $g = 9.81$ m/s^2. Pushing and coating accelerates impacts by 100 - 400 g. The splashing region has much lower acceleration (20 - 50 g). This lower effectiveness of momentum transfer can be observed in the fragmented droplets, continuing downward or radially from the mimic. To give perspective on the magnitude of these accelerations, we note the human[156] limits for acceleration are about 50 g, the limits for fleas[151] jumping are 135 g. In comparison, impact by a falling raindrop can generate even higher accelerations.

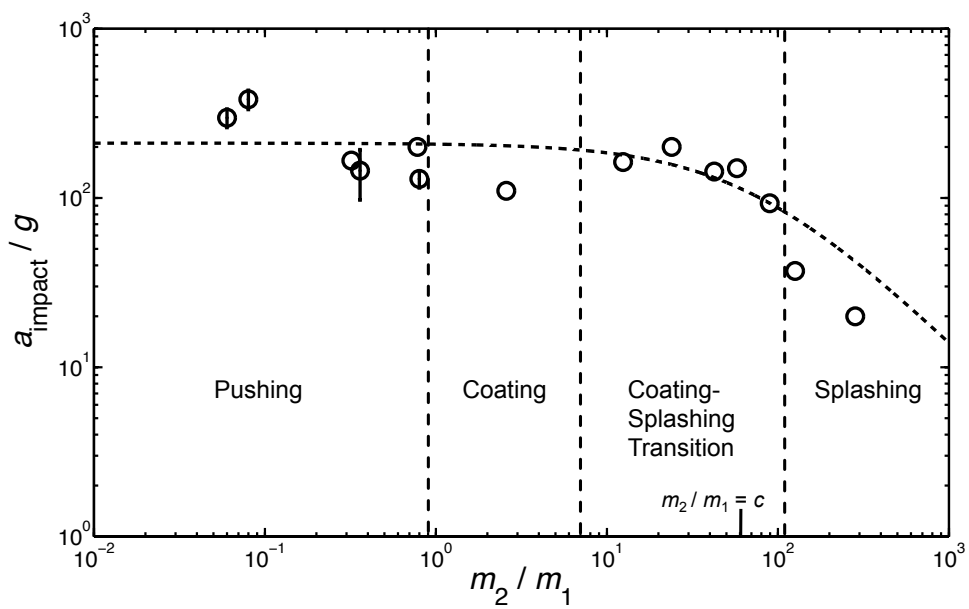

Figure 18: The relation between acceleration in number of gravities a_{impact}/g and mass ratio m_2/m_1, for mimics struck by drops falling at 2.2 - 5 m/s. The line of best fit has R^2 = 0.45. Delineated regions denote impact outcome, based on experimental observation.

The clear trend in **Fig.18** suggests that a scaling is possible. For impact of a drop of constant size and drop speed, we expect the acceleration a_{impact} to scale as the ratio of object speed u' to impact time τ,

$$a_{\text{impact}} = u'/\tau. \tag{4.2}$$

By substituting in Eq. (4.1) for u', a_{impact} scales as

$$a_{\text{impact}} = \frac{1}{\tau}\frac{u_1}{1+m_2/m_1} \sim \frac{b}{c+m_2/m_1}. \tag{4.3}$$

The fitting constants $b = 1.45 \times 10^5$ m/s^2 and $c = 60$ are found using the method of least squares. Although the fit is modest (R^2 = 0.45), the trend line in **Fig.18** encapsulates the trends observed. For mass ratios $m_2/m_1 = 10^{-2} - 10$, which translates to $m_2 = 10^{-4} - 0.05$ g, impact acceleration is roughly constant. After a mass ratio of 10, the acceleration decreases nonlinearly with mimic mass. In particular, an increase in mass ratio by a factor of ten from 20 to 200 causes the acceleration to decrease by a factor of five.

The magnitude of the absolute force provides further insight into the damages that a flying insect may face. Impact acceleration may easily be translated into a maximum impact force F_{impact} such that

$$F_{\text{impact}} = m_2 a_{\text{impact}}. \tag{4.4}$$

Fig.19 shows the relation between maximum force F_{impact} and the mimic-drop mass ratio. Surprisingly, the trend is opposite to the acceleration trend in **Fig.18**, for which the smallest mimics receive the highest acceleration. Instead, here, the heaviest mimics sustain the largest forces ($10^2 - 10^4$ dynes), with the largest force at 4×10^4 dynes. This is close to the maximum force applied by an unyielding surface, $F \sim m_1 u_1/\tau \approx 7 \times 10^4$ dynes. The lightest mimics sustain forces of 100 dynes, indicating that their low mass is effective in reducing the force of impact.

Based on our measurements of impact force, we observe splashing impact is the least effective at transferring momentum. The mimics in the splashing region in **Fig.18** likely experience half of the impact acceleration they would have if the drop had remained intact. In the next section, we present a mathematical model for predicting the mode of impact based on insect size and mass.

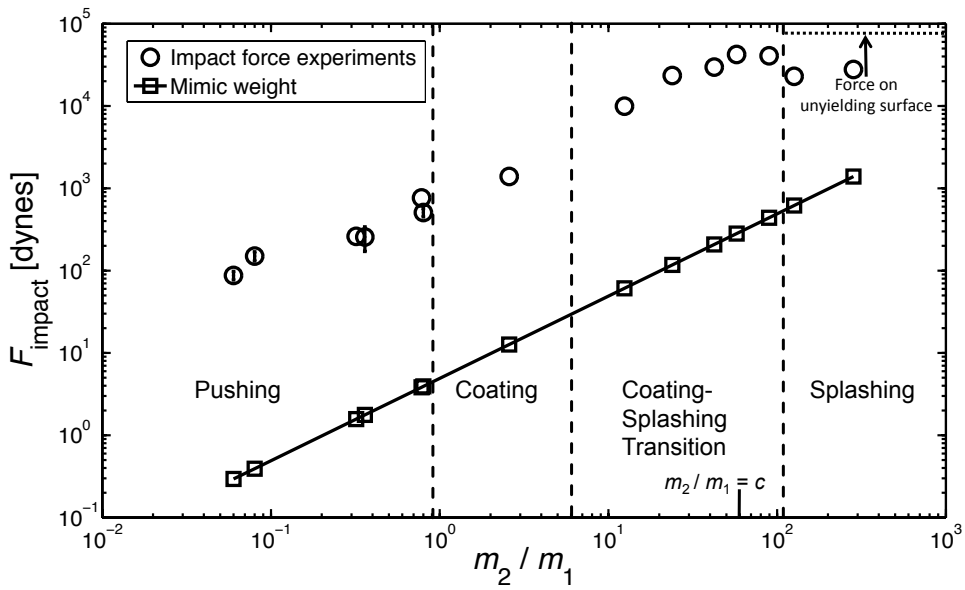

Figure 19: The relation between impact force F_{impact} (circles) and mass ratio m_2/m_1, for mimics struck by drops falling at 2.2 - 5 m/s. The relation between mimic weight (squares) and mimic mass is shown for comparison. Delineated regions denote impact outcome, based on experimental observation.

4.2 Model

In this section, we present a theory for the mass and size range for the three distinct modes of impact, shown graphically in **Fig.20**. In the push regime, the impact is inelastic, and so the kinetic energy may be easily calculated using equation Eq. (4.1). We will use this relation to calculate the conditions for the push-coat and push-splash thresholds. We seek a relation between the object mass and radius that yields an impact that is just on the border of pushing and coating. Our strategy is to use conservation of energy to yield a relation between two regimes. We use a similar method for calculating the conditions distinguishing a push from a splash impact. Lastly, we consider a force balance to investigate the threshold between coating and splashing. In the theory below, this insect is assumed to spherical for simplicity, but modifications can be made for other insect shapes.

4.2.1 Dimensionless Parameters

In the following analysis of raindrop impact onto a free-flying insect, a number of dimensionless groups arise upon non-dimensionalization of our governing equations. The groups

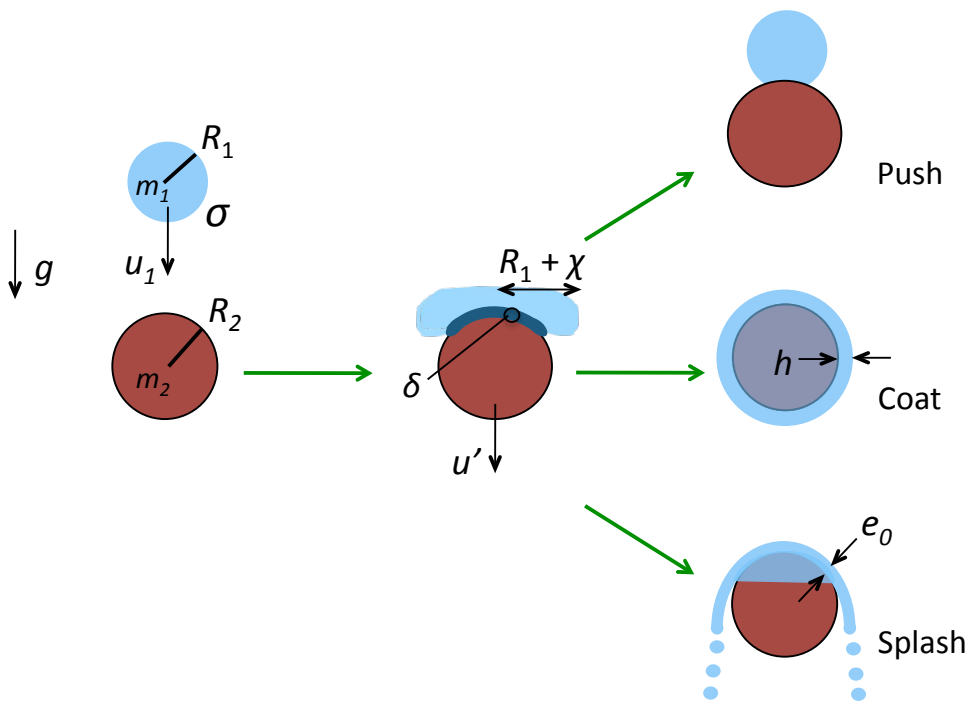

Figure 20: Schematic diagram illustrating drop impact modes. A drop initially strikes the unsupported target, and based on the relative size and speed of the two objects, continues onward to one of three modes of impact. Here we define variables used throughout our analysis, where δ is the boundary layer thickness upon drop deformation, χ is the increase in drop radius, h is the shell thickness of a coating drop, and e_0 is the film thickness during splashing.

are typical of both two-body impact problems, e.g., Equation 1, and in studies of drop impact. The groups include:

$$\begin{aligned} \alpha &= \frac{m_2}{m_1+m_2} = \frac{\text{mimic mass}}{\text{combined mass}} \qquad \beta = \frac{R_1}{R_2} = \frac{\text{drop radius}}{\text{mimic radius}} \\ \mathrm{Re}_1 &= \frac{R_1 u_1}{\nu} = \frac{\text{drop inertia}}{\text{drop viscosity}} \qquad \mathrm{We}_1 = \frac{\rho u_1^2 R_1}{\sigma} = \frac{\text{drop inertia}}{\text{drop surface tension}} \end{aligned} \tag{4.5}$$

The first two groups involve dimensionless groups describing relative masses and sizes of the two bodies. The group α relates the inertia of the insect to the combined inertia of the drop-cum-insect, and emerges upon consideration of the kinetic energy before and after impact. The group β relates the relative sizes of the two objects, which is important in considering surface energy involved. Specifically, β^2 relates the surface areas of the drop to the mimic. The next two dimensionless groups are quite common in drop impact

problems. Reynolds and Weber numbers for the drop size and speed considered in our model are Re_1=5300 and We_1=365 respectively, where the properties of the drop include water density $\rho = 1000$ kg/m^3, kinematic viscosity $\nu = 10^{-6}$ m^2/s, and surface tension $\sigma = 72.8$ dynes/cm. The Reynolds number is used in calculation of dissipated energy within the boundary layer within the drop as is strikes the mimic. The Weber indicates the importance of the drop's inertia to capillarity. In studies of impact on unyielding surfaces, large Weber number typically indicates splashing[29]. However, in the case of impact on a free target of variable mass, the outcome depends on the mass and size of the object as we determine in the analysis below.

4.2.2 Push-Coat Threshold

We employ an energy balance on the drop before and after impact[157,158] to predict the transition from a drop's pushing its target downward to the drop coating its target. Denoting the post-impact energy using primed notation, conservation of energy states

$$\underbrace{E_k + E_p + E_s}_{\text{before impact}} = \underbrace{E_k^{'} + E_p^{'} + E_s^{'} + E_d^{'}}_{\text{after impact}}, \tag{4.6}$$

where E_k, E_p, E_s, and E_d are kinetic, potential, surface, and dissipative energies, respectively. Mass conservation dictates the mass of the drop remains unchanged throughout the impact: namely, $m_1 = m_1'$. We take $E_p = E_p^{'}$ by assuming the drop does not substantially change in elevation with respect to the target just prior to and after the collision.

At the border of coating and pushing, the impact is inelastic and the drop surrounds a spherical target and remains adhered as in **Fig.20**. Initial kinetic and surface energies, E_k and E_s, remain unchanged for all impacts. We calculate E_s' and E_d' based upon the lowest-energy coating scenario, considering the flows that occur as the drop deforms from a sphere to an spherical shell coating the mimic. At conditions away from this threshold, the assumptions we have made about drop deformation and impact kinetics become inaccurate. We therefore define a term which captures the error in our calculation of the energy balance

in Eq. (4.6), given by

$$\Delta E = E_k + E_s - E_k^{'} - E_s^{'} - E_d^{'}. \tag{4.7}$$

The sign of ΔE determines which impact mode will be witnessed. During pushing, the drop does not form a complete spherical shell around the mimic, and so our method overestimates the surface E_s', and dissipative E_d', energies. Thus we expect the error ΔE to be negative if the impact is a push. Conversely, a faster incoming drop would flow around the target and continue past it as in **Fig.17**. This would lead to more residual kinetic energy E_k' than that calculated using an inelastic impact, and so an underestimated E_k'. Thus, we expect the error ΔE to be positive if the impact is a coat. Together, our relation for distinguishing pushing from coating is:

$$\Delta E \begin{cases} < 0 \ \text{ push} \\ > 0 \ \text{ coat} \end{cases} \tag{4.8}$$

To complete this analysis, we now write relations for all the terms in Eq. (4.7). The initial kinetic and surface energies of the system may be written as that of a spherical drop,

$$E_k = \frac{1}{2} m_1 u_1^2, \tag{4.9}$$

$$E_s = 4\pi\sigma R_1^2, \tag{4.10}$$

where ρ and σ are the density and surface tension of water. These energies are converted into several terms throughout the impact process, including the final kinetic and surface energies of the drop-cum-mimic, and the irrecoverable dissipation during impact. We now estimate these final energies of the system post-impact.

The final kinetic energy is estimated as that for inelastic impact,

$$E_k^{'} = E_{k,\text{inelastic}} = \frac{1}{2}\left(m_1 + m_2\right)\left(u'\right)^2, \tag{4.11}$$

where we use Eq. (4.1) to substitute for u'. This equation represents the greatest possible kinetic energy change for the system, as inelastic impact slows the drop more than other

impact types. This estimate will be accurate for pushing, but will be an underestimate for high-speed coating flows in which the fluid continues flowing past the mimic.

We write the final surface energy as that associated with a spherical shell surrounding its target as illustrated by **Fig.20**. This surface energy is comprised of the energy in the solid-liquid surface and the air-liquid surface,

$$E_s^{'} = \underbrace{4\pi\sigma R_2^2(1-\cos\theta)}_{\text{solid-liquid surface}} + \underbrace{4\pi\sigma\left(R_1^3+R_2^3\right)^{\frac{2}{3}}}_{\text{air-liquid surface}} \tag{4.12}$$

where θ is the contact angle of water on the target.

Viscous dissipation arises from the drop's deformation upon impact. The time-scale of deformation is $\tau \approx 2R_1/(u_1-u')$. To calculate dissipation, we apply a method, by Pasandideh-Fard[157] and Mundo[158], for estimating dissipation during impact of drops onto flat surfaces. Dissipation occurs as the fluid undergoes shear within the boundary layer. Using stagnation point flow, this layer can be estimated to be of thickness[157]

$$\delta = 4R_1/\sqrt{\mathrm{Re}}, \tag{4.13}$$

where the Reynolds number Re $=R_1(u_1-u')/\nu$. The viscous dissipation per unit mass[38] is

$$\Phi = \mu\left(\frac{\partial v_i}{\partial x_j}+\frac{\partial v_j}{\partial x_i}\right)\frac{\partial v_i}{\partial x_j} \approx \rho\nu(u_1-u')^2/\delta^2. \tag{4.14}$$

The volume of the boundary layer is approximated by considering the deformation of a drop into a spherical shell that encapsulates the impacted object. At the end of the impact, the drop assumes a spherical shell of thickness

$$h = (R_1^3+R_2^3)^{\frac{1}{3}} - R_2. \tag{4.15}$$

We model this process as the flattening of a drop of radius R_1 to

$$R_{\max} = \sqrt{4R_2^3/3h}, \tag{4.16}$$

where $R_{\max}$ is the effective radius of a disc of height h and the original volume of the drop. The volume of fluid over which dissipation take place is approximated by

$$\Omega \approx \pi R_{\max}^2\delta. \tag{4.17}$$

The total dissipation, $E_d^{'}$, within the drop is

$$E_d^{'} = \int_0^{\tau} \int_{\Omega} \Phi \, \mathrm{d}\Omega \, \mathrm{d}t \approx \Phi \Omega \tau. \tag{4.18}$$

The energy lost due to viscous dissipation may be approximated by substituting Φ, Ω, and τ into Eq. (4.18), yielding

$$E_d^{'} = \frac{1}{2} \rho \nu \pi R_{\max}^2 \left(u_1 - u'\right) \sqrt{\mathrm{Re}}. \tag{4.19}$$

By substituting Eqs. (4.9) to (4.12) and (4.19) into Eq. (4.6) and rearranging, we arrive at

$$\begin{aligned} \Delta E = \frac{1}{2} \left[m_1 u_1^2 - (m_1 + m_2)(u')^2\right] + 4\pi\sigma \left[R_1^2 - R_2^2 (1 - \cos\theta) - \left(R_1^3 + R_2^3\right)^{\frac{2}{3}}\right] \\ - \frac{1}{2} \rho \nu \pi R_{\max}^2 \left(u_1 - u'\right) \sqrt{\mathrm{Re}} \end{aligned} \tag{4.20}$$

where m_2 and R_2 are the only non-constant terms.

We may non-dimensionalize Eq. (4.20) by dividing by $\rho \pi u_1^2 R_1^3$, yielding a dimensionless energy

$$\Delta E^* = \alpha \left[1 - \frac{(\mathrm{Re}_1)^{-\frac{1}{2}}}{\beta(\beta^3 + 1)^{\frac{1}{3}} - \beta}\right] + \frac{6}{\mathrm{We}_1} \left[\cos\theta - (1 + \beta)^{\frac{2}{3}}\right], \tag{4.21}$$

where our push-coat criteria as

$$\Delta E^* \begin{cases} < 0 \ \text{ push} \\ > 0 \ \text{ coat.} \end{cases} \tag{4.22}$$

Eqs. (4.21) and (4.22) are physically consistent in light of limits of dimensionless groups involved. Note the second term in Eq. (4.21) is negative because $0^\circ < \theta < 180^\circ$. Thus, for very low inertia or very high surface tension, $\mathrm{We}_1 \to 0$, ΔE^* decreases, indicating that pushing the target is now favorable. In the limits of either high viscosity, $\mathrm{Re}_1 \to 0$, or for superhydrophobic targets, $\cos\theta \to -1$, the dimensionless energy ΔE^* decreases, promoting pushing. We plot the curve given by Eq. (4.21) in **Fig.14** to predict the threshold between pushing and coating, by specifying values of m_2/m_1 and plotting values of R_2/R_1 for which $\Delta E^* = 0$. No free parameters are employed in computing the push-coat transition Eq. (4.20).

4.2.3 Push-Splash Threshold

In the previous section, we determine the threshold between the push and coat modes. In coating, we assume the drop completely coats its spherical target. In this section, we use observations from our experiments to make several modifications to this physical picture to consider splashing. First, more residual kinetic energy remains in splashing than in coating at the end of the impact. Second, splashing coats the target less than a coating impact.

In this section, we calculate the final kinetic energy $E_k^{'}$ using an inelastic impact model, and the final surface $E_s^{'}$ and dissipative $E_d^{'}$ energies using a model for drop deformation, or flattening, upon impact. If the drop's initial kinetic E_k and surface E_s energies are too high to be absorbed into surface energy and dissipation, the drop will splash. Our model for $E_k^{'}$, $E_s^{'}$, and $E_d^{'}$ becomes invalid if the drop breaks apart, but remains valid if the drop stays intact.

We begin with Eq. (4.18) as before, but consider instead the boundary layer volume $\Omega \approx \pi (R_1 + \chi)^2 \delta$ occupied by a disk of radius $R_1 + \chi$ and height δ. We apply a method we previously used to model the deformation of a drop upon a sphere[117]. Impact increases the radius R_1 by an amount χ,

$$\frac{\chi}{R_1} \sim \sqrt{\mathrm{We}_1} \left(\frac{m_1}{m_2} + 1 \right)^{-1}. \tag{4.23}$$

A more detailed derivation of Eq. (4.23) may be found in Dickerson *et al.*. (2012). We use a scaling factor is 0.7. Combining Eq. (4.23) with Eq. (4.18), and now using $R_1 + \chi$ in place of $R_{\max}$ to determine the volume of dissipating fluid Ω, we arrive at the dissipation

$$E_d^{'} \approx \Phi \Omega \tau \sim \frac{1}{2} \rho \nu \pi (R_1 + \chi)^2 \left(u_1 - u' \right) \sqrt{\mathrm{Re}}. \tag{4.24}$$

Assuming the drop flattens into a disc upon impact, we estimate the final surface energy as the sum of the solid-liquid energy and the air-liquid energy,

$$E_s^{'} = \pi \sigma (R_1 + \chi)^2 (2 - \cos \theta). \tag{4.25}$$

Combining Eqs. (4.9) to (4.11) and (4.23) to (4.25) for the push-splash threshold, we may rewrite Eq. (4.7) as

$$\Delta E = \frac{1}{2}\left[m_1 u_1^2 - (m_1+m_2)(u')^2\right] + \pi\sigma\left[4R_1^2 - (R_1+\chi)^2(2-\cos\theta)\right] \\ -\frac{1}{2}\rho\nu\pi(R_1+\chi)^2\left(u_1-u'\right)\sqrt{\mathrm{Re}} \tag{4.26}$$

where m_2 is the only non-constant term.

We may non-dimensionalize Eq. (4.20) by dividing by $\rho\pi u_1^2 R_1^3$, yielding a dimensionless energy

$$\Delta E^* = \frac{2}{3}\alpha + \frac{4}{\mathrm{We}_1} - \left(1+2\alpha\sqrt{\mathrm{We}_1}+\alpha^2\mathrm{We}_1\right)\left[\frac{2-\cos\theta}{\mathrm{We}_1} + \frac{\alpha^{\frac{3}{2}}}{2\sqrt{\mathrm{Re}_1}}\right], \tag{4.27}$$

and our push-splash criteria as

$$\Delta E^* \begin{cases} < 0 \ \text{ splash} \\ > 0 \ \text{ push.} \end{cases} \tag{4.28}$$

In Eq. (4.27), we can reason that as m_1 increases, the corresponding decrease in the combined mass ratio α will increase ΔE^*, promoting pushing. This is consistent with our experiments, in which decreasing m_2/m_1 produces smaller drop deformations and subsequently, pushing[117]. Similarly, as the target becomes more hydrophobic, $\cos\theta \to -1$, ΔE^* will decrease, promoting splashing. We plot the vertical line given by Eq. (4.27) in **Fig.14** to predict the threshold between pushing and splashing, by specifying values of m_2/m_1 for which $\Delta E^* = 0$. Unlike the previous section, the energy balance given in Eqs. (4.26) and (4.27) has no dependence on R_2/R_1. Such a result occurs because we assume drop deformation is unaffected by mimic size in Eq. (4.23). We justify this approximation in the regime in which mimic radius exceeds drop radius ($R_2/R_1 > 2$), which is the reason of interest, as shown in **Fig.14**.

4.2.4 Coat-Splash Threshold

At the threshold of coating and splashing, the drop deforms beyond a point where pushing is possible. The drop flattens sufficiently that it forms a thin film on the top of the target,

after which two outcomes can occur: it can remains adhered, creating a coat, or shed off in a ligament or drops, creating a splash. Consideration of attachment or separation from the target's curved surface is a solved problem called the teapot effect[159]. To determine the conditions for distinguishing a coat from a splash, we consider a force balance between inertial and adhesive forces for the flow around a curved surface[160].

Duez *et al.*(2010) report a critical Weber scaling that characterizes the transition between fluid attachment and separation. We apply their theory using the relative velocity between drop and mimic, $u_1 - u'$ and the length scale given by the film thickness $e_0 \simeq R_1^2/2R_2$, estimated from the Bernoulli equation, to define a Weber number,

$$\mathrm{We}^* = \frac{\rho\left(u_1 - u'\right)^2 e_0}{\sigma}. \tag{4.29}$$

A radial force balance equates centrifugal forces with the adhesion forces of the fluid to the sphere. This force balance can be written in non-dimensionalized form

$$\mathrm{We} \propto \frac{R_2^2}{e_0^2}\left(1+\cos\theta\right) \tag{4.30}$$

During splashing, inertial forces dominate and so Weber number is above the critical value above. Thus,

$$We \begin{cases} < R_2^2\left(1+\cos\theta\right)/e_0^2 & \text{coat} \\ > R_2^2\left(1+\cos\theta\right)/e_0^2 & \text{splash.} \end{cases} \tag{4.31}$$

By equating expressions for We given by Eqs. (4.29) to (4.31), we write the condition for splashing,

$$R_2 < \left[\frac{\rho R_1^6\left(u_1 - u'\right)^2}{\sigma\left(1+\cos\theta\right)}\right]^{\frac{1}{5}} \tag{4.32}$$

We may non-dimensionalize Eq. (4.32) by dividing by $\rho\pi u_1^2 R_1^3$, yielding a radius ratio

$$\frac{R_2}{R_1} < \left[\frac{\alpha^2 \mathrm{We}_1}{\left(1+\cos\theta\right)}\right]^{\frac{1}{5}} \tag{4.33}$$

A drop with a very high initial velocity, producing a large We_1, and a target with a hydrophobic surface such that $\cos\theta \to -1$, promotes splashing by increasing the right-hand-side of Eq. (4.33). We plot the curve specified by the threshold given in Eq. (4.33) by

specifying values of m_2/m_1 and plotting values of R_2/R_1, which satisfy the equality. No scaling coefficient was required to shift the curve to the intersection of the curves plotted by Eqs. (4.21) and (4.27).

4.3 Comparison of theory to experiment

Previously, we presented implicit equations, Eqs. (4.21), (4.27) and (4.33), for the mass-radius coordinates of each impact mode. We use Mathematica to numerically solve these equations by inputing a mass ratio m_2/m_1 and calculating a corresponding radius ratio R_2/R_1 which solves the equations. Although insects are hydrophobic, we perform experiments with hydrophilic mimics. Thus, we assume in our calculations that the contact angle of water on the mimics is $\theta = 80°$.

We have freedom to choose where to terminate each curve, and so we terminate curves given by Eqs. (4.21) and (4.27) at their point of intersection. For the push-splash transition, in Eq. (4.23), we use a free parameter of 0.7. As shown in **Fig.14**, our theoretical predictions for impact mode match well our experimental observations. Only a few points stray from their predicted zones. We proceed to use our findings to predict impact phenomenon on organisms.

4.3.1 Predictions for insects and flying robots

Fig.13 shows the predicted impact modes for various insects. The model predicts that insects above 100 mg will splash, which seems quite feasible. Inaccuracies are due to our modeling the insect wing, which is flat, as a curved surface. Consequently, the smallest insects lie at the coating-pushing border rather than within the push regime. Mosquitoes in particular are known to be pushed by raindrops[117]. Another inaccuracy is in the coat regime: four insects lie just within the coat regime rather than within the push regime.

We apply our model to predict the effects of raindrop impact on flying robots. We consider four robots, including Harvard's Microrobotic Fly, Cornell's Micro-Air Vehicles I-II and the Delfly[2–4,6], whose mass and half their wingspan is given in **Fig.13**. All robots

are within the splashing zones. Pushing is not possible, as the robots are $2-4$ orders of magnitude too heavy, and 1-2 orders of magnitude too large. Most would need radii two orders of magnitude less than their current values to be in danger of coating. The Harvard micro robotic fly is most in danger of coating: if its wingspan were 3 mm rather than 1 cm, its wings would be coated by the drop. In fact, it is likely that parts of the body which are more slender than the wings will be coated if they are struck by a drop.

4.3.2 Acceleration and force resistance for small and large insects

We now consider the effects of scaling on the effect of raindrop. Scaling is particularly useful as flying insect masses range over 6 orders of magnitude, and synthetic flyers span an additional order of magnitude.

We consider two regimes, the limit of very lightweight and very heavy insects. Small insects have an impressive ability to survive very large accelerations. For example, fleas can survive 135 g during jumping, a mosquito 300 g during raindrop impact[117]. This increasing tolerance to acceleration at small sizes can be explained using scaling.

Fig.4.3 shows that impact accelerations a_{impact}/g asymptote to a constant value of 250 gravities for small sizes. This value arises from consideration of Eq. (4.3), for which the acceleration due to drop impact,

$$a_{\text{impact}} \approx \frac{b}{c+m_2/m_1} = \frac{b/c}{1+m_2/cm_1}. \tag{4.34}$$

For small insects, which have a mass $m_2 \ll cm_1 = 0.3$ g, the acceleration due to drop impact approaches a constant, $b/cg \approx 250$ gravities. Although this acceleration is high, smaller insects, are relatively more capable of surviving accelerations. This increasing strength at small sizes is due to the strength scaling of materials, observed first by Leonardo da Vinci, and reported by McMahon[161] and Schmidt-Nielson[162]. Materials have a constant yield stress, and so the maximum force F_{material} a material can withstand scales as its cross-sectional area, $F_{\text{material}} \sim m_2^{2/3}$. Using Newton's second law, $F_{\text{material}} = m_2 a_{\text{material}}$, the impact acceleration a material can withstand scales as $a_{\text{material}} \sim m_2^{-1/3}$. As insects become

smaller, the maximum acceleration a material can withstand will exceed that provided by a raindrop: $a_{\text{material}} > a_{\text{impact}}$. Thus, smaller insects are invincible with respect to acceleration caused by drop.

As insects increase in size, the force of raindrop impact becomes small compared to both the insect weight and the force their materials can withstand. **Fig.19** shows that as an insect grows larger, the force from a raindrop asymptotes to a constant value of 10^4 dynes. This results from consideration of Eq. (4.4), for which the force due to drop impact,

$$F_{\text{impact}} \approx \frac{bm_2}{c + m_2/m_1} = \frac{bm_2 m_1}{cm_1 + m_2}. \tag{4.35}$$

For large insects, which have a mass $m_2 \gg cm_1 = 0.3$ g, the force due to drop impact F_{drop} approaches a constant, $bm_1 \approx 7 \times 10^4$ dynes. This scaling is adaptive for larger insects, which become relatively more capable of surviving force. The force of raindrop impact will be exceeded by both an insect's weight, scaling as m_2, and the force its materials can withstand, which scale as as $m_2^{2/3}$. A small bird with mass $m_2 = bm_1/g = 74$ g receives an impact force equal to its weight. A Ladybird of mass 2 g receives an impact force 1/10 of its weight.

4.4 Discussion

Our experiments involve several assumptions and simplifications which we review here. Since fast drops cannot be easily aimed at our mimics, we employ drops of speed $u_1 = 2.2 - 5$ m/s, which is $45 - 75\%$ slower than a terminal-velocity raindrop. Experiments conducted with terminal raindrops would produce modifications to regimes in **Fig.14**. Specifically, coating and splashing would occur for lower radius R_2 and mass m_2 values. In addition, the acceleration and force on an insect will increase (**Fig.19**), as a greater amount of momentum is available for transfer to the object. Lastly, we assume only spherical drops of fixed size. However as discussed by Reyssat (2007), raindrops have a range of size and shape. In particular, our transition lines in **Fig.14** may not be robust to changes in drop shape.

Wings and legs increase the force of raindrop impact by increasing the insect's aerodynamic resistance. During the high accelerations applied, these structures provided added mass to the insect and shift points to the right in **Fig.13** and **Fig.14**. Insects with the largest wings for their size such as butterflies will experience the greatest deviation from the predicted trends. Wings induce splashing at mass values smaller than predicted in **Fig.13**.

Behavior of the insect will not likely influence impact force. The maximum speeds of most insects is less than 10 m/s, the terminal speed of a falling raindrop[163]. Even at slow flight speeds, however, the formation of a boundary layer as a result of wing motion may help to dispel the smallest drops. The boundary layers formed on discs spinning at exceedingly high speed may prevent drops from impacting the surface[164].

In this study we consider the impact outcome of a raindrop striking an insect. Conversely, one might consider the fate of the insect during impact: does it fragment or splash upon striking an incoming object? From our experiments and theoretical analysis in §5.2, we conclude that an insect will not break apart from the force of a raindrop impact. However, as we know from common experience, insect splashing does occur upon impact with automobiles. This splashing is due to the high impact force imparted by the high momentum of the automobile. For example, if a 2-mg mosquito is struck by an automobile traveling at 15 mph = 6.7 m/s, it will experience an impact force of 9,000 dynes, which is comparable to the force required to kill a mosquito. Larger insects may even splash. If that same car strikes a 1-cm long 0.3 g insect, which is 150 times heavier than a mosquito, the insect will experience an impact force of 240,000 dynes. A car traveling at higher speeds would generate even higher impact forces, which explains why a car driving at 50 mph is often covered with dead splattered insects.

4.5 Chapter Summary

We perform raindrop impact experiments on free-flying insects and their mimics. By systematically varying the size and mass of the mimics, we observe three distinct impact

modes which we refer to as pushing, splashing, and coating. In our supporting theoretical study, we derive mathematical relations which bound each impact regime based on the target's mass and size. These regimes are consistent with our experimental observations. The push-coat and push-splash transitions are determined from consideration of energetics, whereas the coat-splash transition is determined from the balance of centrifugal and adhesive forces.

Our study shows how the experience of flying in the rain is strongly affected by body size. The lightest mimics experience the highest impact accelerations of 300 g, but the lowest absolute forces of 100 dynes. Conversely, the heaviest mimics experience the lowest accelerations of 20 g, but the highest impact forces of 4×10^4 dynes. Based on our experiments with both mimics and insects, we predict insects smaller than 2 mg are pushed by raindrops, whereas larger insects cause raindrops to splash. Consequently, a modern MAV causes raindrops to splash, and should be designed to withstand this force and to contend with splashes shed on its body.

We also identify a sub-optimal size for which objects are most poorly suited for coping with rain. Objects experience both peak acceleration and peak force at a critical mass of 0.3 g, about the weight of a bumblebee. Biological organisms and synthetic flyers should avoid this mass if they are to minimize acceleration and force due to rain.

CHAPTER V

FOG DISRUPTS MOSQUITO FLIGHT DUE TO INCREASED AERODYNAMIC DRAG ON HALTERES

"I've just been bitten on the neck by a vampire... mosquito. Does that mean that when the night comes I will rise and be annoying?" - Vera Nazarian

Half of the world's population resides in regions where malaria transmission is a risk [165]. In 2010, approximately 216 million clinical malaria episodes resulted in an estimated 655,000 deaths. Transmission of malaria to humans occurs through the bite of an infected female mosquito. In this chapter we probe the limits of flight ability of *Anopheles freeborni* mosquitoes in heavy fogs hyperdense air. Our experimental methods for insect handling and imaging are provided in Chapter 2. In §5.1, we present our measurements of the likelihood and promptness of flight failure in heavy air, a calculation of the aerodynamic forces involved. To show such forces are sufficient to perturb halteres, we laden them with additional mass. In §5.2, we present a discussion of our results and avenues for future work, and summarize our main points in §5.3.

5.1 Experimental Results

5.1.1 Flight failure in fog and heavy gas

We performed hundreds of experiments with male and female *Anopheles freeborni* flying in both fog and 38 mixtures of gas with various densities. Fog here refers to the output from a commercial humidifier, consisting of $5-35$ μm diameter water droplets. The microscopic droplets act to increase the aggregate fluid density through which a mosquito flaps. We define flight failure as a rapid descent to the ground and the subsequent inability to resume

flight. Failure is observed when a mosquito encounters a stream laden with fog particles or when introduced to a quiescent medium with suspended fog particles. Landing on the floor of a container is atypical behavior, as mosquitoes prefer to land on walls and ceilings, despite the species[166]. We observe less than 10% of individuals from a group (number of trials, N = 20) of *Anopheles freeborni* choose to rest on the floor of their container under normal conditions.

Every case of flight failure (N > 100) involves pitching (**Fig.21**c, Video S3) or rolling (**Fig.21**d, Video S4), generating inversion or steep angles of orientation with respect to the horizontal flight position. When mosquitoes have rotated 90° relative to vertical, the lift generated by wings cannot maintain their position and they quickly begin falling downward. In other instances, the mosquito maintains its typical orientation and even generates lift in fog, or heavy gas, for fractions of a second, as shown by the upward flight in Videos S3, S4, and S5. Nevertheless, these periods of normal flight, which occur in approximately 10% of the flights filmed, are so sporadic and unstable that mosquitoes inevitably fall to the floor within seconds of introduction of heavy gas. Fog particle deposition on the wings or body is not the cause of flight instability, as we observe flight may resume immediately after fog particles are removed from the air, and that a mosquito blanketed with small drops on its wings and legs retains the ability to fly in dry air.

Mosquitoes behave similarly in both fog and heavy gas, indicating increasing the aggregate density of the medium is the cause of flight failure, rather than the particulate nature of fog. A heavy gas with the same average density as fog causes nearly identical flight failure, as shown in Video S5. Heavy gas is also transparent, indicating that the opacity of the medium and occlusion of vision is not a factor in their flight failure. In **Fig.22**a,b we present flight tracks for mosquitoes in normal air and hyperdense air, respectively. As demonstrated by the flight track in **Fig.22**a, a mosquito can remain aloft for more than 4 seconds before landing in normal air. Conversely, in hyperdense air, the descent behavior is clearly distinct. **Fig.22**b shows the mosquito falls quickly from the ceiling to the floor of

the container. The mosquito falling in the most dense gas (red) shows the least control over flight, falling at an average falling speed of 27 cm/s over 0.55 s.

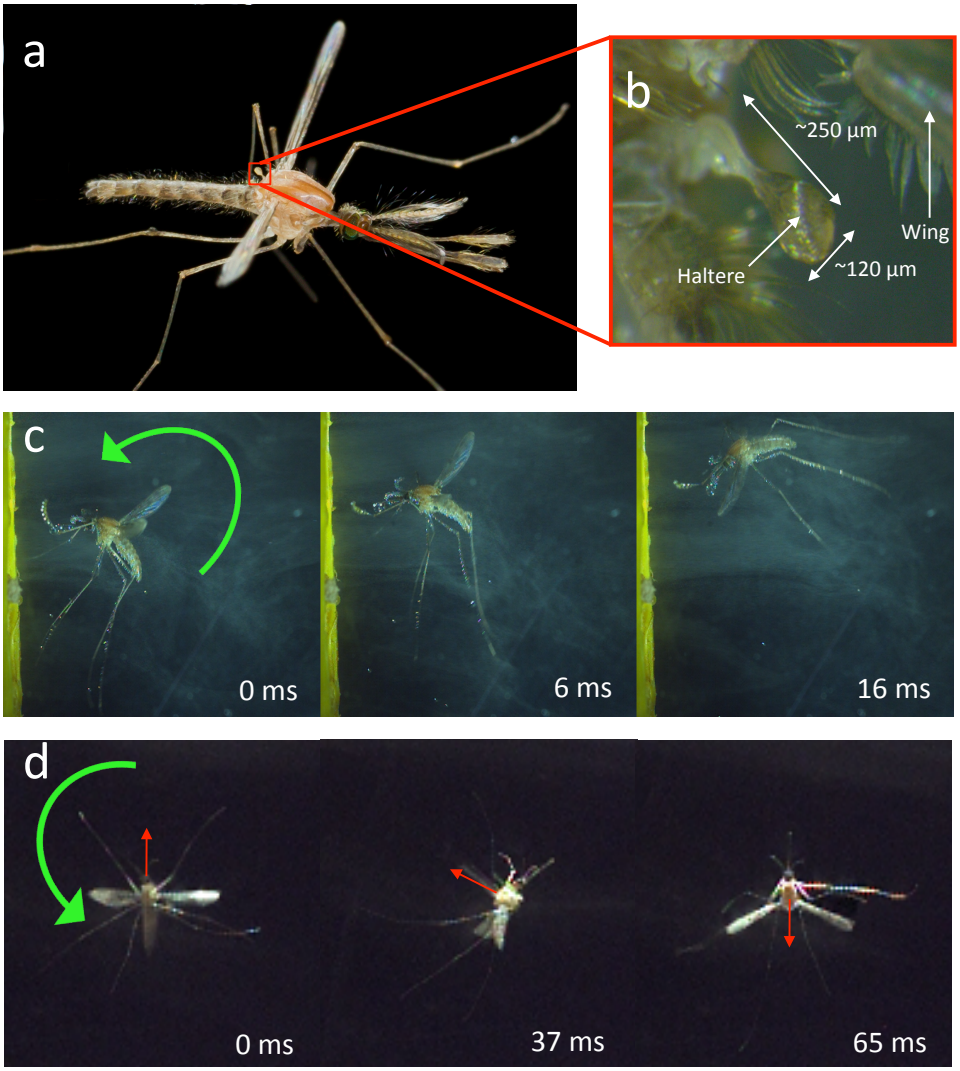

Figure 21: **(a)** An *Anopheles freeborni* mosquito in flight. The location of mosquito's haltere boxed in red. **(b)** A mosquito haltere. A video sequence of a mosquito pitching forward **(c)** and rolling **(d)** while aloft in a stream of fog particles. The red arrow denote the directingon normal to the mosquito's back.

We measured the flight time before grounding when the mosquito is dropped from a height $H = 15$ cm, in air made heavier by the addition of R134a. Humidifier fog was not employed in this experiment due to its propensity for settling and aggregating on container walls. **Fig.23**a shows descent time becomes both shorter and more predictable with increasing gas density. The fastest possible descent time is $T = 0.11$ s, the time needed to fall

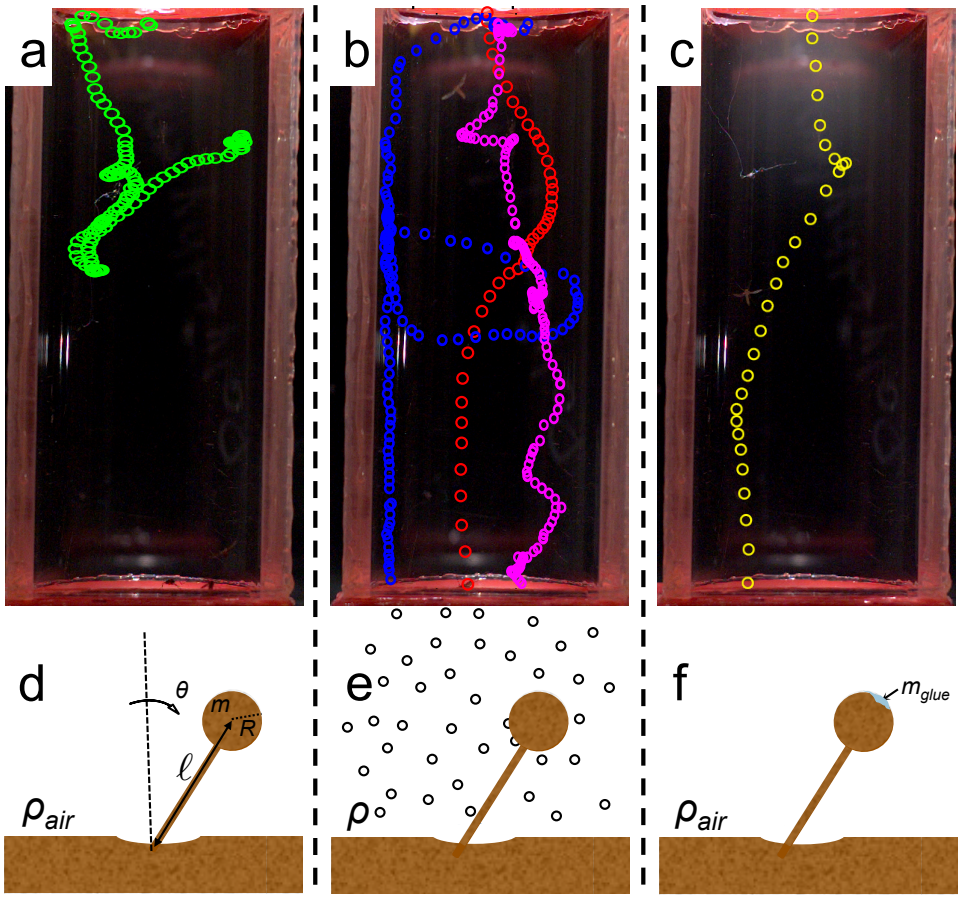

Figure 22: Three columns designate flight in normal air, fog or dense gas, and flight with glue on halteres respectively. Flight tracks **(a-c)** for a mosquito flying in normal air (a); in gas of density $\rho = 1.75$ (blue), 1.9 (pink), 2 (red) kg/m^3 (b); with glue deposited on its halteres (c). Schematics **(d-f)**of haltere flapping in normal air (d), in fog or heavy gas (e), with glue deposited on the tip (f).

a distance H at terminal velocity, 136.5 $\pm$ 9.5 cm/s (N=10). The shortest descent times observed are twice this minimal time, indicating mosquitoes are creating drag by attempting flight. During descent, mosquitoes flap their wings at varying frequencies (150 – 400 Hz), but continue to fall on their sides or inverted.

Fig.23b shows the relation between gas density and proportion of mosquitoes able to sustain flight for over 3 seconds. Over an intermediate range of gas density, 0.9 – 1.6 kg/m^3, or $\pm$ 0.4 kg/m^3 from standard density, mosquitoes can stay aloft indefinitely. The corresponding success rate in this range is slightly less than 100% because of experimental error. In our experiments, we do not control for initial orientation of the mosquito. Thus, a

few mosquitoes are released upside-down entry into the container and, if unable to recover in less than one second, strike the ground.

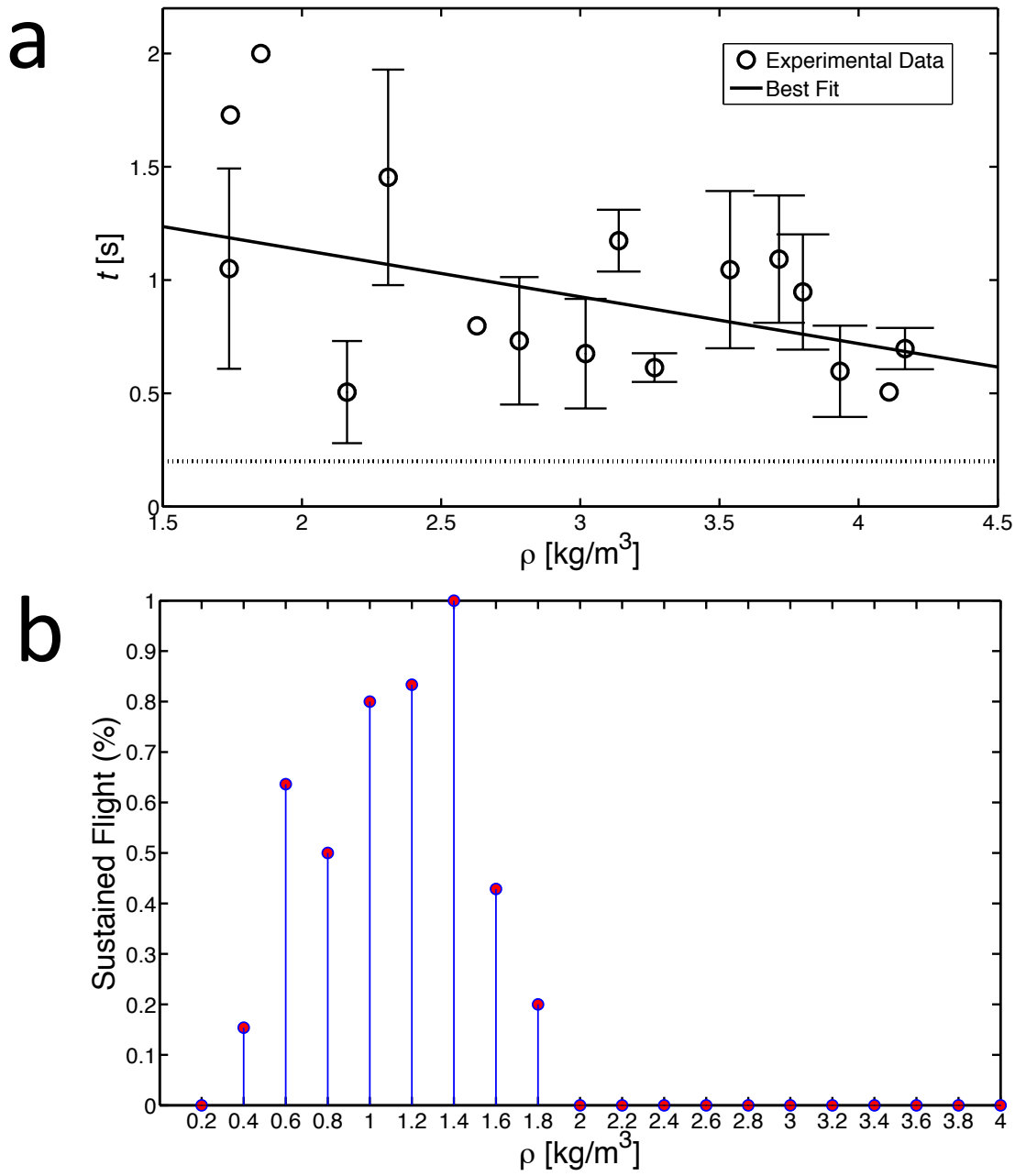

Figure 23: **(a)** Relation between gas density ρ and descent time for mosquitoes suddenly introduced into a container of dense gas. Error bars denote $\pm$ one standard error. Trials were performed once per animal. Points without error bars denote a single trial at the specified gas density. The dotted line a the bottom bounds the minimum time required to fall the container depth at terminal velocity. **(b)** Relation between gas density ρ and percentage of mosquitoes able to sustain flight. Each bar represents N$= 4 - 12$ trials.

At higher gas densities, between 1.6 and 2 kg/m^3, only 50 % mosquitoes can maintain steady flight. At the highest gas densities tested, greater than 2 kg/m^3, no mosquitoes are unable to maintain flight. To investigate further the mechanism for flight failure, we consider in the next section the aerodynamic forces on the mosquitoes' flapping halteres.

5.1.2 Flight failure due to haltere-fluid interaction

In our previous section, we identified the air densities in which mosquitoes can fly. Mosquitoes fail to sustain flight in humidifier fog, with a density up to 2 kg/m^3, and remain grounded until the fog particle concentration falls below 1.7 kg/m^3. We hypothesize this inability to fly is caused by the interaction between the mosquito haltere and ambient fluid.

We measure haltere kinematics and geometry using high speed videography and scanning electron microscopy. Halteres are drumstick-shaped, with a characteristic length of $\ell = 250$ μm and radius, at the widest point, of $R = 60$ μm, as shown in **Fig.21**a,b. They are massive in volume with comparison to fog particles, with diameters $5-35$ μm, a ratio of 100:1. When tethered mosquitoes are stimulated, they flap both wings and halteres for brief periods using a full range of motion. We observe haltere flapping is sinusoidal with similar kinematics for all gas densities tested ($0.2-4.2$ kg/m^3). In normal air, wings and halteres flap at a frequency of $f = 375 \pm 42$ Hz (N = 19), on the same order as the flapping frequency in dense fog ($\rho = 2$ kg/m^3) of $f = 303 \pm 37$ Hz (N = 9) (P-value < 0.0001). The 20% decrease in flapping frequency corresponding to a 67% increase in medium density maintains almost constant mean form drag for the wings. Drag force $F_{\mathrm{D}} \sim \rho$ and $F_{\mathrm{D}} \sim f^2$.

In the following calculations, we use a characteristic flapping frequency of $f = 300$ Hz. The haltere flapping amplitude is $A = 97 \pm 2^\circ$ (N = 6). The time-dependent, linear velocity of a haltere in simple harmonic motion can be written $V(t) = A\ell\omega\cos(\omega t)$, where $\omega = 2\pi f$. The peak velocity of the haltere-tip is therefore $V_{max} \approx 2\pi f A\ell = 0.74$ m/s, using a flapping frequency of $f = 300$ Hz, and flapping amplitude $A = \pi/2$ radians. At densities where flight failure begins, more than 300 fog particles are contained within 1 mm^3 of a

mosquito's flight medium. The flapping halteres will encounter upwards of 2,000 of these particles in 1 second of flight, assuming the shaft's frontal area is negligible compared with that of the bulb.

The total force on the flapping haltere in hovering flight consists of a sum of drag force F_D, virtual mass force F_m, and inertial force F_i,

$$F_{\text{haltere}} = F_{\text{D}} + F_{\text{m}} + F_{\text{i}}, \tag{5.1}$$

where each term may be expressed

$$F_{\text{D}} = \frac{1}{2} C_{\text{D}} \rho \pi R^2 V^2, \tag{5.2}$$

$$F_{\text{m}} = C_{\text{m}} m_{\text{gas}} \frac{\text{d}V}{\text{d}t}, \tag{5.3}$$

$$F_{\text{i}} = m \frac{\text{d}V}{\text{d}t}. \tag{5.4}$$

The haltere mass and radius are m and R respectively; m_{gas} is the mass of gas occupying the same volume as a haltere if modeled as spherical, and V is the time-dependent velocity. Dimensionless coefficients include $C_{\text{D}} = 5.1$, the drag coefficient for a sphere, $C_{\text{m}} = 0.5$, the virtual mass coefficient for a sphere[167]. Though C_{m} is function of jerk, we assume a constant C_{m} is a good approximation in our case. The corresponding Reynolds number Re$= 2R\rho V_{\text{max}}/\mu = 8$, for a medium density of 1.7 kg/m^3, and dynamic viscosity of air $\mu = 1.98 \times 10^{-5}$ kg/m-s. We consider the effect of altered flight conditions on each of the components of Eq. (5.1) in turn.

For flight medium density $\rho = 2.0$ kg/m^3 about 67 % greater than that of air ($\rho_{\text{air}} =$ 1.2 kg/m^3), the anomalous peak drag force is $\Delta F_{\text{D}} = \frac{1}{2}(\rho - \rho_{air}) C_{\text{D}} \pi R^2 (A\ell 2\pi f)^2 = 12.4$ nN. The maximum additional virtual mass force on a flapping haltere can be similarly approximated by $\Delta F_{\text{m}} = (\rho - \rho_{air}) C_{\text{m}} \frac{4}{3} \pi R^3 A\ell (2\pi f)^2 = 0.5$ nN. By adding the drag and virtual mass force, which find their peaks at different positions in the stroke, we calculate their sum $\Delta F_{\text{D}} + \Delta F_{\text{m}} = 12.4$ nN. This value is 0.06% the weight of a mosquito, and nearly equal to the haltere weight, estimated by volume to be 900 ng using the density of water[168].

Based on our observations of flight failure, we hypothesize the calculated anomalous aerodynamic force of 12.4 nN in the high density medium is sufficient to incapacitate the haltere's function. In terms of haltere anatomy, such aerodynamic forces translate to increased strain detected by the campaniform sensilla embedded at the haltere shaft's base. Strain in a cantilever beam $\varepsilon \sim P$, were P is a point force at the tip. Therefore, the increased drag force corresponds to a 67% increase in strain registered at the base. In this case, the finely tuned haltere becomes slightly out-of-sync with the wing's steering muscles, which in turn creates the rapid pitching and rolling behaviors observed in flight.

5.1.3 Flight failure due to artificially increasing haltere mass

To test our hypothesis that an aerodynamic forces of 12.4 nN incapacitates halteres, we perform experiments with mass added to both halteres. Mass added to halteres increases the haltere inertial force F_i, which according to Eq. (5.1), increases the haltere's force in a similar fashion to their immersion in fog. Though increased drag and mass addition have very different dynamical effects, they both increase the strain registered by the campaniform sensilla embedded in the haltere shaft.

We begin by adding a large mass of glue ($50-150$ ng) to one haltere of a mosquito (N= 5). If weight is added to only one of the halteres, a mosquito can remain aloft. Presumably, it ignores the sensory feedback weighted haltere and maintains flight.

By weighting both halteres for each of 5 mosquitoes with a similar mass of glue, we observe they cannot fly. By drastically reducing the volume of glue, we find the minimum amount added to halteres which will induce complications to flight is $\sim 9.8 \pm 8.9$ ng (N=4), which is at the cusp of complete loss of flight ability. At such low amounts of glue (< 5 ng), a mosquito may still be able to remain aloft in our container, but must use the walls of its container as a guide for ascent.

Specifically, the mosquitoes perform pitching and rolling as they would in a denser-than-air gas or if both halteres had been ablated. The third column in **Fig.22** depicts a

mosquito flying in normal air with glue on its halteres. The glue is shaded in blue in **Fig.24**. As seen in **Fig.22**c, a mosquito with glued halteres also falls quickly.

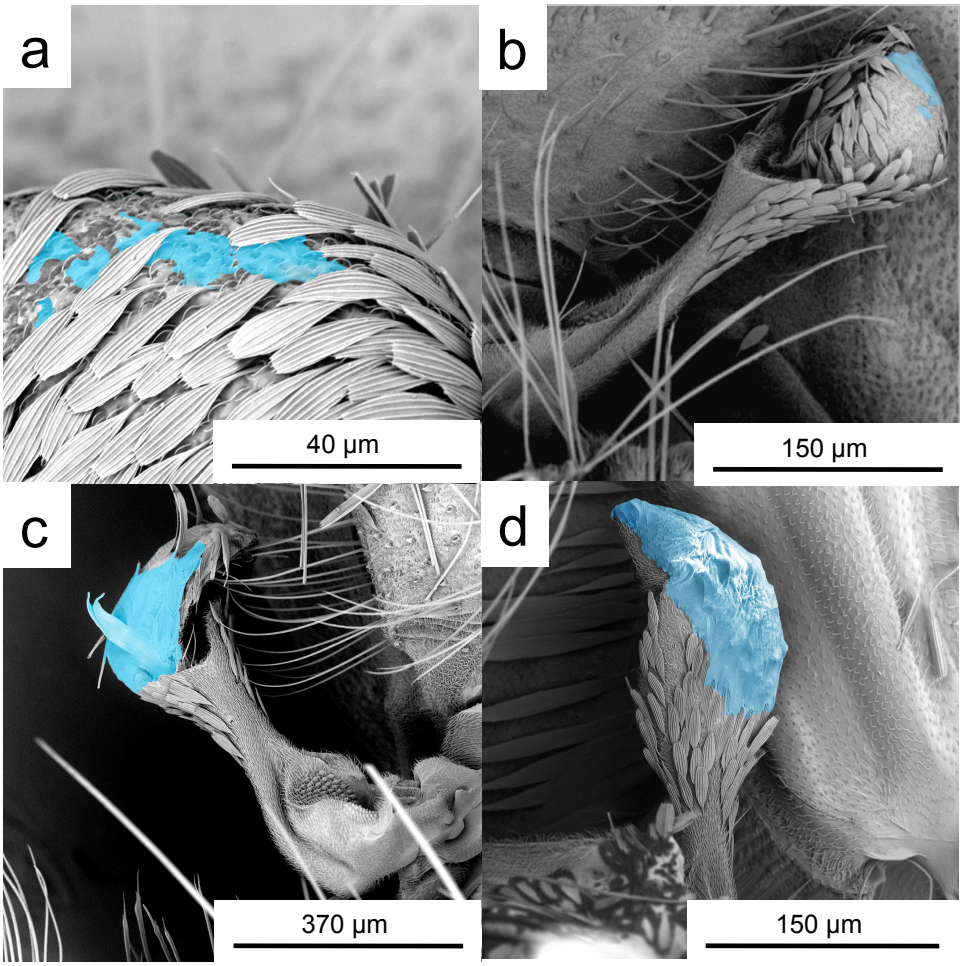

Figure 24: SEM photographs of halteres with various amount of glue, shaded in blue. The glue has a mass **(a)** < 1 ng, **(b)** 2 ng, **(c)** 13 ng, and **(d)** 20 ng.

The additional inertial force added to the halteres by glue is $\Delta F_{\mathrm{i}} = m_{\mathrm{glue}} A \ell (2\pi f)^2$. The mass of the glue m_{glue} is calculated based on volume estimated from images. For glue of mass $m_{\mathrm{glue}} = 9.8$ ng, the maximum additional inertial force is $\Delta F_{\mathrm{i}} = 13.6$ nN, which is similar to the haltere's aerodynamic force in fog, calculated in §3.2. The similarity of these two values suggest that indeed the aerodynamic force of fog is responsible for flight failure.

Both the introduction of heavy gas and the treatment using glue each provide the halteres an additional resistance force. We thus pinpoint the cause of flight failure of a mosquito in fog to malfunctioning of the haltere system, and not the wings. In normal

air, halteres are capable of following the wings, even if wingbeat frequency changes significantly due to wing augmentation[66]. We speculate this anomalous forces places an additional strain on the halteres during flapping. Consequently, the mosquitoes lose the ability to successfully engage steering muscles, causing them to unintentionally turn upside down. A more detailed mechanism involving the pathways from halteres to muscles in unclear. While we do not have a definitive mechanism for flight failure in hyperdense mediums, we can pinpoint the failure as a collapse in haltere function. Next, we show how the additional mass of glue can change the free vibration parameters of the halteres.

5.1.4 Haltere mass affects their natural frequency

All vibratory systems, physical or biological, have a natural frequency due to the geometry and elasticity of their components. Halteres are likely flapped at, or close to, their natural frequency or one of their resonance modes, to reduce the power required to reach maximum amplitude. Wings and halteres are meant to flap together, but if the vibration properties due to aerodynamic drag of haltere mass, a subtle mismatch in phase may occur between wings and halteres. In this section, we examine how increased mass to the haltere affects its natural frequency.

We pluck the halteres of 10 freshly dead mosquitoes, and allow them to vibrate freely (**Fig.25**a, Video S6). As seen in **Fig.25**b, the heavier amounts of glue ($40-50$ ng) decrease the damped natural frequency ω_{d} by 14% as one might expect when increasing a cantilever's inertia. Small amounts of glue ($5-15$ ng) increase ω_{d} by 15% relative to an unaltered haltere. The cause for this increase in frequency is unknown. We find the above differences for ω_{d} to be statistically significant, rendering P-values of 0.02 when compared to the unaltered haltere sample.

We model the haltere as a damped single-degree-of-freedom system, under free vibration. Such a system is governed by $I\ddot{\theta}+c_{\mathrm{v}}\dot{\theta}+k\theta=0$, where $\theta=\theta(t)$, $I\approx m\ell^2$ is the moment of inertia, c_{v} is the damping coefficient, and k is the haltere's spring constant[169].

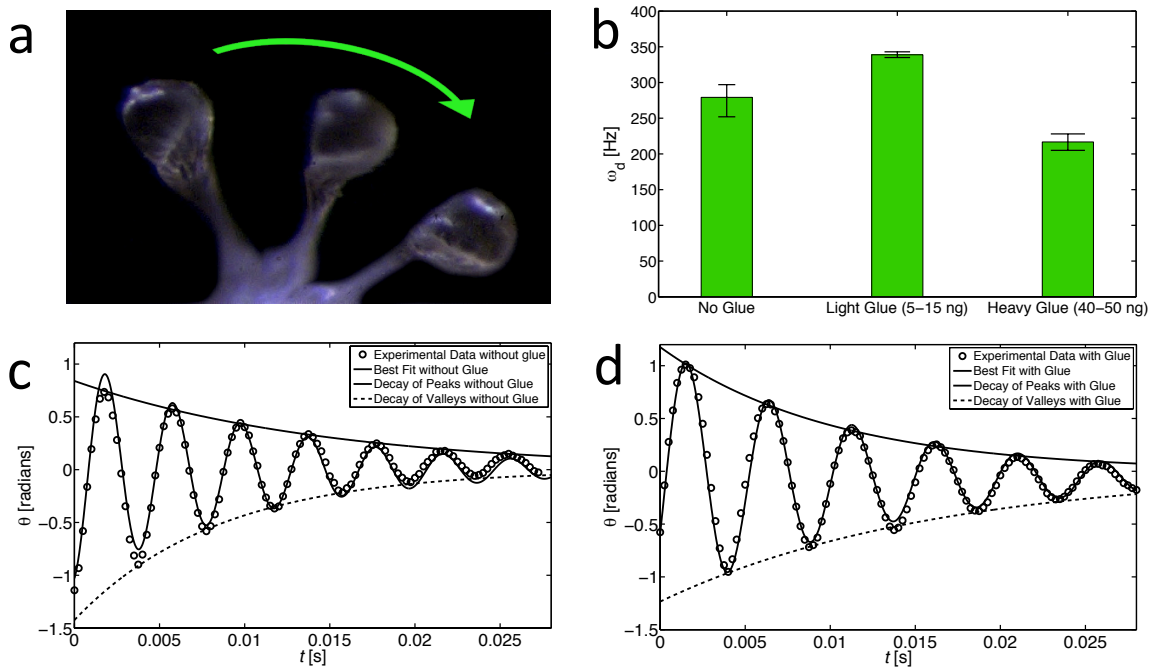

Figure 25: **(a)** Haltere swinging through its plane of motion after manual plucking. **(b)** Damped natural frequencies of freely vibrating halteres with various amount of glue added (N = 8). The bars on each column bound the minimum and maximum values for frequency. **(c)** Time course of freely vibrating haltere, and **(d)** with approximately 50 ng of glue deposited on the tip.

As seen in **Fig.4**c,d, the deflected and released haltere will complete many cycles before coming to rest, and is therefore an underdamped single-degree-of-freedom system. Solving for $\theta(t)$, we may write governing equation above as

$$\theta(t) = \mathrm{e}^{-\zeta\omega_{\mathrm{n}}t}\left(C_1\cos(\omega_{\mathrm{d}}t) + C_2\sin(\omega_{\mathrm{d}}t)\right) + C_3 \tag{5.5}$$

where $\omega_{\mathrm{d}} = \sqrt{1-\zeta^2}\omega_{\mathrm{n}}$ is the damped natural frequency, $\omega_{\mathrm{n}} = \sqrt{k/I}$ is the undamped natural frequency, and C_1, C_2, and C_3 are fitting constants. We have added C_3 to Eq. (8.2) for calibration purposes. On average, addition of glue to a haltere does not alter its damping coefficient ζ. Without glue we calculated $\zeta = 0.05 \pm .02$ (N=4) and with glue added $\zeta = 0.05 \pm .01$ (N=4).

As shown by the examples in **Fig.25**c,d, all of the freely vibrating halteres tested have asymmetrical exponential decay envelopes, likely the result of a single muscle which drives

haltere oscillation[81] alongside a thoracic oscillator[170] when the mosquito is flying. The lower bound of the envelope in **Fig.25**c, (dotted), levels off more quickly than the upper bound (solid), indicating preferential deflection towards the mosquito's anterior surface. The addition of glue to the haltere (**Fig.25**d), not only decreases the vibration of the haltere, but slows the rate by which the vibrations decay. The changes in vibration frequencies and envelopes in plucked halteres resulting from glue addition, suggests a subtle disruption to haltere kinematics in flight. Altered kinematics and mass distribution will impact strain measurements, made by the haltere's campaniform sensilla, and beat rhythm, rendering halteres less effective in regulating wing motion.

5.2 Discussion

Our study highlights the sensitivity and precision of mosquito halteres. We induce flight failure in mosquitoes using two independent means, immersion in hyperdense flight environments and addition of 0.2% mass to the halteres. Our result shows haltere systems are highly tuned to the properties of normal air, rendering small changes to these aerodynamic properties devastating to the insect. A greater understanding of the sensitivity of such sensing systems may lead to a greater understanding of the complex control system of insects and new ways to reduce their populations.

In tests with other insects, we found haltere size is inversely related to their vulnerability in fog. We have observed fruit flies *Drosophila melanogaster* and *Drosophila virilis*, whose halteres are smaller than that of a mosquito, also fail to fly in dense fog. Conversely, houseflies (*Musca domestica*) with larger halteres, can stay aloft in dense fog (Video S7), presumably because their flight system does not require such a finely tuned central pattern generator.

Our results are supported by the findings of Pringle (1948), in which the mechanical resonance of halteres of the *Calliphora erythrocephala* was studied by crushing the haltere bulbs and measuring the resulting change in flapping frequency[81]. Pringle reports a normal

frequency range of $105 - 120$ Hz for females, and $125 - 140$ Hz with crushed bulbs. This result shows aerodynamic forces help govern resonance frequency, and flapping behavior. Our study goes a step further by investigating how a change in drag force affects flight.

Diptera are not alone in possessing very specialized and tuned sensing organs. The male Emperor moth has chemoreceptors which can smell a female 11 km away[171]. A squid's head can detect vibration, and in the $75 - 100$ Hz range, it can sense 0.2 μm peak-to-peak water displacement[116]. Some snakes are able to sense vibrations of their head as small as 0.1 nm peak-to-peak amplitude. Homing pigeons can detect sound frequencies as low as 0.05 Hz, while bats can detect frequencies as high as 100 kHz. In light of the extreme sensitivity in sensing ability in the animal kingdom, disruption of mosquito haltere function with only a 2 ng addition of glue appears more feasible.

When compared to human anatomy, halteres most closely resemble the vestibular structure in our inner ear, used for balance. The inner ear is susceptible to infections, altering the inner ear's original state slightly, causing balance disorders[172]. The vestibular fluid in the semicircular canals of the inner ear pushes against a small membrane, the cupula, as we move our heads. It has been calculated that cupulas have a maximum displacement of 3 microns, or 0.4 % the amplitude displacement of a mosquito haltere[173]. Indeed, microscopic precision in sensing, and the accompanying vulnerability, is a commonality among organisms.

Mosquitoes are not alone in being affected by extreme flight medium conditions. Altering flight medium characteristics reduces the flight performance of most flying creatures. Birds at high altitudes fly with reduced forward drag, but increased requirements for lift production[174]. Orchid bees hovering in heliox (80% He/ 20% O_2), with a density of 0.40 kg/m^3, experienced 50% increases in lift coefficients relative to normal air[129]. The decrease of flight ability in low density and hypoxic environments is a result of both aerodynamics and metabolism. The dynamic viscosity of the flight medium might also create instability flight. It is not possible to calculate the viscosity of our mixtures of R134a and air without

further experiments[175], though based on the viscosities of R134a (12 μPa-s) and air (19 μPa-s), we do not expect the viscosity of the mixture to be dramatically different than that of air. For example, a mixture of nitrogen and R-12 (Freon) with the same volume fraction we use to a create a flight medium density $\rho = 2$ kg/m^3 (74% air, 26 % R134a) has a viscosity of 16 μPa-s. Additionally, a Reynolds on the order of 10 indicates inertial effects dominate viscous effects.

The introduction of gases other than air, displaces oxygen needed for breathing and raises the possibility of hypoxia influencing the results in our experiments. At a density of 2 kg/m^3, the threshold at which no mosquito can fly, the oxygen in our container dropped from 21% by volume to 15% with the introduction of R134a. Such conditions are not prohibitive to flight: insects have been known to survive extreme hypoxic conditions[176] and colonize high altitudes above 6000 m where the oxygen content is a mere 9.5%. We have stated previously that mosquitoes are capable of flying in medium densities of 1.6 kg/m^3. When using carbon dioxide to create this particular density, the oxygen drops to 10.5%, and we notice mosquitoes are able to sustain flight for 10 seconds or more before suffering hypoxic effects and falling to the floor. Mosquitoes left in containers where R134a was used to produce densities greater than $\sim$3 kg/m^3 ($<$ 8% oxygen) would lapse into unconsciousness within 10 s, but no sooner than 4 s. In our observations, insects will cease flapping immediately upon unconsciousness. Since the falling mosquitoes in our experiments continued flapping during descent, we are confident hypoxia did not play a role in our results. Even at the highest gas densities, flight failure behavior occurs within a time much less than 1 s following a mosquito's drop into a container, whereas the total flight time is less than 2 s. The fast onset of flight failure and the flapping of the mosquitoes suggest they are conscious and attempting to fly in our experiments.

Due to the water repellent nature of a mosquito's body, including the halteres, fog particles are unlikely to deposit and remain attached to flapping wings, halteres, and other sensors in quantities significant enough to hinder flight. As seen in **Fig.24** the rapidly

moving appendages have tightly-spaced feather-like sensilla. However, a wetting liquid, such as nontoxic soybean oil (density of 920 kg/m^3), a common insecticide base, may be able to remain adhered. Oil-based insecticides are known to be produced in a range of sizes[177], $2-110$ μm in diameter. A single oil droplet 10 μm in diameter deposited on each haltere would be sufficient to ground a mosquito. Production of insecticide-free fogs may be a viable mosquito-control strategy in some situations. We note that with current foggers, mosquitoes and similarly sized insects will be downed near the output nozzle, not due to immediate insecticide absorption, but due to the fog cloud's density.

To eliminate the likelihood of fog interrupting the function of the mosquitoes' antennae, we cropped the antennae at the base and observed they were able to maintain qualitatively normal flight in a container. Fog exposure on mosquitoes without antennae was met with grounding, in a manner similar to those with intact organs.

Mosquito control using fog produced by ultrasonic humidifiers is not currently viable, especially for large areas. Water and electricity consumption will be unreasonable in most environments, when compared to traditional insecticide sprays. The most realistic use of water droplets to protect humans against mosquitoes would consist of a continuously falling curtain of microscopic droplets over thresholds such as windows and doors. Similar "air doors" are currently used, such that a sheet of high velocity air is directed downward from the top of a doorway. While such curtains of air are effective as an insect filter, they require high power and are noisy. In places where water is plentiful, a "fog door" would provide protection with no sound and lower operating costs.

5.3 Chapter Summary

We perform flight experiments with mosquitoes in mediums of varying fluid density. In gases with densities twice that of standard air, mosquitoes suffer rapid pitching, rolling, and ultimately grounding. We hypothesize the anomalous aerodynamic drag forces, on the order of 10 nN, disrupt the rhythm of mosquito halteres, their gyroscopic sensors and

wingbeat pattern generators. We test this hypothesis by adding weight to the halteres to create inertial forces on the same order of magnitude as aerodynamic forces in heavy air. An increase in the haltere's mass by 10 ng, is sufficient to disable flight. We also show weighted halteres have different natural frequencies than unaltered halteres, and suggest this change in natural frequency prevents synchronization between wings and halteres. This study shows halteres are highly tuned to the properties of air, making changes in air density a potential method to be applied in mosquito control.

CHAPTER VI

DEW-DRIVEN FOLDING OF INSECT WINGS

"The easiest way to get a reputation is to go outside the fold..." -F. Scott Fitzgerald

In this study, we investigate the deformation of mosquito wings due to droplet deposition (**Fig.26**). Our experimental methods for insect handling and imaging are presented in Chapter 2. The 2D bending model we use to predict the response of wings under capillary forces is presented in §1. In §2, we present our measurements of wing bending magnitude for various drop sizes, and qualitatively report the folding behavior of wings in 13 insect species. In §3, we present a discussion of our results and avenues for future work, and §4 a brief conclusion.

6.1 Model

6.1.1 Folding energetics

We model a mosquito wing as a two-dimensional, isotropic beam with length $L = 0.7 - 1$ mm and thickness $t \approx 10$ μm. Consider the wing placed into contact with a circular drop of radius R, as shown in **Fig.27**. Depending on the contact angle θ_e and geometry of the system, the beam can exist in one of two equilibrium states, flat or wrapping the drop. If the process from **Fig.27**a to **Fig.27**b happens spontaneously, the total change in energy can be written as $\Delta E_{\text{total}} = \Delta E_{\text{surface}} + \Delta E_{\text{elastic}} + \Delta E_{\text{gravity}} < 0$, the sum of the changes in surface, elastic, and gravitational energies, respectively. We consider each of these energies in turn.

The change in surface energy from a flat to a wrapped beam is

$$\Delta E_{\text{surface}} = (\sigma_{\text{SL}} - \sigma_{\text{SG}} - \sigma)\, L = -\sigma\,(1 + \cos\theta_e)\, L \sim -\sigma L, \tag{6.1}$$

where σ_{SL} and σ_{SG} are the interfacial tensions between the solid and the liquid, and the

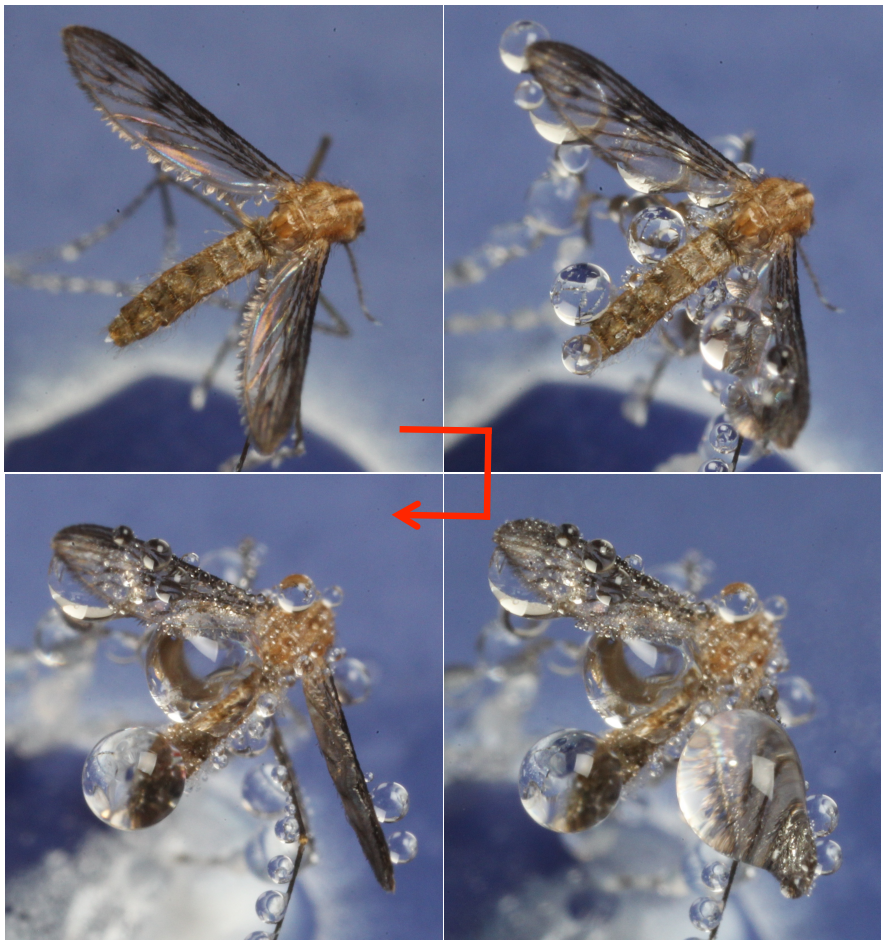

Figure 26: Photo sequence of resting mosquito becoming increasingly wet. Ultimately, the bigger drops on the right wing fall way, leaving a tightly folding wing behind.

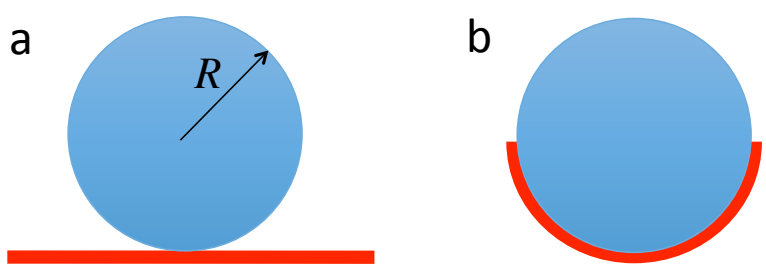

Figure 27: Schematic of liquid cylinder placed in contact with a flexible sheet, where **(a)** pre-wrapping exhibits surface, elastic, and gravitational energies, as compared with **(b)** post-wrapping.

solid and the vapor, respectively. The equilibrium contact angle that the drop makes with a mosquito wing in the Wenzel state is $\theta_e = 90 - 120°$.

The wings used in this study do not have a constant curvature when bent. However, we may define a mean curvature $\bar{\kappa} = \sqrt{\int \kappa^2 \mathrm{d}s/L}$ and mean radius of curvature $\bar{R} = 1/\bar{\kappa}$, where κ is the wing's curvature at any curvilinear coordinate s. The change in elastic energy in the beam[178] is

$$\Delta E_{\text{elastic}} = \frac{EIL\bar{\kappa}^2}{2} \sim \frac{EIL}{\bar{R}^2}. \tag{6.2}$$

The change in gravitational energy as the sheet wraps is

$$\Delta E_{\text{gravity}} = \rho g L t \Delta\bar{H} \approx \rho g L t \bar{R} \tag{6.3}$$

where ρ is the beam's density, g is the acceleration due to gravity, and $\Delta\bar{H} \approx \bar{R}$ is the average change of height in the beam.

Depending on the size of the system and the interfacial tension, the relative magnitudes of the above energies may change. In general, the smaller the system, the less important is gravity and the more important is surface tension. Py *et al.*. have shown the folded length of a structure is governed by the elastocapillary length[97] $L_{\text{EC}} = \sqrt{EI/\sigma}$, where E is Young's modulus, $I = t^3/12$ is the second moment of area of the beam cross-section, per unit depth. For small systems where $L \sim L_{\text{EC}}$, capillary forces are significant[178]. Since elastocapillary length scales as the thickness to the 3/2 power, thinner membranes can produce tighter folds and the thickest membranes cannot fold. Using $E \approx 20$ MPa, estimated from measurement using cicada wings, and $I = 83\ \mu\text{m}^3$, the elastocapillary length for mosquito wings $L_{\text{EC}} =$ 0.15 mm, on the same order as the chord length measured in experiments ($0.7 - 1$ mm). Since L_{EC} is similar in magnitude to L we expect mosquito wings to fold. Using the material and geometric properties of mosquito wings, we find

$$\left|\frac{\Delta E_{\text{elastic}}}{\Delta E_{\text{surface}}}\right| = \left(\frac{L_{\text{EC}}}{\bar{R}}\right)^2 \sim 1, \qquad \left|\frac{\Delta E_{\text{gravity}}}{\Delta E_{\text{surface}}}\right| = \frac{\rho g t \bar{R}}{\sigma} \sim 10^{-3}. \tag{6.4}$$

Therefore, gravity can be reasonably neglected in our analysis in comparison to capillary and elastic forces. In the next section, we perform a more detailed analysis to determine the shape of a wing deformed by capillary forces.

6.1.2 Two-dimensional drop atop an insect wing

In this section, we present a mathematical model for the folding of an insect wing due to growth or evaporation of a single drop emplaced atop it, as shown in **Fig.28**. The influx of fog will cause a drop to grow in volume; the absence of fog will cause a drop to evaporate and shrink in volume. In our two-dimensional model, we consider the cross-sectional area A of the drop as the equivalent measure of drop volume. We consider only drops sufficiently small that gravitational forces remain negligible.

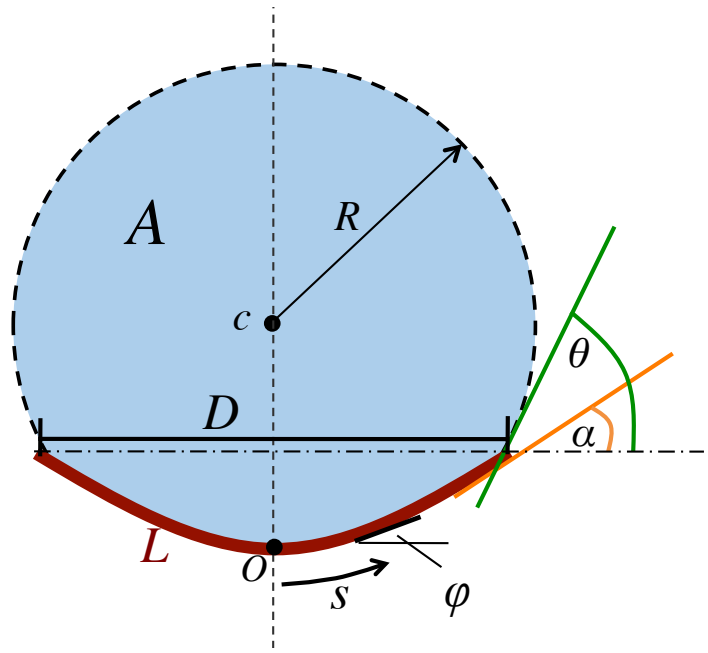

Figure 28: Schematic of drop folding a two-dimensional wing.

To describe the magnitude of folding, we report the tip-to-tip distance D between the leading and trailing edges of the wing. For an undeformed wing, D is simply the wing length L. A worst-case scenario for an insect wing is completely folded in half, in which $D \approx 0$, as seen in **Fig.29**a. The insect wing is considered as an elastica beam of finite bending stiffness EI, but zero thickness and depth into the page.

Fig.28 illustrates a number of dimensions and angles that we will use in our calculations. The drop is shaded, bounded above by its free surface (dashed line), and below by the beam (solid line). In our integration of drop volume, we divide the drop into two parts,

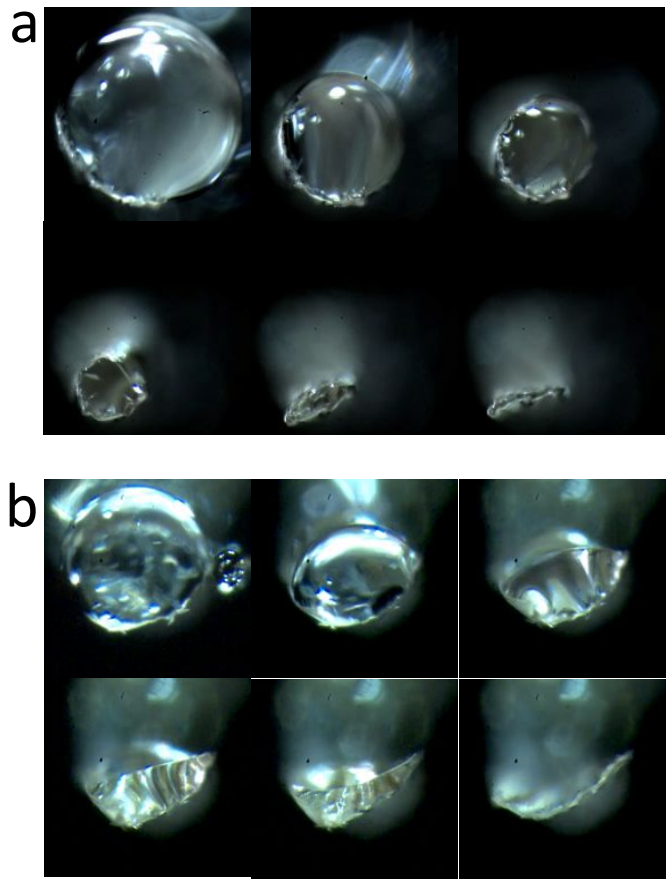

Figure 29: Photo sequence of mosquito wing **(a)** closing and **(b)** opening as the drop evaporates.

above and below the line (dash-dot) connecting the leading and trailing edges of the wing. Above this line, the drop is circular with a radius R and center point C. Below this line, the shape of the drop is governed by its internal pressure and the underlying beam's elastic properties.

In reality, a drop can intersect the beam at any point. In our experiments, we observed the strongest folding occurs for the widest drops, in particular, when the free surface meets the edge of the beam. We consider this case as the boundary condition for our problem. This intersection point involves the joining of three phases, the beam, the water and air. We use two angles to relate the orientation of the beam and the free surface at this point. The angle α is measured between the line tangent to the beam and the horizontal; the angle θ is measured between the line tangent to the free surface and the horizontal. Note that θ is

distinct from the equilibrium contact angle θ_e between the drop and a planar surface. Since the drop intersects the beam at the beam's edge, the free surface can assume any number of angles with the beam.

The rotation angle of the beam φ, relative to the horizontal, is used to describe the deflection as a function of curvilinear coordinate s. Due to symmetry, we consider only half the beam, denoting the lowest point of the beam by $s = 0$, and the rightmost point as $s = L/2$.

By consideration of the geometry of the problem, we may write the tip-to-tip distance D and the drop area A in terms of $\varphi(s)$. Rather than integrating over s, we integrate over $\eta \in [0,1]$, where $L\eta/2$ is substituted for s:

$$\frac{D}{L} = \int_0^1 \cos(\varphi) d\eta \tag{6.5}$$

$$\frac{A}{L^2} = \tilde{R}^2(\pi - \theta + \sin\theta\cos\theta) - \frac{1}{2}\int_0^1 \cos(\varphi(\xi)) \int_1^\xi \sin(\varphi(\eta)) d\eta d\xi, \tag{6.6}$$

where the normalized radius of water drop $\tilde{R} = R/L$.

In light of the discussion of energy in the previous section, we consider only small insect wings in which gravity can be safely neglected. We thus consider only elastic and surface tension forces. The governing equation for local bending is obtained from a force balance, commonly known as Euler-elastica theory. The internal bending moment in the beam $M = EI\kappa$, where $\kappa = \mathrm{d}\varphi/\mathrm{d}s$. By Newton's third law, the load per unit length and unit width P pressing down on the beam is balanced by the beam's elastic force per unit length in the opposite direction, and so $P = \mathrm{d}^2M/\mathrm{d}s^2$. In the curvilinear coordinates shown in **Fig.28**, the beam is subject to Laplace pressure, a uniform load per unit depth such that $P = -\sigma/R$ and is simply supported at the midpoint. The governing equation for bending at a curvilinear coordinate s is therefore

$$EI\frac{\mathrm{d}^3\varphi}{\mathrm{d}s^3} = -\frac{\sigma}{R}, \quad s \in \left[0, \frac{L}{2}\right]. \tag{6.7}$$

The shear force in the beam can be defined as $EId^2\varphi/ds^2$. Shear force in the ends

results from the component of surface tension normal to the wing such that

$$EI\frac{\mathrm{d}^2\varphi}{\mathrm{d}s^2} = -\sigma\sin(\theta-\alpha);\ \text{ at } s=\frac{L}{2}, \tag{6.8}$$

where α is the angle tangential to the beam tip, defined earlier. The beam is unable to sustain a bending moment at its ends, therefore

$$\frac{\mathrm{d}\varphi}{\mathrm{d}s} = 0;\quad \text{at } s=\frac{L}{2}. \tag{6.9}$$

The symmetry of the beam leads to a constraint at its midpoint such that

$$\varphi = 0;\ \text{ at } s=0. \tag{6.10}$$

Triple integrating the governing equation in Eq. (6.7), which is equal to a constant, and solving integration constants with the boundary conditions in Eqs. (6.8) to (6.10), we obtain

$$\varphi = -\frac{1}{6}\frac{\kappa_w}{L_{\mathrm{EC}}^2}s\left[s^2+\lambda\frac{L}{2}s-\left(\frac{3}{4}+\frac{\lambda}{2}\right)L^2\right] \tag{6.11}$$

where $\kappa_w = 1/R$, and λ is an undetermined parameter which satisfies the implicit equation,

$$\lambda = \frac{6\sin(\theta-\alpha)}{\kappa_w L}-3. \tag{6.12}$$

Eq. (6.11) can be normalized, such that

$$\varphi = -\frac{1}{48}\frac{L^3}{L_{\mathrm{EC}}^2}\kappa_w\eta(\eta^2+\lambda\eta-3-2\lambda). \tag{6.13}$$

The result in Eq. (6.13) can now be applied to computationally determine the relation between D and A from Eq. (6.5) and Eq. (6.6). The inputs to the model are L, and L_{EC}. The iteration variable for convergence is λ. To satisfy the condition in Eq. (6.12), a fixed point algorithm is applied because θ and α are both dependent on λ. To accelerate the convergence speed, Steffensen's method[179] is employed such that

$$\begin{aligned}\lambda^* &= f(\lambda^n)\\ \lambda^{**} &= f(\lambda^*)\\ \lambda^{n+1} &= \lambda^n - \frac{(\lambda^*-\lambda^n)^2}{\lambda^{**}-2\lambda^*+\lambda^n}\end{aligned} \tag{6.14}$$

where $f(\lambda) = 6\sin(\theta - \alpha)/\left(\tilde{\kappa}_w \tilde{L}\right) - 3$.

In order to perform our simulation across a wide range of folded shapes, we consider the limits of α and θ. By definition, $\alpha = \varphi|_{\eta=1}$, where $\alpha = 0$ for a flat wing and $\alpha = \pi/2$ for a completely folded wing. However θ changes as the center of the circular drop falls below the line joining the two beam ends. For the case where the center of the circular drop is above this plane, $\theta = \pi - \arcsin(D/2R)$ (**Fig.28**), whereas $\theta = \arcsin(D/2R)$ when the center lies below the plane (**Fig.28**). We must find solutions for A and D for each case separately, and join them to form the theoretical curves.

6.2 Results

6.2.1 Small insect susceptible to wing folding

We begin with a broad survey to identify the size regime of insects susceptible to dew-induced wing folding. Table 2 lists the 13 species used in experiments and their pertinent wing dimensions. Wings are removed from insects ranging in size from a fruit fly, with a single-wing span $S = 1.8$ mm, to a cicada, with wings twenty times longer at $S = 40$ mm. A consumer grade humidifier emulates heavy fog conditions and nocturnal dewfall, producing a stream of $5 - 35$ μm diameter drops, with an average diameter of 15 μm.

We use an elastic modulus $E \approx 20$ MPa to describe the stiffness of insect wings. Due to the mosquito's small size, we measure the elastic modulus of cicada wings to determine a suitable value for analysis. The elastic modulus is measured by taking a chord-wise section of each wing and using an analytical balance to measure the force required to slightly deform each wing. A video camera is used to measure the wing's deflection. Cicada wings have a modulus 25 ± 5 MPa.

Fig.30 shows the relation between wing chord length L and thickness t. The wings denoted by filled symbols fold tightly after drop removal, as seen in **Fig.30**c. Using the solid line, we denote a region in **Fig.30**d where we predict wing folding may be seen in nature. The elastocapillary length L_{EC} governs the limit for which wings can fold[97], and

Table 2: Species used in folding experiments.

species	N	thickness *t* [μm]	chord *L* [mm]	Can fold? [Y/N]
fruit fly (Drosophila melanogaster)	2	5	0.7	Y
mosquito (Anopheles freeborni)	2	8	1.0	Y
fruit fly (Drosophila virilis)	2	5	1.3	Y
lacewings (Chrysoperla carnea)	2	3	1.4	Y
honey bee (Apis mellifera)	2	50	2.3	N
reticulated netwinged beetle (Calopteron reticulatum)	1	25	2.5	Y
northern petrophora (Petrophora subaequaria)	2	60	3.4	Y
firefly (Photuris lucicrescens)	2	30	4.5	Y
forage looper moth (Caenurgina erechtea)	2	50	6.6	Y
bumblebee (Bombus bimaculatus)	2	75	7.1	N
cockroach (Periplaneta americana)	1	95	7.2	N
stone fly (Plecoptera perlidea)	2	20	9.1	Y
cicada (Tibicen davisi)	1	90	14.1	N

is it known that L_{EC} is proportional to L for structures that can fold. Assuming each wing has the same Young's modulus, we use $L = 3.7L_{\mathrm{EC}}$ to divide **Fig.30**d into folding and non-folding regions. The slope of 3.7 cannot be found theoretically, and so is chosen to fit the experiments.

The division is quite good, with all of the non-folding insects below this line, and only one insect, the northern petrophora in the incorrect regime. The distance from an insect's measurements to the closest point on the solid line indicates the level of danger to folding. Six of the thirteen insects studied, fall very close to the the line, indicating that they are near the limits of thickness or chord length at which folding occurs. The insects most in danger of folding is the stone fly, as it is well within the folding regime. The cockroach is the least in danger of wing folding.

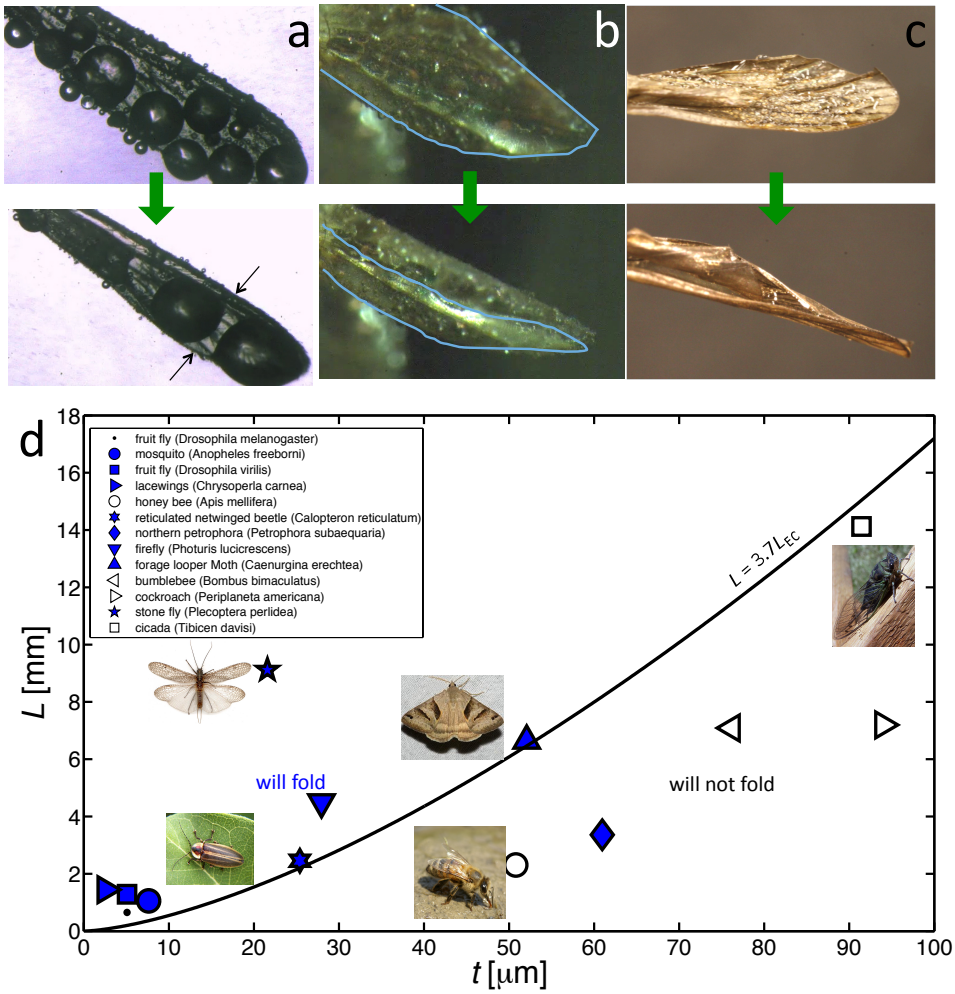

Figure 30: Folding of wings belonging to a **(a)** mosquito, **(b)** fruit fly, and **(c)** stonefly. **(d)** Relation between wing thickness and chord length for 13 insect species. Filled points denote the wings which fold upon droplet deposition and removal in experiments. The curves in (b) trace wing edges.

6.2.2 Taco and edge-type folds

Fig.31 shows how micro-droplet deposition dramatically alters the wing's wetting behavior. If the wing is dry, a drop sits atop it wetting in the Cassie-Baxter state (**Fig.31**a). After 3 seconds or less of exposure to our stream of fog particles, small droplets scattered throughout the wing wet the wing in the Wenzel state (**Fig.31**b). These small droplets serve two functions for further water addition. First, they act as deposition sites and grow upon additional exposure to dewfall or fog particles. Second, they allow larger drops to stick to the wing in the Wenzel state (**Fig.31**c). This Wenzel state has an associated equilibrium

contact angle θ_e across a large range, $30 - 130^\circ$, over the species considered.

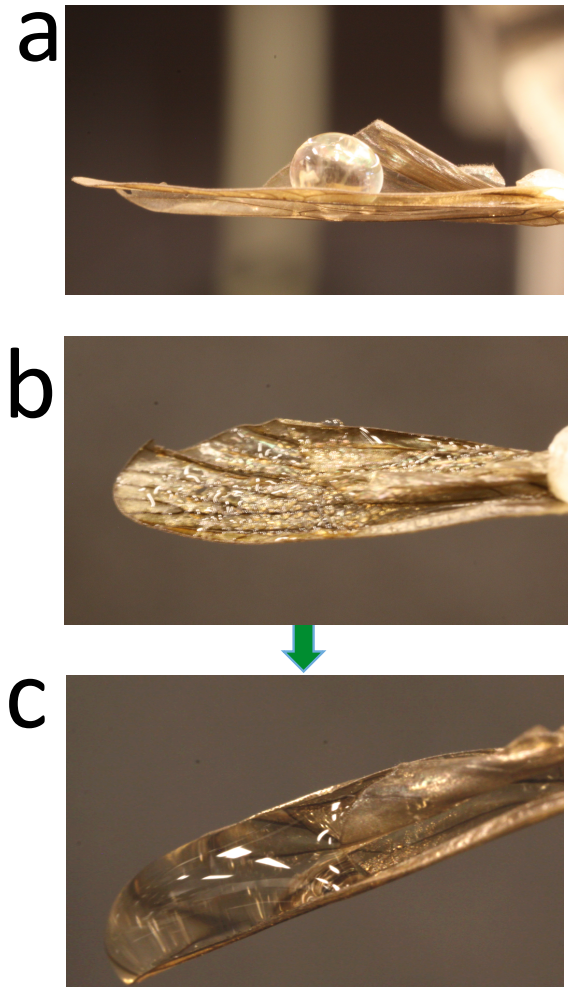

Figure 31: **(a)** Drops deposited on stone fly wing before the introduction of micro-droplets has a very high contact angle $\sim 150^\circ$. **(b)** Micro-droplets wet a stone fly wing upon contact. **(c)** A large drop introduced to wing coated with micro-droplets has a much lower contact angle $\sim 50^\circ$.

Folding occurs as drops coalesce across the span of the wing. This coalescence creates a larger mother drop with a larger contact area, generating sufficient torque to fold the wing. Smaller insects such as mosquito, fruit fly, and stone fly possess wings that fold the tightest. These wings form tacos as shown in **Fig.30**a-c, folding along the centerline of the span (**Fig.32**a). The smallest wings, are typically thinner (**Fig.30**d): this flexibility decreases the elastocapillary length, facilitating folding. Large insects such as cicadas, bumblebees, and cockroaches have stiff large wings that do not bend dramatically and so

cannot fold as tightly as small insects. However, the edges of the wing has few veins, and can undergo folding as shown in **Fig.32**b.

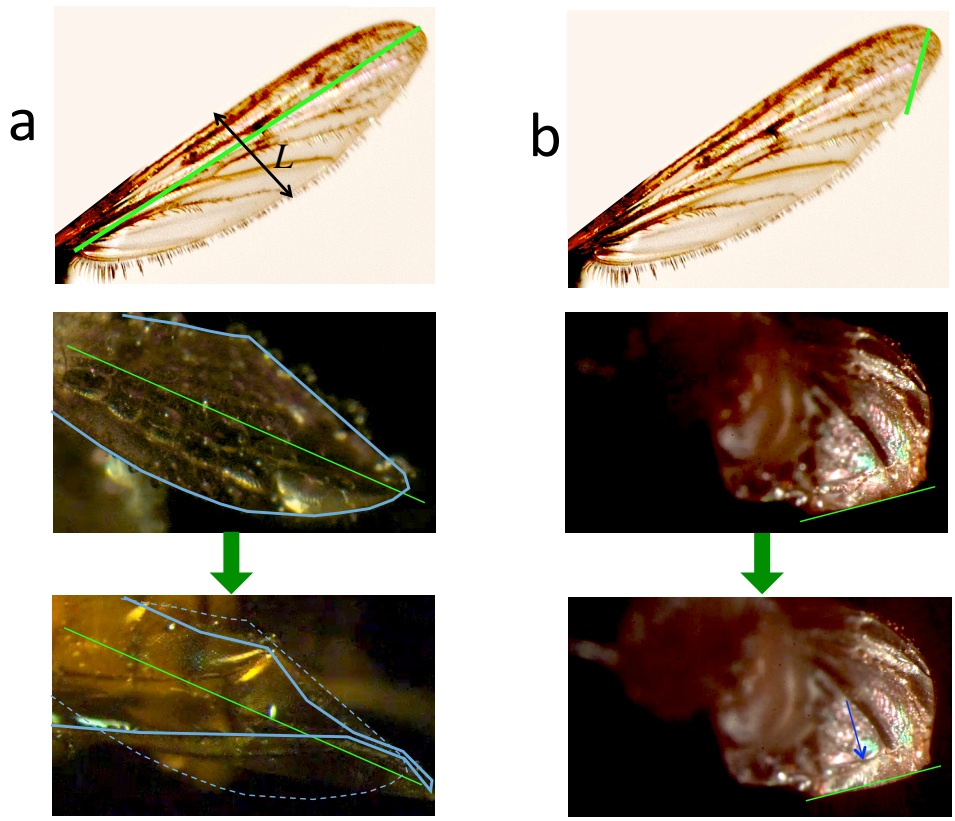

Figure 32: Diagrams of spanwise and edgewise folding followed by photo sequence of a **(a)** fruit fly (*Drosophila biarmipes*) wing folding span wise, and **(b)** a housefly (*Musca domestica*) wing folding at the edge. The green lines denote folding lines, and the blue arrow points on the wing's edge which has been folded over. The curves in (a) trace wing edges.

Wings may also fold through the influence of sliding drops. A large drop may drip off the wing, sliding down the span, and off the wing tip, leaving a very tight fold in its wake (**Fig.30**c). An external disturbance will also cause large drops to fall from the wing in a similar fashion. The insect is unable to contend with these tight folds, which are held together by both capillary forces and viscous lubrication forces resisting separation of the wings. Consequently, such wings are made heavy, small and ineffectual, grounding the insects until the fog ceases and the entrapped fluid evaporates.

6.2.3 Control of wing folding through drop growth and evaporation.

In general the folding of an insect wing is difficult to control. Drops grow and coalesce seemingly randomly across the wing surface. In this section, we use fog to control the growth of drops on the wing, and then hot lights coupled with cessation of fog to control the shrinkage of these drops. In parallel, we measure drop area A and wing edge distance D under a microscope. **Fig.29**a shows a photo sequence of a wing closing as the water drop evaporates. Experiments, which take $7-10$ minutes, are performed on ablated mosquito wings, where the wing is cut near its tip, as shown in the inset of **Fig.33**a, in order to facilitate measuring D from side views of the wing. Through this process, we obtain controlled folding of the insect wing which we compare to our theoretical predictions.

Fig.33a shows the relation between the dimensionless wing distance D/L and the dimensionless area of the drop A/L^2 for three mosquito wings. Each open symbol represents a different wing, and trends are quite consistent between the three wings tested. **Fig.29**a shows a large drop decreasing in volume. As the drop evaporates, decreasing in A, the wing closes more tightly, decreasing in D. When the wing folds very tightly ($D/L < 0.4$), the drop volume has become so small that the meniscus falls below the line drawn between wing edges (dash-dot line in **Fig.28**). Below the smallest drop area measurable of 0.1, the wing abruptly shuts completely, wherein $D = 0$. Conversely, as the drop increases in volume, the wing unfolds, nearly reaching the flat wing distance of $D = L$.

In **Fig.33**a, the solid lines indicate our theoretical predictions for the relation between D/L and A/L^2 using theory derived from Euler's elastica in §3.2. The input to the model is the wing's chord length and thickness, as well as the interfacial tension of the water. The elastocapillary length is used as a free parameter because we cannot measure the bending stiffness $B = EI$ of the wing directly, due to the wing's small size. The color of each line represents a different value of the elastocapillary length L_{EC}, as shown in the legend.

The theoretical trends vary qualitatively depending on the thickness of the wing. The blue and green curves, corresponding to the physically plausible $L_{\mathrm{EC}} = 125-200\ \mu$m, fit

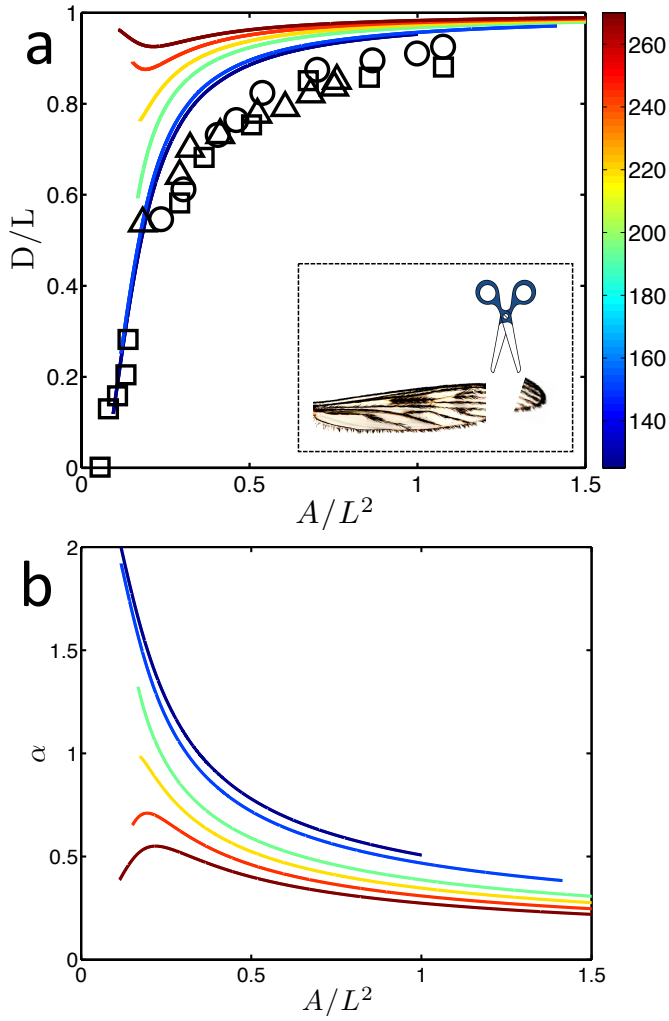

Figure 33: **(a)** Experimental points and theoretical curves of wingtip extent D/L in relation to drop area A/L^2. **(c)** Theoretical curves of wingtip angle α in relation to drop area A/L^2.

our data well. Small drops fit the theory best. As drops increase in size, our experiments generally give a 10 percent higher degree of folding than predicted. We find a value of $L_{\mathrm{EC}} = 125\ \mu$m and so $B = 1.2 \times 10^{-7}$ N-m^2 best fits our data. With a wing thickness of 10 μm, the corresponding Young's modulus is 19 MPa, which is also close to our measurements for a different insect, the cicada. These values of stiffness is consistent with values measured by previous investigators: Shang *et al.*. (2009) suggests that stiffness $B < 10^{-8}$ N-m^2 for wings with $L < 1$ mm. Lower values of B prevent our model from converging and cannot be plotted using our current methods.

For stiffer wings, the brown and red lines, for which $L_{\mathrm{EC}} > 240\ \mu$m, the curves flatten and do not capture the shape of mosquito wings. An anomalous behavior is shown: wings will reopen as the drop evaporates to areas less than $A = 0.2$. This behavior is shown in the anomalously stiff mosquito wing in **Fig.29**b. This opening is distinctly different behavior from the green and blue lines in which the wing closes as the drop evaporates. This evaporation-induced unfolding shows that certain breeds of mosquitoes can resist wing folding, as shown by their closeness to the folding boundary in **Fig.30**.

This transition curve between opening and closing wings is denoted by a yellow line in **Fig.33**b,c, associated with $B^* = 3.5 \times 10^{-7}$ N-m^2 and a wing thickness of 13 μm. This transition is clearly seen in **Fig.33**b, where we plot α in relation to A/L^2. A large alpha corresponds to tight folding. For the stiff wings, the wings begin to unfold, and exhibit smaller α. For MAV wings to be designed for moist environments, they should be stiffened so that their elastocapillary length $L_{\mathrm{EC}} > 220\ \mu$m. Wings in this regime will unfold automatically as water evaporates.

6.3 Discussion

Our study highlights the vulnerability of small insects to wing deformation by dew deposition. We observe very different results depending on wing stiffness. For soft wings, as a drop shrinks by evaporation, the wing wraps the drop, folding the wing more tightly. This behavior is well predicted by our model derived from Euler's-elastica equations. The behavior of stiff wings is quite different and should be emulated by MAV wing designers. The wing is initially bent by drop growth, but can then be opened by further drop growth.

We observed systematic error of 10% in our predictions, likely due to the assumption of isotropy in our model. However, biological wings are laced with irregularly placed veins and hairs which do not always run parallel to one another or the leading edge. This anisotropy affects how the wing unfolds as a the drop evaporates. A higher concentration of veins at the wing's leading edge hinder this edge's mobility during folding. As a drop

held within the wing evaporates, the trailing edge draws toward the static leading edge.

Veins within the wing also allow the wing to fold tighter than might be predicted with an isotropic surfaces. We observe when the wingtips meet, forming a closed surface, the fold's crease straddles a vein. This vein acts as a hinge site enabling the wing to appear folded in half. Consequently, the bended wing does not maintain a smooth curve, but instead forms a "V" shapes for very tight folds.

6.4 Conclusion

Insects are non-wetting, but deposition of micro-droplets is effective at wetting an insect wing. The deposited drops coalesce and grow sufficiently large fold the wings inward via capillary forces. Measurements of folding magnitude were taken using wings ablated from *Anopheles freeborni* mosquitoes, and compared to a two-dimensional elastic model, which predicts well the behavior of folding wings. If wings are sufficiently flexible, evaporating drops create tighter folds that cannot be unfolded except through evaporation over long periods. The tightness of the fold is directly related to the amount of water supported by the wing. This study reveals a previously uncharacterized danger to insects and MAVs in the wild and an unforeseen avenue of insect control.

CHAPTER VII

MOSQUITOES ACTIVELY REMOVE DROPS DEPOSITED BY FOG AND DEW

"Dew-drops are the gems of morning, but the tears of mournful eve!"
-Samuel Taylor Coleridge

We have now investigated the fate of a small insect's wings upon the deposition of fog or dew, but the wings are only one site for deposition, the question remain how a mosquito might cope with the additional mass. In this chapter we investigate the mechanisms of *Anopheles freeborni* mosquitoes to remove deposited moisture from their bodies. Our experimental methods for insect handling and imaging are provided in Chapter 2. §1 gives brief consideration to the acceleration insects should generate to remove droplets from their bodies. In §2, we present our observations and measurements of the various mechanisms mosquitoes use for drop removal. In §3, we present a discussion of our results and avenues for future work.

7.1 Theory

In this section we use theory to predict the magnitude of acceleration required by an insect to remove a drop of particular size. **Fig.34** shows a hemispherical drop of radius R emplaced on an insect wing. The adhesion force of the drop to the wing is $F_s = 2\pi R\sigma \sin\theta \sim R\sigma$, where σ is the surface tension of water, and θ is the equilibrium contact angle. If the wing is abruptly accelerated, the inertial force in the opposite direction is $F_{\text{drop}} = (2/3)\pi\rho R^3 a \sim R^3\rho a$, where ρ is the density of water, and a is the acceleration of the wing. Equating the adhesion and inertial forces yields an expression between the

applied acceleration and the smallest drop that can be removed by this process:

$$a \sim \frac{\sigma}{\rho} R^{-2}. \tag{7.1}$$

As $R \to 0$, $a \to \infty$, and thus smaller drops require greater accelerations to remove. Drops with a radius of 4.7 mm and larger can be removed by gravity. Since such drops are larger than a mosquito, it is rarely observed that drops fall from mosquitoes due to gravity. Therefore, a mosquito must remove drops by applying high accelerations using a variety of techniques that we review in the next section.

Table 3: Methods for droplet removal employed by mosquitoes.

	Particle Diameter *D* (prior to deposition)	**% Body Weight of 2 dyne Mosquito**	**Survival Behavior/ Mechanism**	**Associated Acceleration (*g*)**
Rain	1 – 8 mm	100 – 5000	hyrdophobicity, passive rotation	50 – 300
Fog	0.3 – 10 μm	10^{-10} – 10^{-5}	rest in unfavorable conditions	----
Dew	~100 nm	----	rapid takeoff hard landings wing flutters	0.5 – 3 10 2500

7.2 Results

Insects must cope with a wide range of particles in their environments, including millimetric raindrops, micrometric fog droplets, and nanometric water vapor. The size of these three classes of particles is given in Table 6. **Fig.35**b,c shows fog condensing into discrete drops, covering the insect's body. If we zoom in, as in **Fig.36**, we observe the progression of drop growth between the hairs. Over time, the drops increase in size. The accumulated

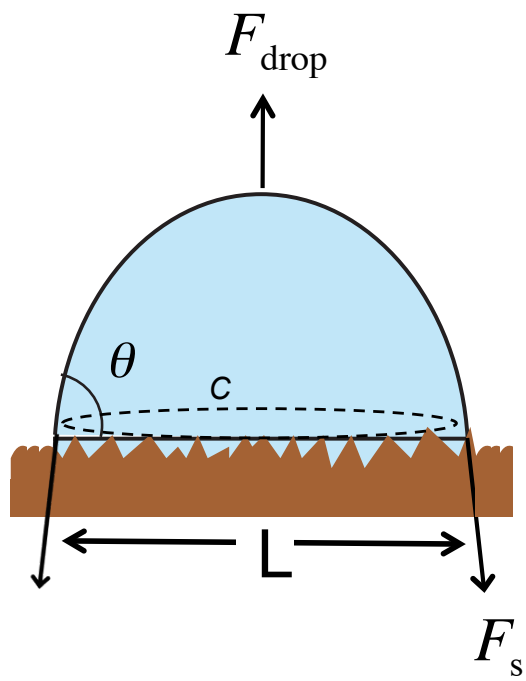

Figure 34: Schematic of drop adhering to an insect's surface.

drops across the mosquito's body can be many times its mass[119]. Below we report three methods, listed in Table 4, which mosquitoes use to remove these drops.

Table 4: Predicted and observed drop sizes for each method in this study.

Mechanisms of Deposition Removal	Associated Acceleration (*g*)	Observed Drop Radius (μm)	Predicted Drop Radius (μm)
rapid takeoff	0.5 – 3	>500	1575 – 3850
hard landings	10	280	860
wing flutters	2500	150	55

7.2.1 Take-off

In previous work[119], we have shown a flying mosquito is grounded rapidly when encountering very dense fog. After the fog has settled, mosquitoes laden with droplets tend to remain at rest. This behavior is likely a strategy to conserve energy. After waiting, on the

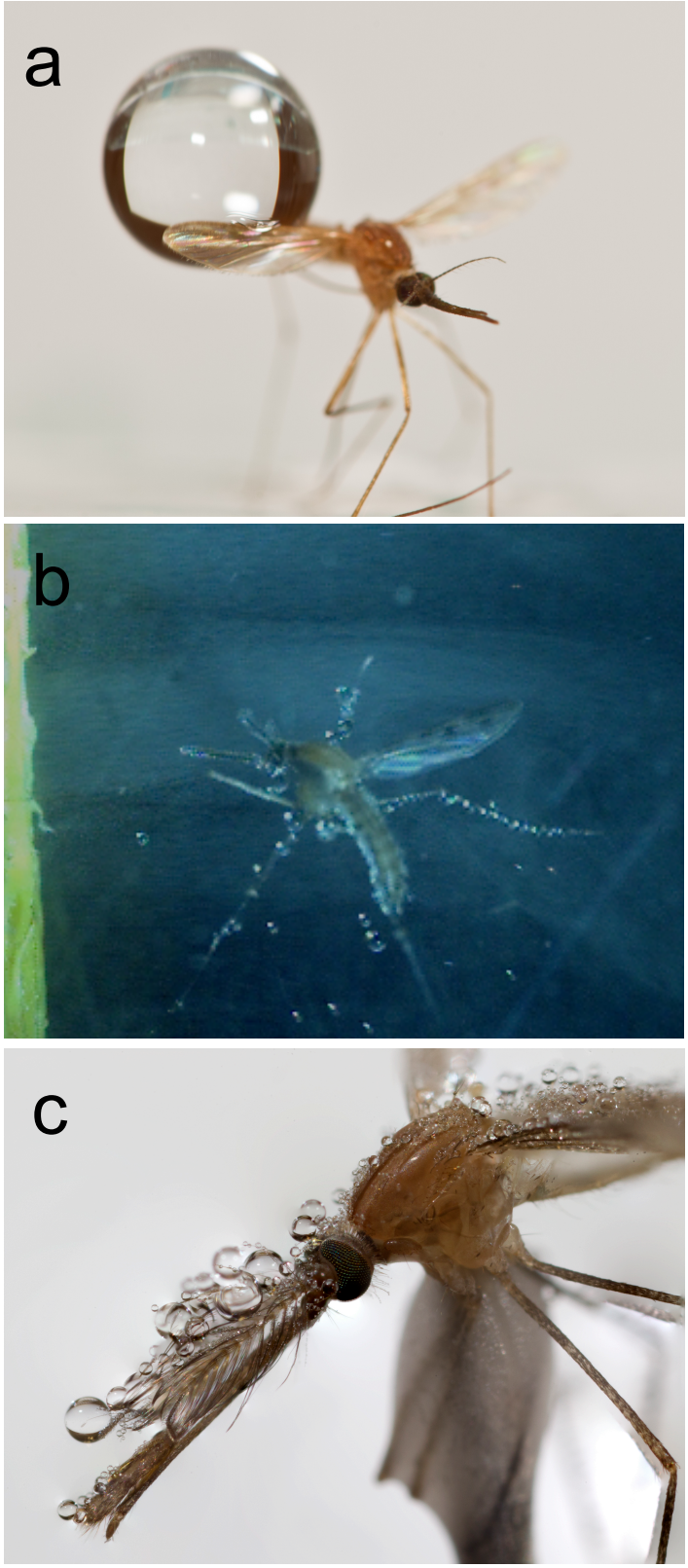

Figure 35: **(a)** Raindrop impacting a flapping mosquito. **(b)** Mosquito attempting flight in a stream of 15 μm fog particles. **(c)** Resting mosquito covered with droplets after the deposition of 15 μm fog particles.

order of one minute, the insect tries to take off. In our experiments, we observe the vigor of takeoff is strongly dependent on the direction off takeoff. We discuss two types of takeoff, those from the floor and a wall, both in which the insect takes off normal to the surface.

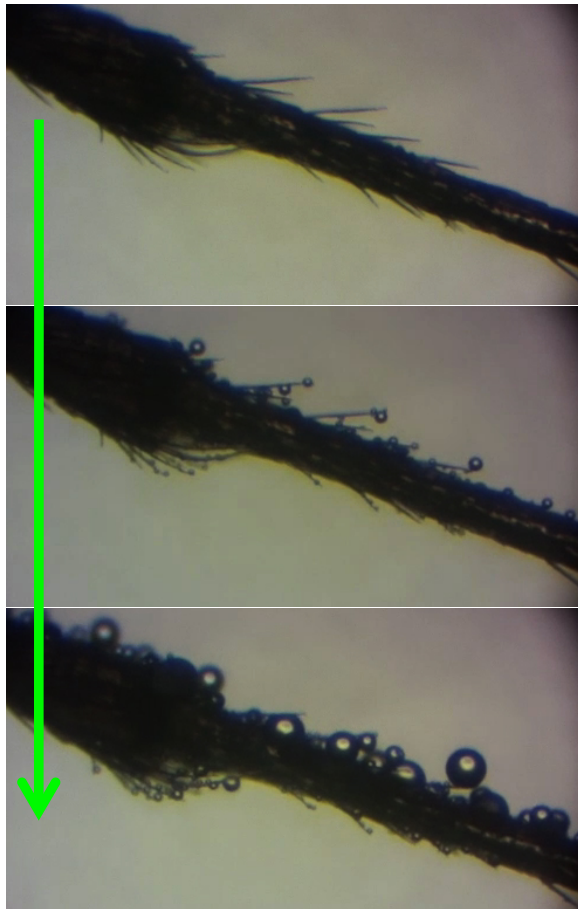

Figure 36: Photo sequence of droplets forming on a mosquito leg through the deposition of 15 μm fog particles.

Mosquitoes take off from the floor with an acceleration of 1.6 ± 1.1 g when dry. When they are wet, they do not take off. In some cases, mosquitoes cannot fly their legs or other body parts are entrapped by accumulated moisture, as seen in **Fig.37**. A leg of diameter $D_{\text{leg}} = 100$ μm would require an applied force of $F = \pi\sigma D_{\text{leg}} = 2.3$ dynes to pull free from a liquid film. If all six legs are entrapped, upwards of six times the mosquito's weight is required to escape the film. We observe mosquitoes flapping in these scenarios, but remaining grounded.

Figure 37: A mosquito attempting to escape a water film upon the ground.

Wet mosquitoes resting on a wall or a ceiling are much more likely to takeoff than those resting on the floor. Wet mosquitoes generate accelerations of 0.47 ± 0.26 g (N = 4), only one sixth the takeoff acceleration of dry mosquitoes (3.1 ± 1.9 g, N = 5). The lower acceleration of wet mosquitoes is explained by their higher mass, roughly a factor of six (6.22 ± 0.22, N = 3). A wall takeoff is more vigorous, and so more effective at removing drops, than from the floor. Takeoffs from a wall involve forces applied perpendicular to gravity, and so necessarily have higher accelerations than takeoffs from the floor. Indeed, takeoffs from walls are higher than those from the floor by 1.5 g, which is close to the

expected value of 1 g.

7.2.2 Hard Landing

A dry mosquito will repeatedly attempt flight when held by any part of its body. Upon release, the mosquito will assume stable flight within one second[119]. Surprisingly, a wet mosquito falls motionless when released from any height (N = 20). They make no attempt to flap during the fall, but resume motion after collision with the floor. **Fig.38**a shows a photo sequence of a wet, motionless mosquito impacting the ground. Before collision, the mosquito carries approximately forty visible drops on its legs, wings, and body. After impact, the number of drops adhered falls by $\sim$75%, with roughly ten drops remaining.

Fig.38b shows the time course of the vertical position of the mosquito's head (open symbols), and a drop with radius of 280 microns near the head (closed symbols). Prior to collision, the mosquito is falling at a terminal velocity of $U = 0.44$ m/s, which is significantly higher than the falling speed $U = 0.135 m/s$ of an anesthetized, dry and much lighter mosquito[119]. During a 3.8 ms collision with the floor, the mosquito's head undergoes an acceleration $a = U/\tau = 115$ m/s^s, or about 10 g, which is well within its limits of survival[117,118], which is greater than 300 g. In fact, after collisions, the insect stands up, shakes off a few additional drops (**Fig.38**c) and flies away. The smallest drops are likely to remain attached through both impact and shaking, but these behaviors are an excellent method for removing collected moisture.

7.2.3 Wingbeating

The most unusual method of drop removal is a modified wingbeat. Shown in **Fig.39**a, this maneuver can be compared to driving a beam, fixed at one end, at its natural frequency, such that the amplitude of deflection at the free end is much greater than that at the fixed end. This *flutter stroke* causes a mosquito's wings to dramatically flex, removing a number of small droplets.

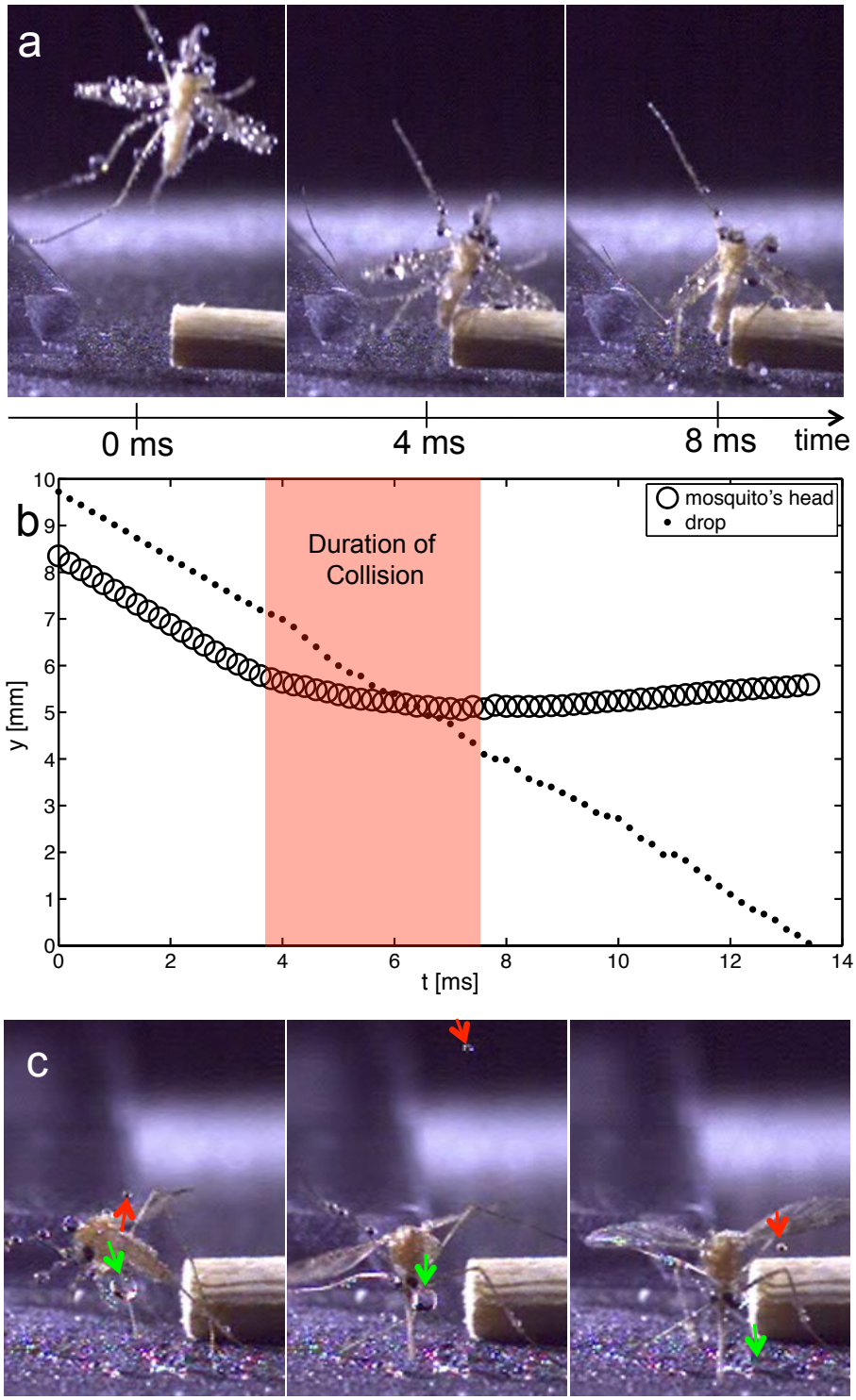

Figure 38: **(a)** Photo sequence of a live mosquito, falling motionless and covered with dew droplets. Drops are dislodged upon impact. **(b)** Time course of the vertical position of a mosquito's head (open symbols) and a 0.8 mm diameter drop (closed symbols), originally attached to the mosquito. **(c)** Photo sequence of a mosquito standing and shaking after a hard fall. Arrows denote the direction of drop travel.

Black lines in **Fig.39**a trace the wing at various moments over the duration of the flap. The time course of the displacement of the wingtip, with respect to its resting state, is plotted in **Fig.39**b, with a spline interpolant through the data. We denote three consecutive regions in **Fig.39**b as the flutter stroke, transition, and normal stroke phase.

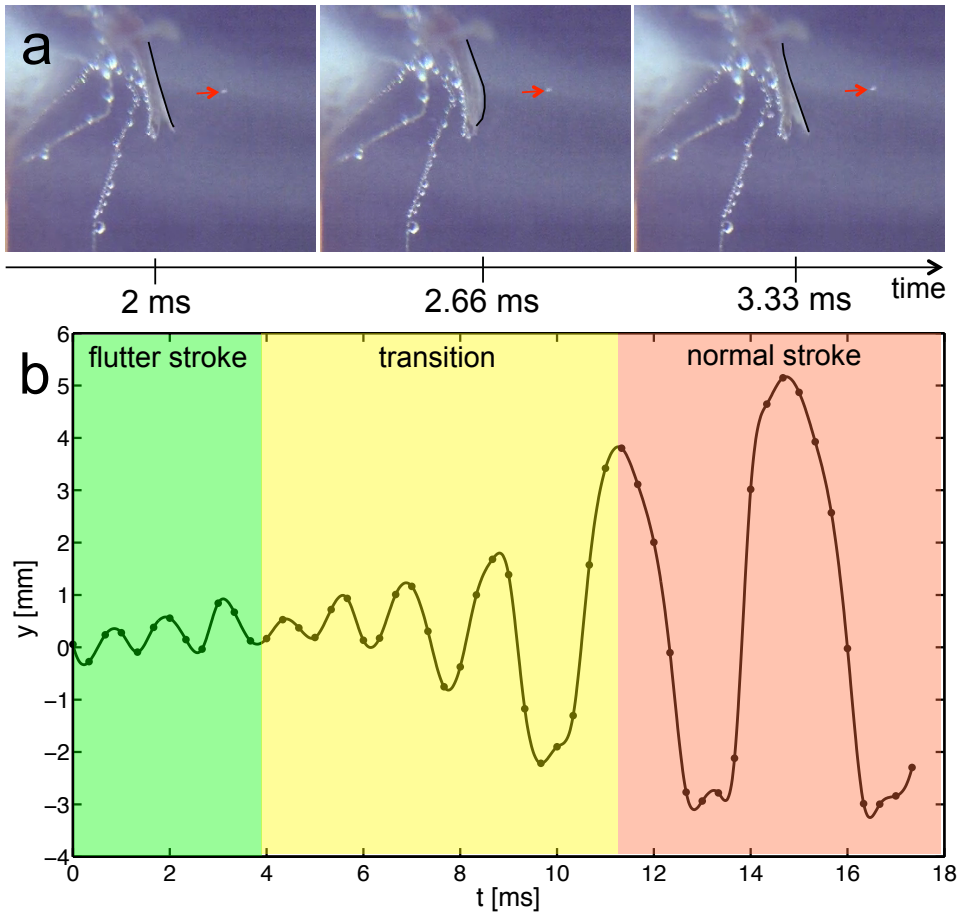

Figure 39: **(a)** Photo sequence of a mosquito removing droplets from wings using a flutter stroke. The drop denoted by the arrow has a radius of approximately 0.15 mm. **(b)** Time course of the vertical position of wingtip measured against the natural resting state, for the mosquito in (a).

During the flutter stroke phase lasting 4 ms, the wings beat at 875 Hz. During the flutter stroke, the wingtip amplitude, at less than 1 mm, is roughly 10% of a normal stroke. The flutter stroke produces higher acceleration on adhered drops than a normal stroke. For an amplitude $A = 0.8$ mm and frequency $f = 875$ Hz, the flutter stroke generates $a_{\max} = A(2\pi f)^2 = 2470\ g$. Thus, this motion is explicitly for removing drops, and not for flight.

In the transition region, the amplitude grows while the wingbeat frequency slows to the normal wingbeat frequency, 285 Hz.

We compare the effectiveness of the three techniques in Table 4. We record the size of drops removed during each, as shown in **Fig.38**b and **Fig.39**a. Using the observed acceleration, we can compare the size of the released drop to that predicted using Eq. (7.1). The wing flutter generates the highest acceleration (2500 g), followed by hard landings and takeoff, which are roughly comparable ($0.5 - 10$ g). Clearly the wing flutter can dispel a wider range of drop sizes than the other two methods. The superiority of the wing flutter is shown by the data, in which the drop dispelled is half the size of the other drops. The last column of the table shows the expected range of sizes for the removed drops, roughly consistent with those observed. In fact, the predicted drop size dispelled by the flutter stroke is about 50 μm size, below the limit that can be seen in our videos.

7.3 Discussion & Future Work

While our study focused on insects, the preceding principles to eject drops can be extended to much larger organisms. Like insects, most mammals are covered with hair, which acts to repel water by an oily coating on the fibers[106]. However, mammals can trap large amounts of water within their fur after swimming, which they need to remove[122]. By rapidly oscillating their bodies, producing up to 180 degrees of skin displacement, mammals generate centrifugal forces sufficient to remove 70% of the water trapped in their fur within seconds. Humming birds have been observed to exhibit similar behavior in flight[18]. The animals' loose skin and feathers is crucial to their ability to generate large shaking amplitudes and high forces.

While insects do not have the advantage of loose skin[122] or feathers[18] to aid in water removal, they have exists a rich set of strategies for water removal across the gambit of insect species. Mosquitoes employ a number of active strategies such as the flutter stroke, and passive strategies, such as hard falls. Other strategies may be species specific, or subtler

than those we observe. Future work should be done to compare and contrast the various grooming and drying techniques in insects. The techniques will vary by insect geometry, locomotive style, and climate.

Micro-aerial vehicles (MAVs)[1–7] can employ the techniques reported here to remove water, particularly hard landings. For a perched MAV, a terminal velocity fall should be less than 1 m/s and easily survivable by on-board components. For larger fliers, such as birds, crash-landing is not an option for water removal due to their higher mass and so a higher terminal velocity. Furthermore, birds have been known to shake water from their bodies[18]. Additionally, a drenching is not as life threatening as flyers grow in size because of an increasing volume to surface area ratio. Nevertheless, birds can generate large accelerations on take-off sufficient to remove drops. The European migratory quail[180], *Coturnix coturnix*, uses its wings and hind-limbs to produce 8 g, enough to dispel medium to large-sized drops.

This study also raises questions of wetting, namely, whether or not insect hair arrays are optimized to repel water. While micro-pillar wetting models exist[49], future researchers may choose to search for an optimum hair spacing, diameter, length, and stiffness, such that the array easily repels water drops at any length-scale.

7.4 Chapter Summary

In this chapter, we have looked briefly into three mechanisms by which mosquitoes remove water from their bodies, takeoff acceleration, collision with the ground, and a modified wingbeat. The gamut of techniques create accelerations ranging from $1-2500$ g. The modified wingbeat, in particular is most able to remove the smallest droplets, as mosquitoes are able to flap their wings at more than twice their wingbeat frequency in flight.

CHAPTER VIII

WET MAMMALS SHAKE AT TUNED FREQUENCIES TO DRY

"A dog is the only thing on earth that loves you more than he loves himself." - Josh Billings

In this study, we investigate a mechanism used by mammals to dry quickly, the wet-dog shake shown in **Fig.40**a. In Chapter 2, we describe the novel methods developed in this study, including a robotic wet-dog-shake simulator. We proceed §8.1 by measuring the masses and frequencies of shakes spanning a wide range of mammals. Next, we characterize the kinematics of the shaking response using high-speed video and fur-tracking. We proceed by presenting models for both drop ejection and the ensuing dryness of the animal, testing these models using experiments with a spinning tuft of fur. Lastly, we discuss the implications of our work in §8.2 and suggest directions for future research. A summary of this work is given in §8.3.

8.1 Experimental Results

8.1.1 Shaking frequencies across mammals

Using high-speed video at 500-1000 fps, we filmed the shakes of 33 wet mammals, spanning 16 species and 5 breeds of dogs (**Fig.41**). Animals were provided by the Atlanta Zoo, the local park, and neighboring laboratories at our institution, and filmed according to IACUC protocols A09036 and A10066. Shakes were prompted by sprinkling small animals with a spray bottle, and large animals with a hose. We found animals generally shook after the flow of water had ceased.

We characterized animal sizes using measurements of body mass M and the chest circumference $2\pi R$ measured posterior to the shoulder, where R is cross-sectional radius of the chest. In general, one specimen per species or breed was available. Several specimens

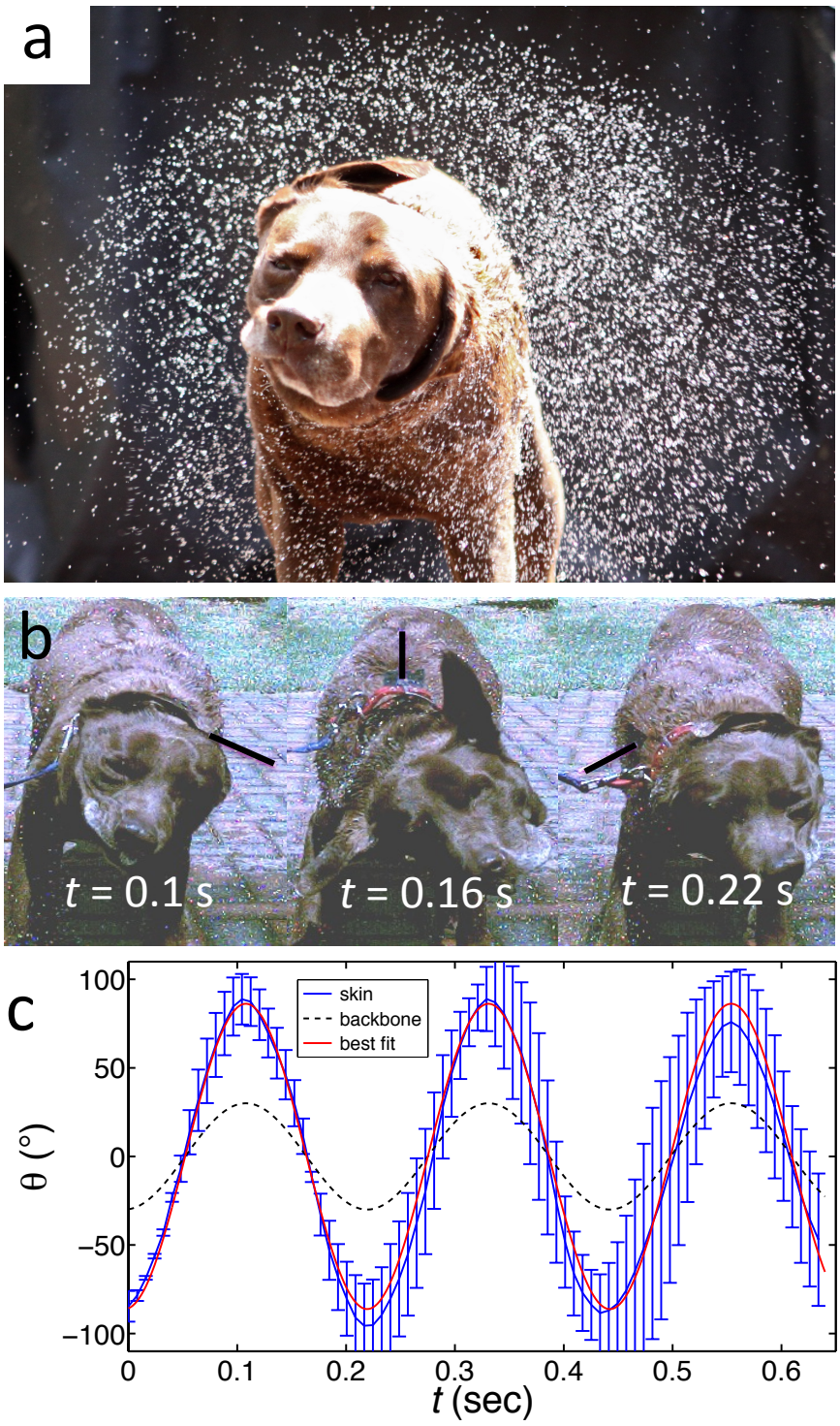

Figure 40: Kinematics of fur during the wet-dog shake. **(a)** A droplet cloud generated by a Labrador retriever during mid-shake. **(b)** Time-lapse images of a dog shaking its fur. The thin black line highlights a marker glued between the shoulders of the dog's back. **(c)** Time course of the angular position of the skin and vertebrae of the dog. Error bars indicate the standard deviation of measurement (N=3).

of mice and rats provided the opportunity to determine variability in frequency and mass within a species. The averages and standard deviations of measurements are presented in Table 5 with corresponding error bars in **Fig.42**. Among four juvenile mice, four adult mice, and four adult rats, the standard deviations for both mass and frequency were only 5-10% of their respective averages, indicating that there is very low variability in these measurements. This also suggests that each animal has a particular frequency at which it shakes.

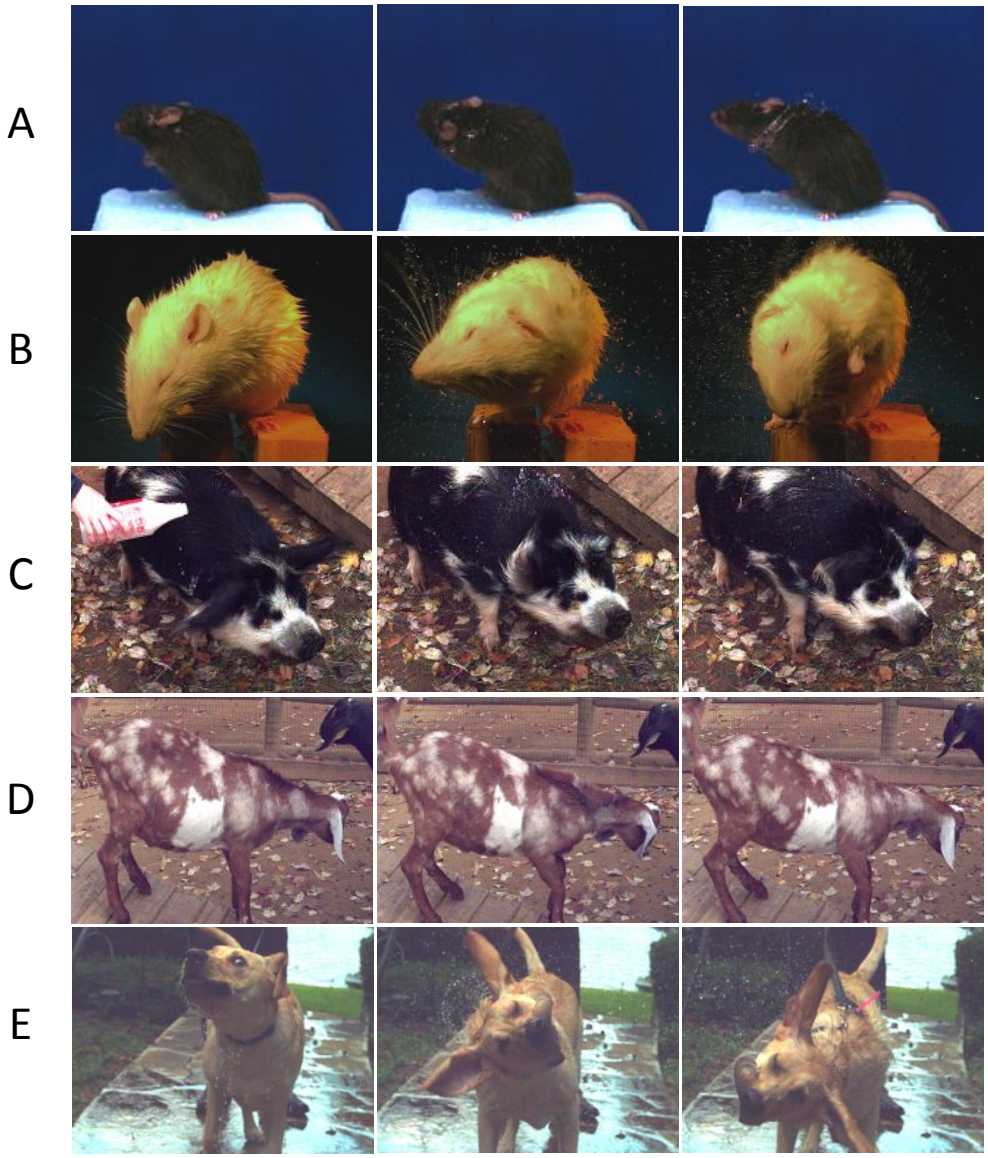

Figure 41: Photo-sequences of animals filmed in this study. **(A)** Adult Mouse. **(B)** Rat. **(C)** Kunekune Pig. **(D)** Boer Goat. **(E)** Labrador Retriever.

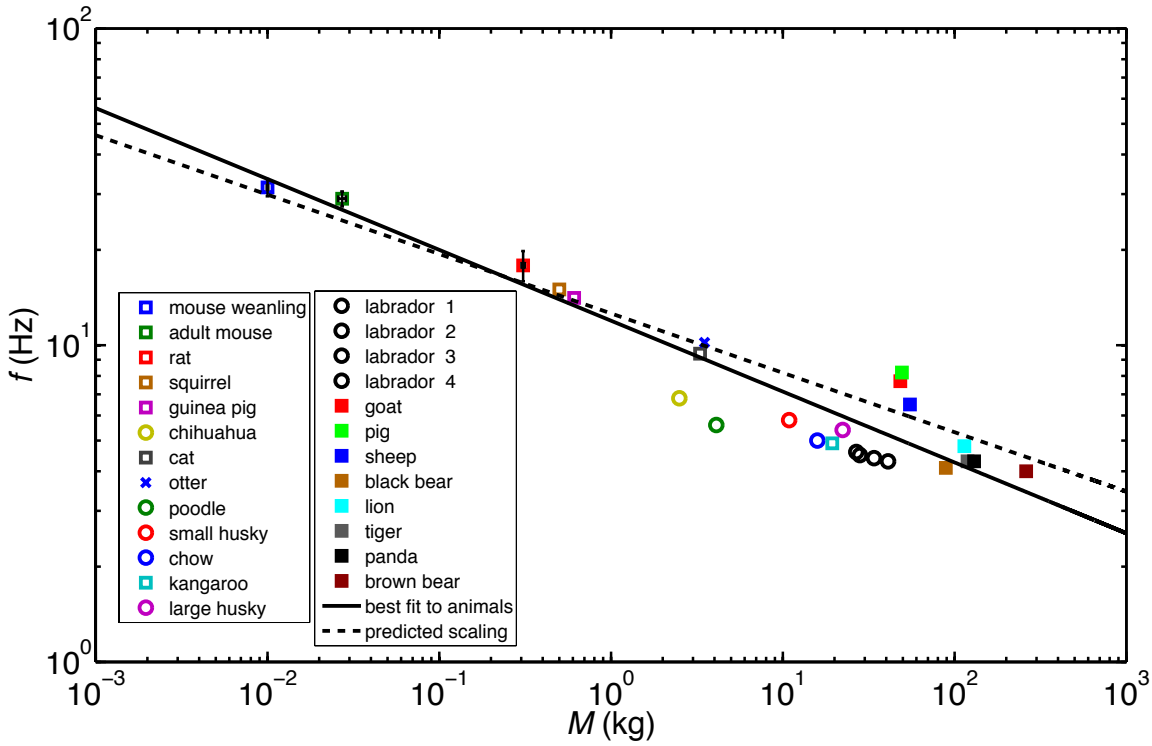

Figure 42: The relation between shaking frequency f and animal radius R. Dogs are denoted by a ◯, other mammals by a □, and the semi-aquatic otter by an X. Best fit is given in Eq. (8.1) Error bars indicate the standard deviation of measurement.

Fig.42 and Table 5 show the relation between frequency of shaking f and animal mass M for the animals in our study. To calculate a best fit, we tried to obtain a fair and uniform sample of the animals studied. The mass and frequency changed little within certain samples groups, such as juvenile mice, adult mice, and adult rats. In these groups, only the average of each group was considered to avoid bias towards particular species in our best fit. Specimens of certain canine breeds such as Labradors and Huskies were obtainable in a wider range of masses and so were considered individually rather than as an average for each breed. Otherwise, we calculated a best fit using a sample that consisted of one specimen of each canine breed and one specimen of each non-canine species. In all, among the 33 animals measured, we used a sample of 25 points to determine our best fit.

Table 5: Size and shaking speeds of animals studied. The radius and mass of the squirrel, black bear, and brown bear were estimated from the sizes of average adults in literature[137,138,140,142]. The radii measurements of the lion and tiger were unattainable by the Zoo staff and were estimated similarly sized adults in literature[135,136].

	M	R	f	$R\omega^2/g$
	Mass (kg)	**Radius (cm)**	**Frequency (Hz)**	**Non-dimensionalized Centrifugal Acceleration**
Mouse Weanling *Mus musculus*	0.01 ± 0.0001	1.2	31.5 ± 2.0	72
Adult Mouse *Mus musculus*	0.0272 ± .0014	1.3	29.0 ± 1.6	66
Rat *Rattus norvegicus*	0.3077 ± .007	2.6	17.869 ± 2.0	53
Grey Squirrel *Sciurus carolinensis*	0.50	3.0	15.0	43
Guinea Pig *Cavia porcellus*	0.606	3.2	14.1	40
Chihuahua *Canis lupus familiaris*	2.5	5.0	6.8	14
Domestic Cat *Felis catus*	3.3	5.9	9.4	33
River Otter *Amblonyx cinereus*	3.5	5.5	10.2	36
Poodle *Canis lupus familiaris*	4.1	5.9	5.6	12
Siberian Husky *Canis lupus familiaris*	10.9	8.8	5.8	19
Chow *Canis lupus familiaris*	15.9	10.0	5.0	16
Kangaroo *Macropus rufus*	19.4	8.1	4.9	12
Siberian Husky *Canis lupus familiaris*	22.3	11.2	5.4	21
Labrador Retriever 1 *Canis lupus familiaris*	26.8	11.9	4.6	16
Labrador Retriever 2 *Canis lupus familiaris*	28.1	12.1	4.5	15
Labrador Retriever 3 *Canis lupus familiaris*	34.0	13.3	4.4	16
Labrador Retriever 4 *Canis lupus familiaris*	41.0	14.1	4.3	17
Boer Goat *Capra hircus*	48.3	13.3	7.7	50
Kunekune Pig *Sus scrofa*	49.4	13.3	8.2	57
Gulf Coast Sheep *Ovis Aries*	55.0	15.0	6.5	40
Black Bear *Ursus americanus*	90	15	4.1	16
African Lion *Panthera leo*	114	15	4.8	22
Sumatran Tiger *Panthera tigris sumatrae*	119	16	4.3	19
Giant Panda *Ailuropoda melanoleuca*	130	18.1	4.3	21
Brown Bear *Ursus arctos horribilis*	260	24	4.0	24

The best fit using the method of least squares yields

$$f \sim M^{-0.22}, \qquad (R^2 = 0.95, N = 25). \tag{8.1}$$

Note that the goodness of fit R^2=0.95 is high, despite over four orders of magnitude in mass (0.01 - 260 kg) of the animals considered. Among these animals, we observe a clear dependency of shaking frequency on body size: mice must shake at 30 Hz, dogs at 4.5-8 Hz and bears at 4 Hz.

In **Fig.42**, the vertical distance between the points and the best fit denotes the vigor of the animal's shake with respect to the average. We suspect deviations from the trend are due to modifications in shaking style according to the animal's anatomy, or as in the case of dogs, centuries of domestication. While animals generally shook on four legs, rodents such as mice and rats stood on hind legs to shake (**Fig.41**)a-b). Otters and sheep did not shake at frequencies lower than the best fit, as one might expect from the lower adhesion of drops to their waxy fur.

The largest animals such as bears shook at frequencies of 4 Hz, slightly higher than predicted by the best fit (3.5 Hz). Generally animals in the size range of 4-260 kg exhibited a slightly smaller range in frequency (4-6 Hz) than indicated by the best fit (3.5-9 Hz). This departure from the best fit is likely due to the decreasing importance of shaking with size. The largest animals such as elephants need not shake because of a combination their large thermal mass, thickness of dermal layers, and lack of hair. Thus, we expect animals to depart from the observed trends at some critical size, and this departure may in fact begin for the largest animals studied.

8.1.2 Shaking Kinematics

Four Labrador retrievers ($M = 32.5 \pm 6.5$ kg) served as model organisms to characterize the shaking kinematics because they were tame and accessible. A typical shake by a Labrador is shown in **Fig.40**a, where a fluorescent fiducial marker is taped to the dog's fur in the middle of its back (**Fig.40**b). The angular position θ of the marker with respect to the

vertical is shown in **Fig.40**c and Video S14. We find the shake is closely approximated by simple harmonic motion, in which

$$\theta(t) = A\sin(2\pi f t) \qquad (\mathrm{R}^2 = 0.98,\ \mathrm{N} = 3) \tag{8.2}$$

where the shake amplitude is $A = 90 \pm 10^\circ$ (N=3) and the frequency (in cycles per second) is $f = 4.5 \pm 0.25$ (N=3) . The peak angular velocity of the shake is $\omega = \mathrm{d}\theta/\mathrm{d}t \sim 2\pi f A$. We observed qualitatively that drops are shed continuously throughout the cycle, with small bursts of increased shedding when the fur changes direction.

We observe in **Fig.40**b a surprisingly large amplitude of motion $A \approx 90^\circ$ despite the dog's four paws remaining in contact with the ground. Rotating the dog's skin by hand, while keeping the vertebrae static, indicates the dermal tissue alone has a maximum deflection of $A_s \approx 60^\circ$. Loose dermal tissue, which roughly contains all substance between fur and muscles, had been previously hypothesized[106] to reduce the energetic cost of locomotion by facilitating limb movement, and we find here it serves another purpose by increasing the amplitude of the shake.

We infer the vertebral motion during the shake has a smaller amplitude $A_v = A - A_s \approx 30^\circ$, as shown by the time course of the dotted line in **Fig.40**c. The vertebral amplitude is three times less than the dermal tissue amplitude during the shake, indicating that loose dermal tissue has an important role in amplifying the shake. We also observed loose dermal tissue in other animals, such as our x-ray videos of rats (Video S15). In our analysis of the forces involved, we will see how this increase in amplitude improves the efficacy of the shake through increasing the centrifugal force on drops within the fur.

8.1.3 Drops ejection from hair clumps

We now rationalize the observed power law scaling by consideration of the physics of drop release from an animal's furry surface. A wet furry animal will drip water due to the influence of gravity. As the animal dries, the falling ligaments of water transform into streams of drops. Because the animal coat is wetting, it is energetically favorable for this departing

fluid to follow the animal's hair, from root to tip. Photographs of wet animals such as otters, bears, and dogs (**Fig.43**) often show wet animal hair forms a fairly uniform series of wet aggregations, resembling wetted paintbrush bristles. These clumps are formed through a complex process that depends on hair spacing, length, curvature, material properties and degree of wetness[100,181–184]. Tabulated properties[106,185–188] of animal fur, length, diameter, density, and stiffness, show no dependency on animal size for the range of animal masses we have considered (**Fig.43**, **Fig.44**).

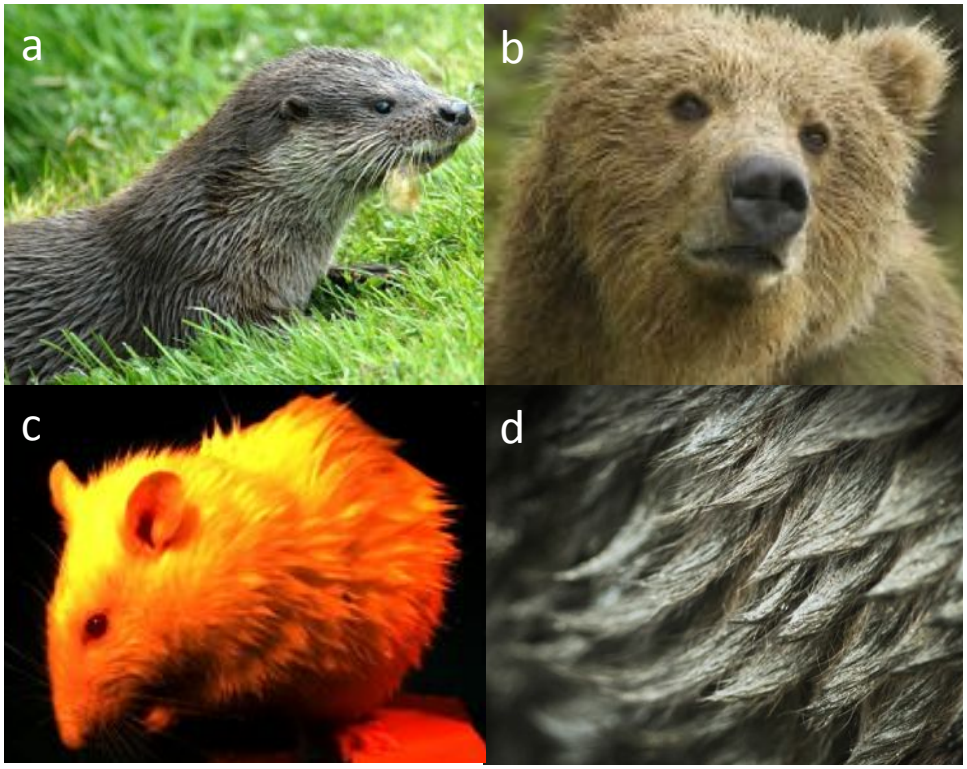

Figure 43: Wet fur aggregation array shown on a **(a)** otter, **(b)** a brown bear, **(c)** an rat, and **(d)** a black Labrador. (photo credit: stock photos (a)-(b), Andrew Dickerson (c), and Phil Roman (d))

We performed a series of drip tests with variable-sized paintbrushes, ranging in diameter from 1.2 to 11.5 mm meant to simulate the range of hair clump sizes observable in animals. We shaved the tips of the paintbrush bristles flat in order to obtain uniformity in our experiments. The paintbrushes are then suspended in a "wet-dog simulator" (see **Fig.7** in Chapter 2), consisting of a high-strength spinning frame that rotates the brush along with

a high-speed camera at a given frequency f. This device allowed us to visualize the flow of fluid as if a dog is shaking at the frequency the device is spun.

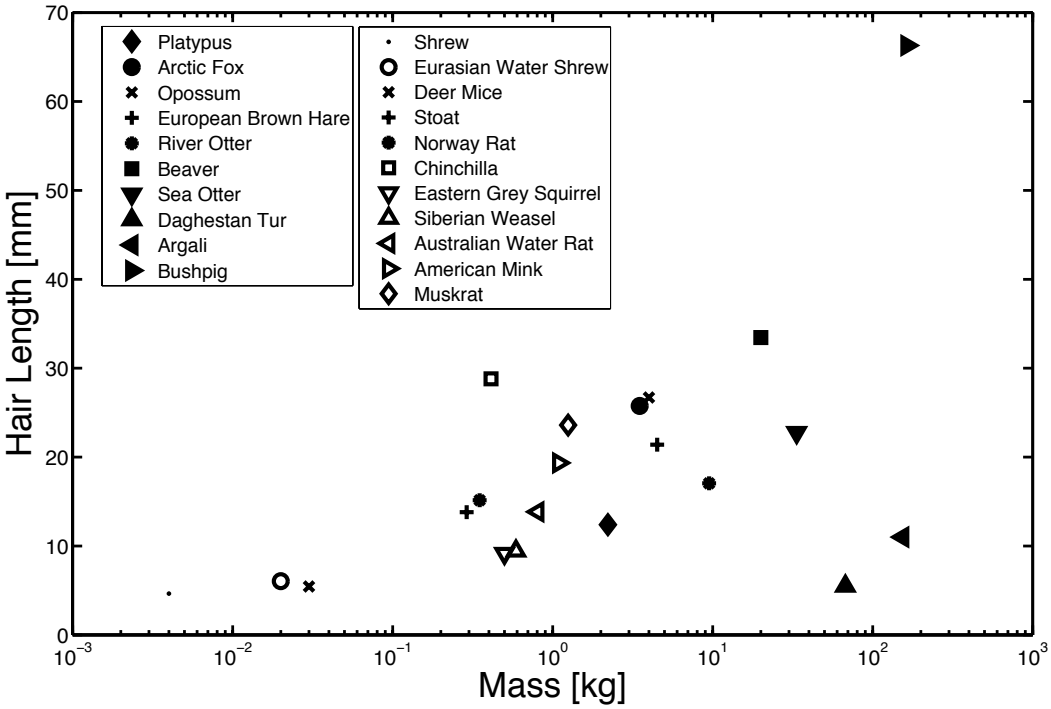

Figure 44: Hair length of mammals versus body mass.

8.1.4 Visualization of drop release

The detachment of drops may be clearly visualized using our system. **Fig.45**a shows a video sequence of drop release from a paintbrush under gravity. The corresponding drop release from a spinning brush (at 2.61 m/s with rotation rate of 610 rpm) is shown in **Fig.45**b, and is visually similar to release due to gravity. In both processes, fluid entrained from the brush engorges the drop. This engorgement occurs at a rate that depends on the remaining moisture content of the brush and the applied centrifugal or gravitational forces. During engorgement, the drop remains pinned to the brush. In **Fig.45**a, pinning occurs at the circumference of the hair clump, whereas in **Fig.45**b, at points within the center of clump. Once the drop has grown to a critical size, the pinch-off and release process is quite fast, occurring within 10 ms. In both gravitational and centrifugal force-driven dripping, a portion of the drop remains attached to the clump after release.

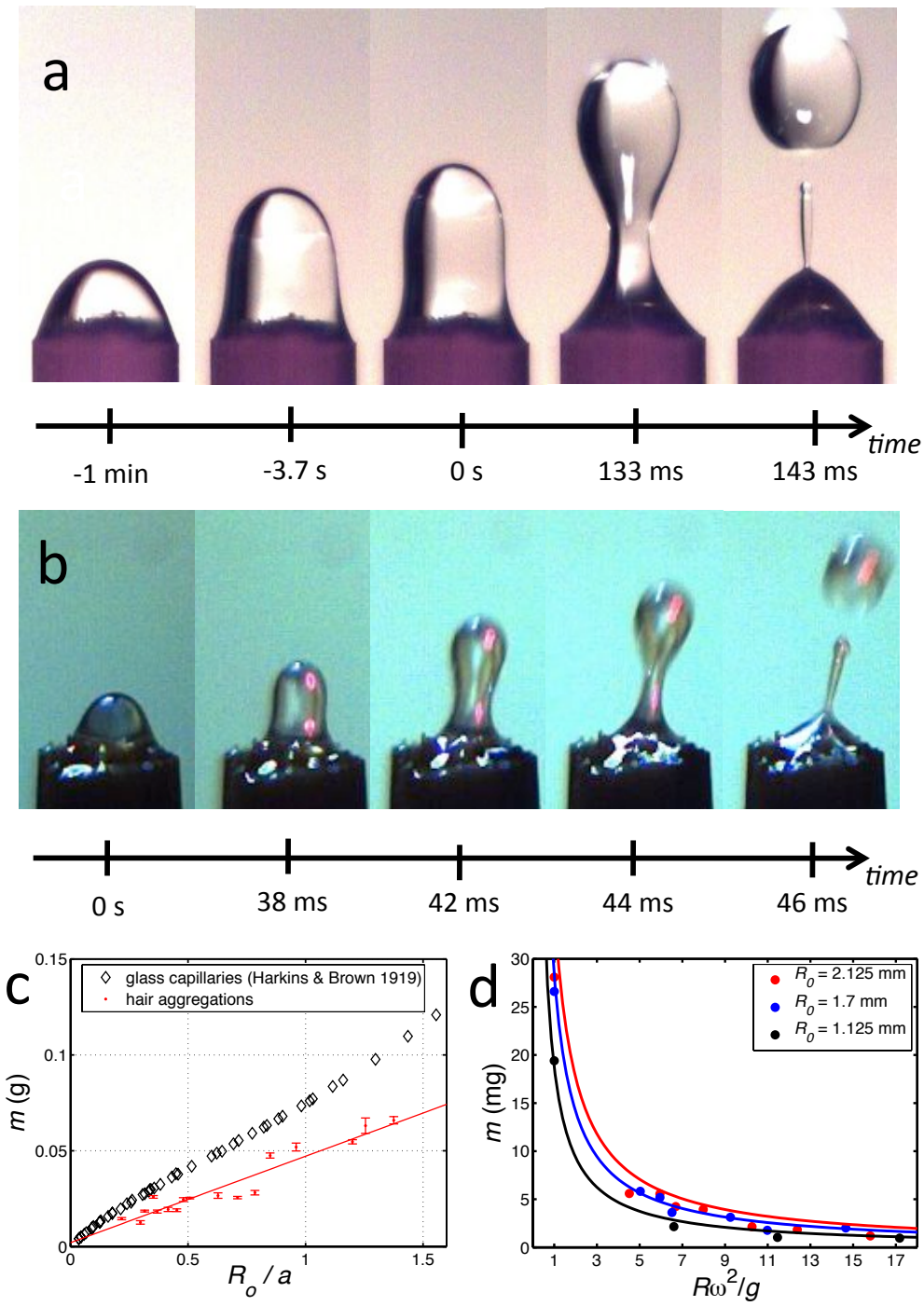

Figure 45: Drop departure from fiber aggregations. **(a-b)** Video sequences of drop ejection under gravity and due to spinning, respectively. In the latter, centrifugal forces are $R\omega^2/g = 11$ and smaller drops are ejected. **(c)** The dependence of drop mass m and hair aggregation size R_0 for dripping under gravity. The mass of drops dripping from from glass capillaries is shown for comparison. **(d)** The relation between drop mass and dimensionless centrifugal acceleration for three hair aggregations of varying diameters. Best fits in (c) and (d) are given by Eq. (8.3) using $F(R_0/a) = 0.4$.

This phenomenon of drop release has been well-studied in dripping from capillaries[189,190] in the context of intravenous drug delivery and in spinning disk spray applications[191,192]. In these cases, drop size can be very carefully controlled. The conditions for drop detachment from a capillary are given by Tate's Law[193,194]: to detach, a drop's effective weight mg must overcome the surface tension force σR_0 binding the drop to adjacent hairs, where m is the drop's mass, $\sigma = 72$ dynes/cm is the surface tension of water and R_0 is the paintbrush radius. During shaking, drops have a larger effective weight due to centrifugal forces, $F_{cent} = mR\omega^2$, which for mammals we have filmed can be 10-70 times gravity (Table 5). As shown in **Fig.45**a-b, the high centrifugal forces cause extruded drops to be smaller; we will see later that they result in far more fluid extracted than simply by gravity.

Note that because our device spins at constant speed, our experiments do not account for the dynamics of oscillating, pendulum-like motion, which may also act to eject drops. The relative magnitudes of centrifugal to acceleration forces are comparable, $F_{accel}/F_{cent} = |\frac{d\omega}{dt}/\omega^2| = A^{-1} \approx 0.65$, suggesting that drops are likely to be shed by a combination of both mechanisms; nevertheless we only consider centrifugal forces in our analysis.

8.1.5 Tate's law applied to hair clumps

Our experiments reveal that drops formed by wet paintbrushes very consistently satisfy Tate's Law. **Fig.45**c shows the dependency of drop mass on clump size R_0 under gravity: drop mass is linearly proportional to clump size, as shown by the red points. Note this behavior is similar to that shown previously for capillary tubes, as shown by the diamonds in **Fig.45**c. **Fig.45**d shows the dependency of drop mass on rotational speed for three clump sizes (R_0 = 1.1, 1.7, 2.1 mm): drop mass is inversely proportional to centrifugal acceleration $R\omega^2$. Together, these findings demonstrate the modified Tate's Law for the mass of drops released,

$$m = (2\pi\sigma R_0/R\omega^2)F(R_0/a), \tag{8.3}$$

where σ is surface tension of water, ρ is density, and $a = \sqrt{\sigma/\rho g} \approx 2.7$ mm is capillary length. For the best fit trend lines in **Fig.45**c-d, we estimate the correction factor[195] for hair clumps as a constant function, $F(R_0/a) = 0.4$. We plot $F(R_0/a)$ for hair clumps of various size in **Fig.46**. The correction factor for an analogous system, glass pipettes, was previously determined to be a non-constant function by Harkins and Brown (1919). Measurements of this function in our experiments yielded a small range, from 0.3 to 0.6, indicating the low impact of approximation as a constant function. As shown by the agreement between the solid lines and the experimental data in **Fig.45**c-d, Eq. (8.3) well predicts the mass of the drops shed for an animal shaking at a fixed rotational velocity ω with hair clumps of size R_0.

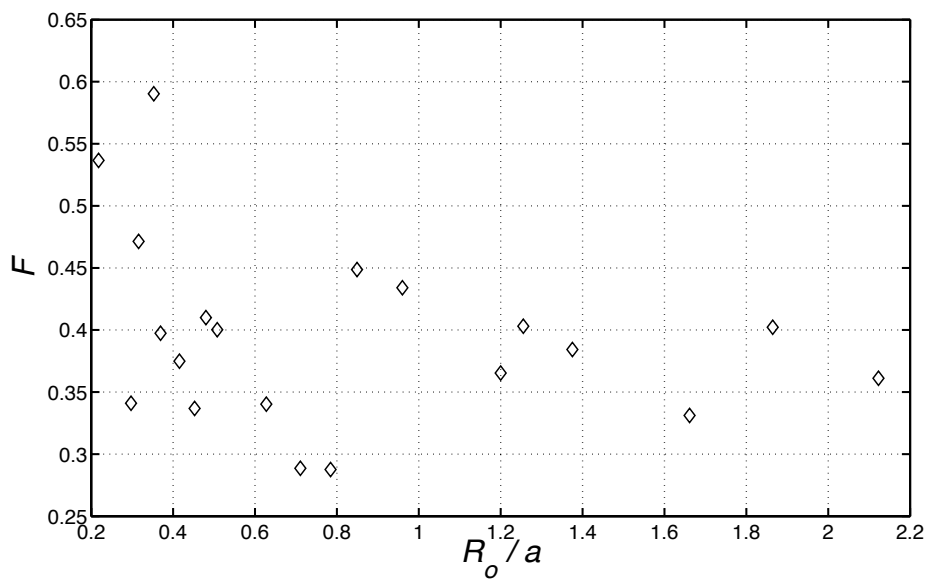

Figure 46: $F(R_0/a)$ for hair clumps of various size.

We surmise the drying of animals proceeds as follows. Large drops, whose size are on the order of the capillary length, naturally depart the animal due to gravity as in **Fig.45**a. However, thin films of water on the hairs and the smallest drops remain attached and so can only be removed by shaking, as shown in **Fig.45**b. Equation 8.3 shows that if an animal increases its rotational velocity and so its centrifugal force compared to gravity, it may extend the range of drop masses shed. However, at a given rotational velocity, the residual

drop masses left behind after dripping, shown in **Fig.45**a-b, may be too small to be ejected by centrifugal forces, and so may remain attached to the animal.

8.1.6 Prediction of shaking allometry

We may simplify Tate's Law to formulate a "wet-dog shake rule," an allometric relation between animal mass and shaking frequency. Formulation of such a scaling law requires determining which variables within Eq. (8.3) are independent of animal mass and so may be fixed as constant. We consider each of the five variables in turn (σ, A, m, R_0, f), turning first to variables that are independent of animal mass, as found either in our experiments or in literature. Clearly, material properties of the fluid such as surface tension σ are independent of animal mass. In our experiments, we observe shaking amplitude A varies over a range of 60-110° without clear trends in animal mass. We find hair properties[108,142,196–199,199–225] such as hair length and density do not vary systematically across mammal mass, as shown in **Fig.43**, **Fig.44**, and **Fig.47**, respectively. Thus we fix wet hair clump radius, which depends primarily on hair length and density.

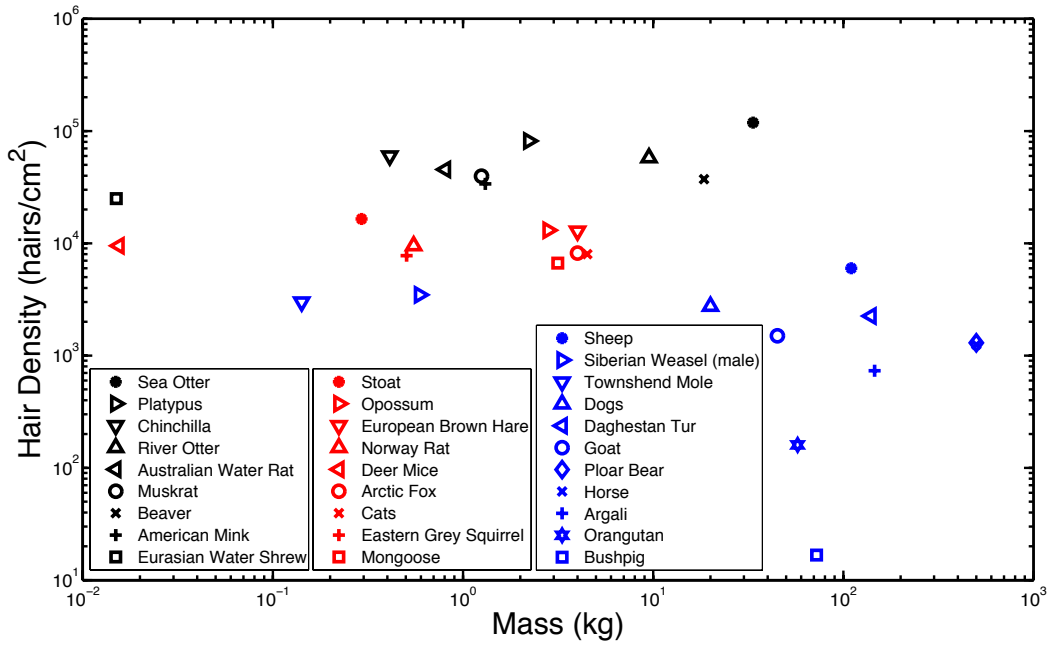

Figure 47: Hair density of mammals versus body mass.

The remaining variables in Eq. (8.3) are the radius R, which is an independent variable,

and two dependent variables, the chosen shaking frequency f and the shed drop size m. The shed drop mass is a function of both the radius and the frequency of shake. In particular, over the range of $R\omega^2/g$ = 10-70 for animals studied (Table 5), Eq. (8.3) predicts drop mass will vary by a factor of 7. This amount is low in comparison to the variation in other variables considered. Variation in animal radius R is a factor of 24 (from 1 to 24 cm); moreover, variation in the square of frequency (4 to 30 Hz) is a factor of 50. Each of these factors are greater than seven. Moreover, their combined variation of $R\omega^2$ varies by an even larger factor of 1200 if R and ω were to vary independently. Thus, we assume drop mass is constant and proceed with our scaling to determine the relation between frequency and radius.

We apply an allometric relation relating animal mass and radius previously found by McMahon and Bonner (1983)[161]: animals are nearly isometric according to Kleiber's Law such that $M \sim R^{8/3}$. Applying this law, the resulting scaling relation between animal mass and shaking frequency is

$$f \sim M^{-3/16}. \tag{8.4}$$

By shaking at such frequencies, furry animals act like a high-pass filter, causing drops above a critical size m to eject. This critical drop size is determined by the scaling pre-factor in Eq. (8.4), which depends on the drop's surface tension and density according to Eq. (8.3). It is noteworthy our predicted exponent of -0.19 (R^2=0.92) is close to the observed value of -0.22. Our exponent is within the 99.8% confidence intervals for our experimental best fit indicating that there is only a 0.2% chance our the predicted exponent is different from the measured one. We attribute this small discrepancy, which scales as an infinitesimal $M^{0.03}$, to simplifications in our model, most likely regarding animal radius.

The increase in shaking speed for smaller animals is important in compensating for their smaller radius. This tuning of shaking frequency with body size is necessary to generate the large centrifugal forces required to shed drops, $R\omega^2/g =$ 10-70 gravities, for the animals listed in Table 5. If for example all animals shook at the frequency of a dog, the smallest

animals would have insufficient force to remove drops: for example a mouse shaking at 4 rather than 30 Hz would generate only 1 gravity of centrifugal force, and would remain just as wet.

8.1.7 Shaking animals achieve similar residual moisture content

In our experiments with paintbrushes, we found the frequencies required for drop detachment depend on clump size R_0. We now use experiments with real animal fur to measure how clump size changes during longer durations (30 seconds) of shaking. **Fig.48**a shows the hair clump configurations at various speeds of rotation for a 6.3 cm^2 square sample of deer fur. As rotation speed increases so that centrifugal forces increase from from 1 to 40 gravities, the clumps separate into a cascade of smaller clumps. By weighing these clumps, we find that this separation is accompanied by an exponentially increasing difficulty in drying, which gives further rationale for the frequencies used by the animals.

Fig.48b shows the relation between the centrifugal forces applied and the remaining moisture content *RMC* within our deer fur sample. We define *RMC* as the ratio of the post-shake mass to the initial mass of water in the clump, as was done by textile-drying engineers[226]. In **Fig.48**b the limiting *RMC* values of $D = 30\%$ show excellent agreement with our measurements of $RMC = 0.31 \pm 0.12$ (N=10) on live rats, suggesting our experiments with spun deer hair are representative of shaking live animals. From the combination of these results, we conclude 30% RMC is the lowest level of dryness obtainable using shaking. Moreover, the lowest *RMC* values of 0.3 - 0.4 values occur for speeds in which the associated centrifugal force is

$$R\omega^2/g > 10, \tag{8.5}$$

as indicated in the shaded region in **Fig.48**

As shown in Table 5, all shaking mammals in our study have centrifugal forces in the range of 10-70, a relatively small range considering the 4 orders of magnitudes of mass of the animals. Notably, this range of forces coincides with the region of peak dryness given

by Eq. (8.5), which was found independently with our wet-dog simulator. We conclude that animals shake to achieve nearly equal and maximal levels of dryness.

8.1.8 Physical basis of residual moisture content

We may rationalize the trends observed in **Fig.48**b, beginning with the initial *RMC* of deer fur under gravity. The mass of water in the hair is proportional to the corresponding water column height within the fur. When fur is initially wetted, surface tension competes with elasticity to bring the water column between the hairs to an equilibrium height[100] of

$$H_{initial} = L - \left(\frac{9}{2} d^2 L_{EC}^2 / \cos\theta_e\right)^{1/4}, \tag{8.6}$$

where hair length in the deer fur sample $L \approx 40$ mm, hair follicle radius $b \approx 200$ μm, inter-hair spacing $d \approx 0.028$ cm, elastocapillary length is $L_{EC} = \sqrt{EI/\sigma b} = 57$ cm, Young's Modulus is $E = 3.7$ GPa, $I = \pi b^4/4 \approx 1.26 \times 10^{-3}$ mm^4 is the area moment of inertia and $\theta_e = 60^\circ$ is the equilibrium contact angle of water on hair[188]. We find this model is fairly accurate for our 6.3 cm^2 square sample of deer fur. Given its combined water column cross-sectional area A_{fur} of 2.4 cm^2 (measured by the area of space between the furs): we predict the hairs will retain $m_{initial} = \rho H_{initial} A_{fur} = 4.4$ g of water whereas it held 4.7 g in our experiments. Thus elastocapillarity theory is sufficient to account for the wet weight of deer fur under gravity, and the discrepancy between experiment and theory suggests water may soak into the hair fibers.

When fur is spinning, the associated centrifugal force competes with surface tension to decrease the height of the water column to a modified Jurin's height $H = 2\sigma\cos\theta_e/\rho R\omega^2 d$. Using the definition of *RMC*, we may write $RMC = H/H_{initial} + D$, where D is a free parameter used for fitting the asymptote in **Fig.48**b. This parameter D cannot be predicted with our simple model, as it represents the moisture that soaks into the rough surfaces of the hair and skin, and cannot be removed even under extreme centrifugal forces[227–230]. The remaining moisture content simplifies to

$$RMC = C/R\omega^2 + D \tag{8.7}$$

where $C = 2\sigma\cos\theta_e/\rho d H_{initial} = 14.2$ m/s^2 and D = 0.3. Our measurements of RMC of deer fur in **Fig.48**b show a power law qualitatively consistent with Eq. (8.7), having a goodness of fit R^2 = 0.93 within the range of $R\omega^2/g$ =2 - 35.

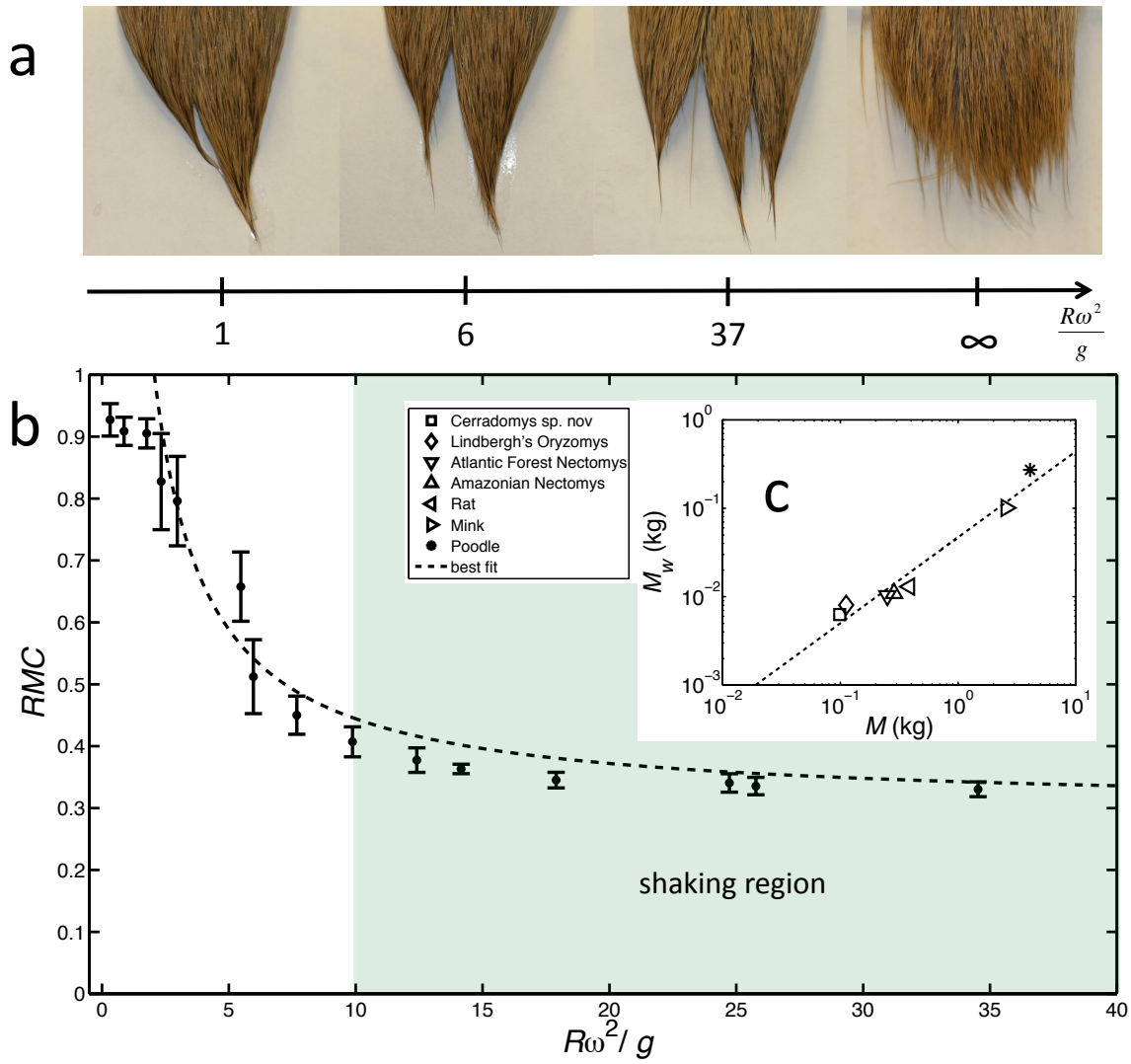

Figure 48: Properties of hair clumps measured using our Wet-Dog Simulator. **(a)** The separation of wet aggregations upon spinning. **(b)** The relation between *RMC* and non-dimensionalized centrifugal acceleration. Error bars indicate the standard deviation of measurement. **(c)** Mass of water held on a wet animal's body versus animal mass. Data for wet and dry masses for Cerradomys. sp. nov, Lindbergh's Oryzomys, Atlantic Forest Nectomys, and Amazonian Nectomys were collected by Santori (2008)[112], while the Mink was gathered from Korhonen (2002)[113].

For small rotation speeds $R\omega^2/g < 2$, *RMC* is sigmoidal and outside the scope of our model, due to elastic and gravitational forces becoming comparable with centrifugal forces in this regime.

Using our measured trends in moisture content in **Fig.48**b, we may quantify the benefits of the animal's loose dermal tissue, observed in **Fig.40**c. Previously, we found loose dermal tissue increases the shake amplitude by 3-fold, and thus the speed of shaking by 9-fold. If dermal tissue were tight rather than loose (as on humans), animal shaking frequencies would cause *RMC* values to remain close to 1, indicating the animal would remain wet. Thus, an important role of the loose dermal tissue is to increase the efficacy of the shake, as shown by the sensitivity of the *RMC* to changes in skin speed.

8.1.9 Shaking energy expenditures

We may assess the effectiveness of shaking by comparing the energetic costs of shaking versus evaporating the water. The shaking energy can be estimated as the peak kinetic energy for simple harmonic motion, given by $E_{shake} = \frac{1}{2}M(R\omega)^2$. If animals can shake 70% of their water off, as shown previously, the energy required to evaporate that mass of water is given by $E_{evap} = 0.42\lambda M_w$ where M_w is the mass of the water on the animal. The coefficient 0.42 is a product of 0.6, the fraction of energy needed from the animal to evaporate water[115] and 0.7, the fraction of water an animal can shake off as found in our experiments.

Fig.48c shows the relation between an animal's body mass M and the mass of water in its fur, M_w. Data for 7 mammals was found by combining our own measurements of wet animals along with others[112,113]. The trend follows the power law $M_w = 0.047M^{0.97}$, where M and M_w are both in kilograms, with high accuracy ($R^2 = 0.95$, N = 7). The mass of the water held in the fur is approximately 3-10% of the animal's body mass for the masses considered (0.1-4 kg).

We combine the above energetic estimates above with our measurements of animal

frequency to calculate an efficacy of shaking. We define this efficacy as the ratio of the energy expended to shake to the energy expended to air-dry as $\eta = E_{shake}/E_{evap}$. We find that over the 4 orders of magnitude of mass for animals studied, this efficacy has a small range of $10^{-4} - 10^{-3}$. In this range, all values are far less than one, indicating the great energy savings achieved by shaking.

8.2 Discussion

8.2.1 Predictions based on power

In tests with animal hair, we found the observed frequencies were capable of drying the animal appreciably, as defined by removing 70% of its accumulated water. Furthermore, we found that increased speeds imparted to the fur would achieve diminishing return. Thus, the animal obtains a reasonable amount of dryness without expending an excess of energy. The work per shake W of an animal[161] scales as the mass of its muscles ($W \sim M$). The kinetic energy expended per shake is

$$W \sim MR^2\omega^2 \sim MR^2 f^2 \tag{8.8}$$

thus

$$f \sim R^{-1} \sim M^{-1/3}. \tag{8.9}$$

We note that our observed scaling exponent of -0.22 falls between the minimum frequencies for drop release (-0.19) and the maximum frequencies based on power output (-0.33). Thus, it may not be possible for animals to dry further because they may be at the upper limits of shaking speed they can generate. In studies of galloping, stride frequencies of small mammals varied from 2- 9 strides/second, whereas the frequencies of shaking are faster (4-30 shakes/second). Studies regarding drug-induced tremors in mice reported shivering frequencies to be very close to shaking frequencies at 25 shakes/second[231], which is quite possibly at the limits of oscillatory motion of muscle.

8.2.2 Comparison with other scaling laws

Our measurements of shaking frequency may be related to other frequencies associated with animal movement. Stahl measured the heartbeat frequency[232] of resting animals scaling as $f_{hb} \sim M^{-0.25}$. Joos *et al.* found that the wing beat frequency[233] in bees scales with the bee's mass as $f_{wb} \sim M^{-0.35}$. Heglund found frequency[234], in the trot-gallop transition, for mice, rats, dogs, and horses, scales as $f_{trot} \sim M^{-0.14}$. He noticed for all animals tested, stride frequency became asymptotic, changing less than 10% as the animals increased their speed from the trot-gallop transition to their maximum. These power law scalings are comparable in exponent to the ones we measured for shaking animals, possibly because similar muscles are used to power both locomotion and shaking.

8.2.3 Scaling frequency with body radius

In predicting a scaling for frequency, care must be made in choosing an appropriate independent variable. There are two choices to characterize body size, radius and mass. When choosing body mass, our model fit the experimental results quite well. Rewriting our model, Eq. (8.4), in terms of frequency and body radius yields $f \sim R^{-1/2}$. This result is in high variance with respect to experimental data in Table 5, which yields $f \sim R^{-0.77}$ (R^2 = 0.96). This discrepancy arises from approximating body proportion with a single circumference measurement around the shoulders. However, this is not the only region in need of drying. In fact, other regions of the animal will have a different characteristic radius. Consequently, an animal's mass, which scales as its volume, more accurately captures the average radius of the animal the drops encounter during shaking. This reasoning explains why our scaling with respect to animal mass ultimately yielded a closer fit to experimental data.

8.2.4 Predictions and exceptions

We hypothesize shaking when wet is an ancient survival mechanism, dating back to the emergence of furry mammals. Many Pleistocene mammals were covered with hair. Giant

beavers[235], similar in size to a black bear, and short-faced bears[236], similar in size to grizzlies, would have likely shook similarly to their modern counterparts. Though the ability to shake likely spans generations of furry mammals, it is not a characteristic of all mammals, even of those today. The largest mammals' thermal mass is a likely cause for its inability to shake. In addition, aquatic mammals and those covered with a hard shell, such as an armadillo have no need to shake dry. Other animals with specialized slow lifestyles such as the giant sloths may not posses the speed to initiate a shake.

Hairless mammals may have no shaking instinct. While filming we observed hairless guinea pigs did not shake, but only shivered. In personal observations, some species such as the sparsely-haired warthog spend their days bathing in muddy water. We expect that nearly hairless species, adapted to hot environments, have not developed the behavior to shake when wet.

We saw earlier that loose dermal tissue played a role in increasing the speed, force and efficacy of the shake. This constraint may also prevent certain species from shaking. For instance, while humans do not generally have loose dermal tissue, some humans can use their long hair to shed water. This technique involves repeated motion of the head and upper torso in the dorso-ventral plane to whip water from their hair. Although the head is oscillated at the low frequencies of only 1-2 Hz, the hair length aids to increase the amplitude and speed at which hair tips are whipped, and consequently the ensuing dryness.

8.3 Chapter Summary

In this study, we demonstrated that reciprocal high-speed twisting commonly observed in dogs has a broad generality among mammals. We found that drops remain adhered to a wet animal's hair due to the forces of surface tension. To eject drops and achieve dryness levels of 30%, we found animals generated centrifugal forces equivalent to 10-70 gravities. In order for animals of variable size to attain this magnitude of force, we predicted animals must shake at frequencies of $f \sim M^{-3/16}$, which was similar to experimentally measured

frequencies. We conclude animal frequency is tuned to (1) the animal's size and (2) the properties of water, namely surface tension and density, which set the magnitudes of the centrifugal and capillary forces in our model. Consequently, such mechanisms work poorly when animals are subjected to fluids with properties different from water such as crude oil, whose wetting properties and inability to evaporate prevents the shake from being effective.

CHAPTER IX

CONCLUDING REMARKS

"Consider it pure joy, my brothers, whenever you face trials of many kinds, because you know that the testing of your faith develops perseverance. Perseverance must finish its work so that you may be mature and complete, not lacking anything. If any of you lacks wisdom, he should ask God, who gives generously to all without finding fault, and it will be given to him." -James 1:2-5 (New International Version)

We have reported the results of a combined theoretical and experimental thesis on mosquito locomotion in rainfall, hyperdense flight mediums, and various phenomena arising from fog and dew deposition. In Chapter 3, we investigated how *Anopheles gambi* mosquitoes and similarly sized insects survive raindrop impacts, and quantified the forces associated with those impacts. The mosquito's low mass causes raindrops to lose little momentum upon impact and so impart correspondingly low forces to the insect. We derived relations for the transfer of momentum between the insect and raindrop to predict the insect's downward velocity post impact. An analysis of drop deformation was preformed and we may conclude that drops do no splash upon impact with a mosquito. Our findings demonstrate that small fliers are robust to in-flight perturbations. In Chapter 4, we identified three outcomes of raindrop collisions: drops push the insect while remaining intact, coat the insect, or splash. The type of impact observed is dependent upon the insect's mass and size. We presented a mathematical model that predicts impact force and outcome consistent with those found in experiments. We pinpointed a critical mass of 0.3 g for which flyers achieve both peak acceleration (100 g) and applied force (10^4 dynes) from incoming raindrops; designs of flying robots similarly massed should be avoided. Future researchers

may identify how our results will change for other drop kinematics. There likely exists a small range of sphere sizes and masses that can produce any of the three impact modes based on initial drop velocity and size.

In Chapter 5, we showed simple fogs of water droplets, devoid of chemicals, are effective at obstructing the flight of *Anopheles freeborni* mosquitoes. Using high-speed video, we filmed their flight in heavier-than-air fluids such as fogs produced by household humidifiers and R134a gas. In gases denser than air, mosquitoes cannot maintain flight stability, but pitch and roll uncontrollably until they fall to the ground. We found the aerodynamic drag force of denser-than-air flight environments is sufficient to render a mosquito's gyroscopic sensors and wingbeat controllers, their halteres, ineffective. We compared the change in force required to drive the rapidly oscillating halteres imposed by increased drag to the inertial forces induced by adding glue masses of 10 nanograms to each haltere. Mosquitoes with such a minor treatment executed flight maneuvers similar to mosquitoes in fog, indicating their halteres are highly tuned to aerodynamic properties of normal air, making the halteres sensitive to contaminants. The failures of mosquito flight in fog reveals potential methods for mosquito control that do not require insecticide-laced particles. In addition to insecticide research, future researchers may choose to investigate the effects of hyperdense mediums on the flight performance of non-haltere-bearing insects, which also rely on airflow characteristics to sense flight dynamics[68,69] .

In Chapter 6, we characterized the folding process of small, wet, insect wings from flat into taco shapes. We observed a wing begins to bend as the drops atop grow larger through coalescence. A very thin wing will fold more tightly as the drop evaporates, whereas a thicker wing will reopen to its natural state. We derived a two-dimensional model to determine the magnitude of folding for a given drop size spanning the wing's width, and presented folding-resistant design suggestions for micro-aerial vehicle wings.

Certainly, deposited moisture on an insect's body can hinder locomotion. In Chapter 7 we investigated three water deposition removal techniques employed by mosquitoes. They

shed drops by employing various types of body accelerations, ranging from $1 - 2500\ g$, including those during takeoff, collision with the ground, and a flutter-type wingbeat. These low amplitude, flutter-type wingbeats are executed at more than double the mosquitoes' in-flight wingbeat frequency to dispel droplets. Table 6 gives a comparison of the survival mechanisms and associated accelerations mosquitoes employ when encountering different type of water particles. In addition to undiscovered drying techniques, our study raises questions of wetting, namely, if insect hair arrays are optimized to repel water. While micro-pillar wetting models exist[49], future researchers may choose to search for an optimum hair spacing, diameter, length, and stiffness, such that arrays easily repel drops of any length-scale.

Table 6: Methods for droplet removal, categorized by particle type.

	Particle Diameter *D* (prior to deposition)	**% Body Weight of 2 dyne Mosquito**	**Survival Behavior/ Mechanism**	**Associated Acceleration (*g*)**
Rain	1 – 8 mm	100 – 5000	hyrdophobicity, passive rotation	50 – 300
Fog	0.3 – 10 μm	10^{-10} – 10^{-5}	rest in unfavorable conditions	----
Dew	~100 nm	----	rapid takeoff hard landings wing flutters	0.5 – 3 10 2500

In Chapter 8, we strayed away from the realm of insects into that of furry mammals. Mammals do not face the locomotive challenges of insects in particle environments, but water accumulation on their bodies remains a great danger. By rapidly oscillating their bodies, through a process similar to shivering, furry mammals can dry themselves within seconds. We used high-speed videography and fur particle tracking to characterize the shakes of 33 animals (16 animals species and 5 dog breeds), ranging over four orders of

magnitude in mass from mice to bears. We presented a power-law relationship between shaking frequency f and body mass M to be $f \sim M^{-0.22}$, which is close to our prediction of $f \sim M^{-0.19}$ based upon the balance of centrifugal and capillary forces. We also observed a novel role for loose mammalian dermal tissue: by whipping around the body, it increases the speed of drops leaving the animal and the ensuing dryness relative to tight dermal tissue. Due to water absorption into the hair fibers themselves, an animal can remove about 70% of the water initially trapped in its fur, which can be done in less than 2 seconds. Therefore, we proposed that mammals shake close to an energetically optimal speed and time.

Much may be gleaned from nature's solutions to environmental challenges, as engineers become more interested in the manufacture of micro- and nanoscale devices which operate at scales dominated by capillary forces. Aerial robots have rapidly shrunken in size in recent years[1–7]. Their designs have closely relied on the physiology of insects. Biomimetics, the development of machines based on living organisms, is drawing on increasingly lightweight materials, but with smaller components, comes increased vulnerability to fluids. The success of robotics in the future will rely heavily on their ability to cope with challengingly wet and particle-filled environments.

It is my hope this series of investigations bestows perspicuity to a number of fundamental fluid mechanics problems arising through the consideration of flying insects, to date left largely unexplored by fluid dynamicists and biologists. In this thesis, we have applied modern technology (specifically, high-speed videography) and classical fluid mechanics towards understanding survival strategies of insects and mammals against surface tension forces and droplet impacts, which evolved millions of years ago.

APPENDIX A

SUPPLEMENTARY VIDEO CAPTIONS

A thesis is meant to stand the test of time, and the links below will remain active as long as YouTube exists.

Mosquitoes survive raindrop collisions by virtue of their low mass

Video S1: Experimental clips of mosquitoes and insect mimics, submitted to the Gallery of Fluid Motion, APS DFD 2011.

http://youtu.be/LQ88ny09ruM

Raindrops push and splash flying insects

Video S2: Experimental clips of all regions of impact on insects and insect mimics.

http://youtu.be/aBNPKej-lgU

Fog disables mosquito flight due to increased aerodynamic drag on halteres

Video S3: Mosquito taking off in a dense fog stream. The mosquito, unable to sense this orientation, quickly pitches forward after takeoff. Notice that despite the presence of fog and the deposition of droplets onto the body, a mosquito is able to generate lift in the presence of fog particles. Mosquitoes have been known to double their body weight through feeding and fly successfully. Time is slowed 150X.

http://youtu.be/6ZzGE_IM2qE

Video S4: Mosquito flying into the fog stream. The mosquito is performing normal flight

prior to entering the stream, but eventually perfumes a 180° roll due to interaction with the stream. Time is slowed 30X.

http://youtu.be/VS962PyCsFg

Video S5: Mosquito entering a container of hyperdense air from the top, unable to achieve flight before hitting the floor. Mosquitoes are able to climb in during brief periods but lack of orientation control results in a quick descent. Time is slowed 50X.

http://youtu.be/UTc_Y_F9gEw

Video S6: Haltere of a freshly dead mosquito manually plucked. The haltere has not been weighted with glue. Time is slowed 200X.

http://youtu.be/DhtvsC4996I

Video S7: Housefly successfully executing a turn in a fog stream. Unlike mosquitoes, houseflies could stay aloft in the densest fog tested. Time is slowed 140X.

http://youtu.be/4qq4TK7noag

Dew-driven folding of insect wings

Video S8: Top view of mosquito wing folding following coalescence cascade. Slowed 50X.

http://youtu.be/snqMbD5l-ks

Video S9: Drosophila melanogaster wing folding. Slowed 100X.

http://youtu.be/b2ZpuWm_LVc

Video S10: Mosquito wing folding tightly as drop above evaporates. Sped up 4X.

http://youtu.be/KXzpdwRYXac

Video S11: Mosquito wing reopening as drop above evaporates. Sped up 4X.

http://youtu.be/JTIb2nVjcaI

Mosquito drop shedding mechanisms for fog and dew deposition

Video S12: Live mosquito falls motionless to remove droplets covering its body. Mosquito quickly stands after fall and flies away. **http://youtu.be/8s1_f9fyjME**

Video S13: Mosquito flapping with a flutter stroke at 875 Hz (initially). This is a mechanism to remove small droplet attached to the wings. **http://youtu.be/t1NC1Rw8ygw**

Wet mammals shake at tuned frequencies to dry

Video S14: Particle-tracking straw affixed to a Labrador retriever's back during four periods of shaking. The shaking is initiated by the dog's head. Note the looseness of the skin increases the amplitude of shaking, which for the skin is 90° from the vertical axis. Time is slowed 25 X.

http://youtu.be/ekXOf8Rc5EI

Video S15: Image shaking sequence for animals of increasing size (Mouse, Rat, Kunekune Pig,Labrador Retriever, Gulf Coast Sheep Brown Bear), including an X-ray video of rat shaking. Note smaller animals (mouse, rat) lift their front feet to increase their mobility during the shake. Animals of all sizes exploit their loose skin to increase shaking amplitude.

http://youtu.be/FYegFlZ3-o0

Video S16: Drop ejection from a hair clump on the "wet-dog simulator." Ejected drops shrink with increasing centrifugal acceleration and decreasing hair aggregation size. Note

the small drop radius compared to the clump size for this frequency of rotation corresponding to $R\omega^2/g = 14$. Laser light in background is used to track rotation. Time is slowed 50 X.

http://youtu.be/jEMNwm-CX2c

APPENDIX B

DEW-DRIVEN FOLDING OF INSECT WINGS: NUMERICAL CODE

Below we provide the numerical code for solving the implicit equations presented in Chapter 6. The code is run in Intel Fortran Compiler integrated with Microsoft Visual Studio. Code was authored by Xing Liu.

```
program main
 implicit  none
!===========interface=============
     interface
    !*********total***************
         function  total (x, y, z)
         implicit  none
         real (8)  ::  x, y, z
         real (8)  ::   total (6)
        end
         function   total_extra  (x, y, z)
         implicit  none
         real (8)  ::  x, y, z
         real (8)  ::   total_extra  (6)
        end
    end  interface

!===========initialization=============
    real (8), parameter  ::  E = 1.9e7,  thickness  = 0.9e-5
    real (8)  ::  Lec, d, temp(6),  constants (3),  breakpoint,  rate,   pz_initial1  ,   pz_initial2
    real (8),  allocatable   ::  inv_r (:),  inv_r2 (:),  area (:),  th (:),  pz (:),  alpha (:),  dist (:)
    integer (8)  ::  i, j, no, err, m

        i = 1
        j = 0
        no = 1e5
```

```
allocate ( inv_r (no), inv_r2 (no), area(no), th(no), pz(no), alpha(no), dist (no), stat =
    err )
    if ( err .ne. 0) stop ' allocation error !'

forall (j = 1:no) inv_r (j) = 0.2+(1-0.2)/(no-1)*(j-1)
forall (j = 1:no) inv_r2 (j) = 0.32+(1-0.32)/(no-1)*(j-1)

area = 0
th = 0
pz = 0
alpha = 0
temp = 0
rate = 0
        dist = 0
pz_initial1 = -2
pz_initial2 = -2

Lec = SQRT(E/12*(thickness**3)/0.073)
d = 6.7e-4/Lec

constants = [d, thickness , E]

print *, constants
m = 3
call output( constants , ' plotgraph / cons_al . dat ' , m)

!==========lambda initial1====================
breakpoint = 0.0 ! 1 correct
do while(abs( breakpoint ) . lt . 1e-5)
    temp = total (1/ inv_r (1) , d, pz_initial1 )
    breakpoint = temp(6)
    print *, ' lambda_initial1 ' , pz_initial1
    pz_initial1 = pz_initial1 + 0.1

end do
!==========lambda initial2====================
breakpoint = 0.0 ! 1 correct
do while(abs( breakpoint ) . lt . 1e-5)
```

```
            temp = total_extra (1/inv_r2(1), d, pz_initial2 )
            breakpoint = temp(6)
            print *, ' lambda_initial2 ', pz_initial2
            pz_initial2 = pz_initial2 + 0.1

        end do

        pz_initial1 = pz_initial1 - 0.1
        pz_initial2 = pz_initial2 - 0.1

!==========calculate everything==============
        breakpoint = 1.0
        pz(1) = pz_initial1
        do while (abs(breakpoint-1) .lt. 1e-5)

            temp = total (1/inv_r(i), d, pz(i))
            area(i) = temp(1)
            th(i) = temp(2)
            pz(i) = temp(4)
            alpha(i) = temp(3)
                dist(i) = temp(5)
            breakpoint = temp(6)
            rate = sin(alpha(i)+th(i))/inv_r(i)/d/(3+pz(i))*6
            print *, 'FIRST', i, rate, pz(i)
            i = i+1
            pz(i) = pz(i-1)
        end do

        call output(area(1:i-2),'plotgraph/area_nm.txt',i-2)
        call output(th(1:i-2),'plotgraph/thet_nm.txt',i-2)
        call output(pz(1:i-2),'plotgraph/lamb_nm.txt',i-2)
        call output(alpha(1:i-2),'plotgraph/alph_nm.txt',i-2)
            call output(dist(1:i-2),'plotgraph/dist_nm.txt',i-2)
        call output(inv_r(1:i-2),'plotgraph/invr_nm.txt',i-2)

!==========extra==================================
        area = 0
        th = 0
        pz = 0
```

```
        alpha = 0
        temp = 0
        rate = 0
                dist = 0
        i = 1

!==========calculate everything extra==============
        breakpoint = 1.0
        pz(1) = pz_initial2
        do while (abs(breakpoint-1) .lt. 1e-5)

            temp = total_extra (1/inv_r2(i), d, pz(i))
            area(i) = temp(1)
            th(i) = temp(2)
            pz(i) = temp(4)
            alpha(i) = temp(3)
                        dist(i) = temp(5)
            breakpoint = temp(6)
            rate = sin(alpha(i)+th(i))/inv_r2(i)/d/(3+pz(i))*6
            print *, 'SECOND', i, rate, pz(i)
            i = i+1
            pz(i) = pz(i-1)
        end do

        call output(area(1:i-2),'plotgraph/area_ex.txt',i-2)
        call output(th(1:i-2),'plotgraph/thet_ex.txt',i-2)
        call output(pz(1:i-2),'plotgraph/lamb_ex.txt',i-2)
        call output(alpha(1:i-2),'plotgraph/alph_ex.txt',i-2)
                call output(dist(1:i-2),'plotgraph/dist_ex.txt',i-2)
        call output(inv_r2(1:i-2),'plotgraph/invr_ex.txt',i-2)


end program

!=========function================
!**** total *******
function total(x, y, z)
implicit none
```

```
real(8) :: x, y, z, lambda, lambda2, err, dlbd, s(100000),ss(99999), phi(99999), theta, q1,
    q2, tt
real(8) :: dx(99999), dy(99999), xx(100000), yy(100000), Area, l
real(8) :: total(6), rate, pi
real(8), external :: phi_cal
integer(8) :: judge, step, j
!x r
!y d
!z lbd
    judge = 1
    lambda = z
    lambda2 = 0
    dlbd = 1
    step = 0
    total = 0
    phi = 0
    err = 1e-5
    theta = 0
    q1 = 0
    q2 = 0
    tt = 0
    xx = 0
    yy = 0
    dx = 0
    dy = 0
    Area = 0
    l = 0
    j = 1
    pi = 4.D0*datan(1.D0)
    forall (j = 1:100000) s(j) = (j-1)/99999.0

    ss = s(2:100000)

loop1: do while( dlbd .gt. err)

        phi = -y**3/48/x *ss *(ss**2+lambda*ss-3-2*lambda)
        l = sum(y/100000*cos(phi))
        tt = l/2/x
        if (abs(tt) .gt. 1) then
```

```
    judge = 0
    print *, 'First loop1'
    exit loop1

                    else
    theta = asin(tt)
end if

q1 = 6*sin(y**3/48 /x *(2+lambda)+theta)*x/y-3;

phi = -y**3/48/x *ss *(ss**2+q1*ss-3-2*q1)
l = sum(y/100000*cos(phi))
tt = l/2/x
if (abs(tt) .gt. 1) then
    judge = 0
    print *, 'First loop2'
    exit loop1

                    else
    theta = asin(tt)
end if

q2 = 6*sin(y**3/48 /x *(2+q1)+theta)*x/y-3;
dlbd = abs(q2-q1)

                    if(dlbd .lt. err) then
    lambda2 = q2
else
    lambda2 = lambda-(q1-lambda)**2/(q2-2*q1+lambda)
end if

dlbd = abs(lambda2-lambda)
step = step+1
lambda = lambda2

if(step .gt. 10000) then
                                    print *, 'First convengence
                                        error!', x, lambda
                                    judge = 0
```

```
                                                    exit loop1
        end if
    end do loop1

        phi = -y**3/48/x*ss*(ss**2+lambda*ss-3-2*lambda)
        l = sum(y/100000*cos(phi))
        tt = l/2/x
        if (abs(tt) .gt. 1) then
            judge = 0

        else
            theta = asin(tt)
        end if
    rate = sin(y**3/48/x*(2+lambda)+theta)*x/y/(3+lambda)*6

    if(judge .ne. 0) then
        j = 1
        phi = -y**3/48/x*ss*(ss**2+lambda*ss-3-2*lambda)
        dy = sin(phi)/99999
        dx = cos(phi)/99999

loop2:  do j = 1, 99999
            yy(j+1) = yy(j)+dy(j)
            xx(j+1) = xx(j)+dx(j)

            if(dy(j) .lt. 0) then
                print*, 'Geometric Error A!'
                judge = 0
                exit loop2
            elseif (xx(j+1) .lt. 0) then
                print*, 'Geometric Error B!'
                judge = 0
                exit loop2
            end if

        end do loop2

        if (judge .ne. 0) then
            yy = yy - yy(100000)
```

```
                Area = -sum(yy(1:99999)*dx)*2
                Area = Area*y*y/4+x*x*(theta- sin( theta )*cos( theta ));
                total = [Area, theta , y**3 /48 /x *(2+lambda), lambda, 1, 1]
            else
                total = 0

            end if
        else
            total = 0
        end if

    end function total

!**** total *******
function total_extra (x, y, z)
implicit none
    real (8) :: x, y, z, lambda, lambda2, err , dlbd, s(100000),ss(99999), phi(99999), theta , q1,
        q2, tt
    real (8) :: dx(99999), dy(99999), xx(100000), yy(100000), Area, l
    real (8) :: total_extra (6) , rate , pi
    real (8) , external :: phi_cal
    integer (8) :: judge, step , j
    !x r
    !y d
    !z lbd
        pi = 4.D0*datan(1.D0)
        judge = 1
        lambda = z
        lambda2 = 0
        dlbd = 1
        step = 0
        total_extra = 0
        phi = 0
        err = 1e-5
        theta = 0
        q1 = 0
        q2 = 0
        tt = 0
        xx = 0
```

```
yy = 0
dx = 0
dy = 0
Area = 0
l = 0

forall (j = 1:100000) s(j) = (j-1)/99999.0
ss = s(2:100000)

loop3: do while( dlbd .gt. err)

    phi = -y**3 /48 /x *ss *(ss**2+lambda*ss-3-2*lambda)
    l = sum(y/100000*cos(phi))
    tt = l/2/x
    if (abs(tt) .gt. 1) then
        judge = 0
        print *, 'Third loop1'
        exit loop3

    else
        theta = pi - asin(tt)
    end if

    q1 = 6*sin(y**3 /48 /x *(2+lambda)+theta)*x/y-3;

    phi = -y**3 /48 /x *ss *(ss**2+q1*ss-3-2*q1)
    l = sum(y/100000*cos(phi))
    tt = l/2/x
    if (abs(tt) .gt. 1) then
        judge = 0
        print *, 'Third loop2'
        exit loop3

    else
        theta = pi - asin(tt)
    end if

    q2 = 6*sin(y**3 /48 /x *(2+q1)+theta)*x/y-3;
    dlbd = abs(q2-q1)
```

```
        if(dlbd .lt. err) then
            lambda2 = q2
        else
            lambda2 = lambda-(q1-lambda)**2/(q2-2*q1+lambda)
        end if

        dlbd = abs(lambda2-lambda)
        step = step+1
        lambda = lambda2

        if(step .gt. 10000) then
            print *, 'Second convengence error!', x, lambda
            judge = 0
            exit loop3
        end if

    end do loop3

        phi = -y**3/48/x *ss *(ss**2+lambda*ss-3-2*lambda)
        l = sum(y/100000*cos(phi))
        tt = l/2/x
        if (abs(tt) .gt. 1) then
            judge = 0

        else
            theta = pi- asin(tt)
        end if
    rate = sin(y**3/48 /x *(2+lambda)+theta)*x/y/(3+lambda)*6

    if(judge .ne. 0) then
        j = 1
        phi = -y**3/48/x *ss *(ss**2+lambda*ss-3-2*lambda)
        dy = sin(phi)/99999
        dx = cos(phi)/99999

loop4:  do j = 1, 99999
            yy(j+1) = yy(j)+ dy(j)
            xx(j+1) = xx(j)+ dx(j)
```

```
            if (dy(j) . lt . 0) then
                print *, 'Geometric Error A!'
                judge = 0
                exit loop4
            elseif (xx(j+1) . lt . 0) then
                print *, 'Geometric Error B!'
                judge = 0
                exit loop4
            end if

        end do loop4

        if (judge .ne. 0) then
            yy = yy - yy(100000)
            Area = -sum(yy(1:99999)*dx)*2
            Area = Area*y*y/4+x*x*(theta- sin(theta)*cos(theta));
            total_extra = [Area, theta, y**3/48 /x *(2+lambda), lambda, 1, 1]
        else
            total_extra = 0

        end if
    else
        total_extra = 0
    end if

end function total_extra
!==================================================================
subroutine output(results, filename, M)
implicit none

integer (8) :: i_var, err, i, M
real (8) :: results (*)
character (21) :: filename

    open( unit = 111, &
          file = filename, &
          err = 100, &
          iostat = i_var, &
```

```
            access = 'sequential', &
            form   = 'formatted',  &
            status = 'replace', &
            action = 'readwrite', &
            position = 'rewind')

100 continue

    if(i_var .eq. 0) then
        print *, '"results.dat" opened!'
    else if(i_var .gt. 0) then
        print *, 'File openning error:', i_var
        stop
    else
        print *, 'Reach to the end of file "results.dat"!'
        stop
    end if

    i = 0

    do i = 1, M-1
        write(111, 400) results(i), char(9)
    end do
        write(111, 300) results(M), char(9)

    endfile(111)
    print *, filename

300 format(f18.8,a)
400 format(f18.8,a\)
500 format(/i0,a,i0,a,i0)

    close(111)
end subroutine output
```

APPENDIX C

SCHOLARLY ACHIEVEMENTS

C.1 Journal papers

Dickerson, A.K. and Shankles, P.G. and Madhavan, N.M. and Hu, D.L. "Mosquitoes survive raindrop collisions by virtue of their low mass," *Proceedings of the National Academy of Sciences*. 109, no. 25, 2011.

Dickerson, A.K. and Mills, Z.G. and Hu, D.L. "Wet mammals shake at tuned frequencies to dry," *Journal of the Royal Society Interface*. 10.1098, 2012.

Dickerson, A.K. and Shankles, P.G., and Hu, D.L. "Raindrops push and splash flying insects," *Physics of Fluids*. (In Review)

Dickerson, A.K. and Shankles, P.G. and Berry, B.E. and Hu, D.L. "Fog disrupts mosquito flight due to increased aerodynamic drag on halteres," *Experiments in Fluids*. (In Review)

Dickerson A.K. and Liu, X. and Zhu, T. and Hu, D.L. "Dew driven folding of insect wings." *Journal of the Royal Society Interface*. (In Preparation)

Dickerson A.K. and Hu, D.L. "Mosquitoes actively remove drops deposited by fog and dew," *Integrative and Comparative Biology*. (In Review)

C.2 Conference presentations

Dickerson, A.K. and Mills, Z.G. and Hu, D.L. "Wet-dog shake" American Physical Society: Division of Fluid Dynamics. Nov 2010. Long Beach, CA

Dickerson, A.K. and Shankles, P.G. and Madhavan, N.M. and Hu, D.L. "How mosquitoes fly in the rain," American Physical Society: Division of Fluid Dynamics. Nov 2011. Baltimore, MD

Dickerson, A.K. and Shankles, P.G. and Madhavan, N.M. and Hu, D.L. "Insects flying in the rain," Society for Integrative and Comparative Biology. Jan 2012. Charleston, SC

Dickerson, A.K. and Telljohann, L. and Hu, D.L. "Mosquito flight failure in heavy fog," American Physical Society: Division of Fluid Dynamics. Nov 2012. San Diego, CA

Dickerson, A.K. and Liu, X. and Zhu, T. and Hu, D.L. "Dew-driven folding of insect wings," American Physical Society: Division of Fluid Dynamics. Nov 2013. Pittsburgh, PA

Bibliography

[1] DENG, X., SCHENATO, L., WU, W., and SASTRY, S., "Flapping flight for biomimetic robotic insects: Part I-System modeling," *Robotics, IEEE Transactions on*, vol. 22, no. 4, pp. 776–788, 2006.

[2] WOOD, R., "The first takeoff of a biologically inspired at-scale robotic insect," *IEEE Transactions on Robotics*, vol. 24, no. 2, pp. 341–347, 2008.

[3] DE CROON, G., DE CLERCQ, K., RUIJSINK, R., REMES, B., and DE WAGTER, C., "Design, aerodynamics, and vision-based control of the DelFly," *International Journal of Micro Air Vehicles*, vol. 1, no. 2, pp. 71–97, 2009.

[4] RICHTER, C. and LIPSON, H., "Untethered hovering flapping flight of a 3D-printed mechanical insect," *Artificial Life*, vol. 17, no. 2, pp. 73–86, 2011.

[5] VAN BREUGEL, F., REGAN, W., and LIPSON, H., "From insects to machines," *Robotics & Automation Magazine, IEEE*, vol. 15, no. 4, pp. 68–74, 2008.

[6] VAN BREUGEL, F., TEOH, Z., and LIPSON, H., "A passively stable hovering flapping micro-air vehicle," *Flying Insects and Robots*, pp. 171–184, 2009.

[7] ZDUNICH, P., BILYK, D., MACMASTER, M., LOEWEN, D., DELAURIER, J., KORNBLUH, R., LOW, T., STANFORD, S., and HOLEMAN, D., "Development and testing of the mentor flapping-wing micro air vehicle," *Journal of Aircraft*, vol. 44, no. 5, pp. 1701–1711, 2007.

[8] WANG, Z., "Dissecting insect flight," *Annual Reviews of Fluid Mechanics*, vol. 37, pp. 183–210, 2005.

[9] DUDLEY, R., "Unsteady aerodynamics," *Science*, vol. 284, no. 5422, pp. 1937–1939, 1999.

[10] DUDLEY, R., *The biomechanics of insect flight: form, function, evolution*. Princeton Univ. Press, 2002.

[11] TAYLOR, C. and HEGLUND, N., "Energetics and mechanics of terrestrial locomotion," *Annual review of physiology*, vol. 44, no. 1, pp. 97–107, 1982.

[12] RISTROPH, L., BERGOU, A., RISTROPH, G., COUMES, K., BERMAN, G., GUCKENHEIMER, J., WANG, Z., and COHEN, I., "Discovering the flight autostabilizer of fruit flies by inducing aerial stumbles," *Proceedings of the National Academy of Sciences*, vol. 107, no. 11, pp. 4820–4824, 2010.

[13] KHASNIS, A. and NETTLEMAN, M., "Global warming and infectious disease," *Archives of Medical Research*, vol. 36, no. 6, pp. 689–696, 2005.

[14] AMADOR, G. J., YAMADA, Y., MCCURLEY, M., and HU, D. L., "Splash-cup plants accelerate raindrops to disperse seeds," *Journal of The Royal Society Interface*, vol. 10, no. 79, 2013.

[15] ATTENBOROUGH, D., "Life in the undergrowth," BBC, 2005.

[16] REYSSAT, E., CHEVY, F., BIANCE, A.-L., PETITJEAN, L., and QUÉRÉ, D., "Shape and instability of free-falling liquid globules," *Europhysics Letters*, vol. 80, no. 3, p. 34005, 2007.

[17] VOIGT, C., SCHNEEBERGER, K., VOIGT-HEUCKE, S., and LEWANZIK, D., "Rain increases the energy cost of bat flight," *Biology letters*, vol. 7, no. 5, pp. 793–795, 2011.

[18] ORTEGA-JIMENEZ, V. and DUDLEY, R., "Aerial shaking performance of wet anna's hummingbirds," *Journal of The Royal Society Interface*, 2011.

[19] COMBES, S. and DUDLEY, R., "Turbulence-driven instabilities limit insect flight performance," *Proceedings of the National Academy of Sciences*, vol. 106, no. 22, pp. 9105–9108, 2009.

[20] RISTROPH, L., BERMAN, G., BERGOU, A., WANG, Z., and COHEN, I., "Automated hull reconstruction motion tracking (hrmt) applied to sideways maneuvers of free-flying insects," *Journal of Experimental Biology*, vol. 212, no. 9, pp. 1324–1335, 2009.

[21] HEDRICK, T., CHENG, B., and DENG, X., "Wingbeat time and the scaling of passive rotational damping in flapping flight," *Science*, vol. 324, no. 5924, pp. 252–255, 2009.

[22] DICKINSON, M., LEHMANN, F., and SANE, S., "Wing rotation and the aerodynamic basis of insect flight," *Science*, vol. 284, no. 5422, pp. 1954–1960, 1999.

[23] DANIEL, T. and COMBES, S., "Flexible wings and fins: Bending by inertial or fluid-dynamic forces?," *Integrative and Comparative Biology*, vol. 42, no. 5, pp. 1044–1049, 2002.

[24] PHILLIPS, E., "Nasa will study heavy rain effects on wing aerodynamics.," *Aviation Week and Space Technology*, vol. 130, no. 7, pp. 38–41, 1989.

[25] BEZOS, G., AERONAUTICS, U. S. N., SCIENTIFIC, S. A., and PROGRAM, T. I., *Wind tunnel aerodynamic characteristics of a transport-type airfoil in a simulated heavy rain environment*. Citeseer, 1992.

[26] WAN, T. and WU, S., "Aerodynamic analysis under influence of heavy rain," *Journal of Aeronautics, Astronautics, and Aviation*, pp. 173–180, 2004.

[27] BUSH, J., HU, D., and PRAKASH, M., "The integument of water-walking arthropods: form and function," *Advances in Insect Physiology*, vol. 34, pp. 117–192, 2007.

[28] VILLERMAUX, E., BOSSA, B., and OTHERS, "Drop fragmentation on impact," *Journal of Fluid Mechanics*, vol. 668, pp. 412–435, 2011.

[29] YARIN, A., "Drop impact dynamics: splashing, spreading, receding, bouncing...," *Annual Review of Fluid Mechanics*, vol. 38, pp. 159–192, 2006.

[30] JIANG, Y., UMEMURA, A., and LAW, C., "An experimental investigation on the collision behaviour of hydrocarbon droplets," *Journal of Fluid Mechanics*, vol. 234, no. -1, pp. 171–190, 1992.

[31] ORME, M., "Experiments on droplet collisions, bounce, coalescence and disruption," *Progress in Energy and Combustion Science*, vol. 23, pp. 65–79, 1997.

[32] REIN, M., "Phenomena of liquid drop impact on solid and liquid surfaces," *Fluid Dynamics Research*, vol. 12, no. 2, pp. 61–93, 1993.

[33] FIELD, J., DEAR, J., and OGREN, J., "The effects of target compliance on liquid drop impact," *Journal of Applied Physics*, vol. 65, no. 2, pp. 533–540, 1989.

[34] BAKSHI, S., ROISMAN, I., and TROPEA, C., "Investigations on the impact of a drop onto a small spherical target," *Physics of Fluids*, vol. 19, 2007.

[35] ROZHKOV, A., PRUNET-FOCH, B., and VIGNES-ADLER, M., "Dynamics of a liquid lamella resulting from the impact of a water drop on a small target," *Proceedings of the Royal Society of London. Series A: Mathematical, Physical and Engineering Sciences*, vol. 460, no. 2049, p. 2681, 2004.

[36] ROZHKOV, A., PRUNET-FOCH, B., and VIGNES-ADLER, M., "Impact of water drops on small targets," *Physics of Fluids*, vol. 14, p. 3485, 2002.

[37] BUSSMANN, M., MOSTAGHIMI, J., and CHANDRA, S., "On a three-dimensional volume tracking model of droplet impact," *Physics of Fluids*, vol. 11, p. 1406, 1999.

[38] CHANDRA, S. and AVEDISIAN, C., "On the collision of a droplet with a solid surface," *Proceedings: Mathematical and Physical Sciences*, vol. 432, no. 1884, pp. 13–41, 1991.

[39] DE GENNES, P., BROCHARD-WYART, F., and QUÉRÉ, D., *Capillarity and wetting phenomena: drops, bubbles, pearls, waves*. Springer Verlag, 2004.

[40] QUÉRÉ, D., "Wetting and roughness," *Annual Reviews of Materials Research*, vol. 38, pp. 71–99, 2008.

[41] BARTHLOTT, W. and NEINHUIS, C., "Purity of the sacred lotus, or escape from contamination in biological surfaces," *Planta*, vol. 202, no. 1, pp. 1–8, 1997.

[42] PAL, R., "The wetting of insect cuticle," *Bulletin of Entomological Research*, vol. 41, no. 01, pp. 121–139, 1950.

[43] WAGNER, T., NEINHUIS, C., and BARTHLOTT, W., "Wettability and contaminability of insect wings as a function of their surface sculptures," *Acta Zoologica*, vol. 77, no. 3, pp. 213–225, 1996.

[44] NGUYEN, S. H. T., WEBB, H. K., HASAN, J., TOBIN, M. J., CRAWFORD, R. J., and IVANOVA, E. P., "Dual role of outer epicuticular lipids in determining the wettability of dragonfly wings," *Colloids and Surfaces B: Biointerfaces*, vol. 106, pp. 126–134, 2013.

[45] WATSON, G. S., WATSON, J. A., HU, S., BROWN, C. L., CRIBB, B., and MYHRA, S., "Micro and nanostructures found on insect wings–designs for minimising adhesion and friction," *International Journal of Nanomanufacturing*, vol. 5, no. 1, pp. 112–128, 2010.

[46] BYUN, D., HONG, J., SAPUTRA, KO, J., LEE, Y., PARK, H., BYUN, B., and LUKES, J., "Wetting characteristics of insect wing surfaces," *Journal of Bionic Engineering*, vol. 6, no. 1, pp. 63–70, 2009.

[47] SUN, M., WATSON, G. S., ZHENG, Y., WATSON, J. A., and LIANG, A., "Wetting properties on nanostructured surfaces of cicada wings," *Journal of Experimental Biology*, vol. 212, no. 19, pp. 3148–3155, 2009.

[48] JOPP, J., GRÜLL, H., and YERUSHALMI-ROZEN, R., "Wetting behavior of water droplets on hydrophobic microtextures of comparable size," *Langmuir*, vol. 20, no. 23, pp. 10015–10019, 2004.

[49] YU, T., PARK, J., LIM, H., and BREUER, K., "Fog deposition and accumulation on smooth and textured hydrophobic surfaces," *Langmuir*, vol. 28, no. 35, pp. 12771–12778, 2012.

[50] DORRER, C. and RÜHE, J., "Condensation and wetting transitions on microstructured ultrahydrophobic surfaces," *Langmuir*, vol. 23, no. 7, pp. 3820–3824, 2007.

[51] DING, Y., XU, S., ZHANG, Y., WANG, A. C., WANG, M. H., XIU, Y., WONG, C. P., and WANG, Z. L., "Modifying the anti-wetting property of butterfly wings and water strider legs by atomic layer deposition coating: surface materials versus geometry," *Nanotechnology*, vol. 19, no. 35, 2008.

[52] HU, D. L., CHAN, B., and BUSH, J. W. M., "The hydrodynamics of water strider locomotion," *Nature*, vol. 424, pp. 663–666, 2003.

[53] GAO, X. and JIANG, L., "Biophysics: Water-repellent legs of water striders," *Nature*, vol. 432, no. 7013, pp. 36–36, 2004.

[54] ZHENG, Y., GAO, X., and JIANG, L., "Directional adhesion of superhydrophobic butterfly wings," *Soft Matter*, vol. 3, no. 2, pp. 178–182, 2007.

[55] VOGELMANN, H., "Fog precipitation in the cloud forests of eastern mexico," *Bioscience*, vol. 23, no. 2, pp. 96–100, 1973.

[56] KOSTER, F., "Darwin's finch "ploughs" for water," *Noticias de Galapagos*, vol. 41, pp. 23–24, 1985.

[57] SEELY, M., "Irregular fog as a water source for desert dune beetles," *Oecologia*, vol. 42, no. 2, pp. 213–227, 1979.

[58] ANDRADE, J., "Dew deposition on epiphytic bromeliad leaves: an important event in a Mexican tropical dry deciduous forest," *Journal of Tropical Ecology*, vol. 19, no. 5, pp. 479–488, 2003.

[59] PINNICK, R., HOIHJELLE, D., FERNANDEZ, G., STENMARK, E., LINDBERG, J., HOIDALE, G., and JENNINGS, S., "Vertical structure in atmospheric fog and haze and its effects on visible and infrared extinction," *Journal of the Atmospheric Sciences*, vol. 35, no. 10, pp. 2020–2032, 1978.

[60] GULTEPE, I., PEARSON, G., MILBRANDT, J., HANSEN, B., PLATNICK, S., TAYLOR, P., GORDON, M., OAKLEY, J., and COBER, S., "The fog remote sensing and modeling field project," *Bulletin of the American Meteorological Society*, vol. 90, no. 3, pp. 341–359, 2009.

[61] SINCLAIR, D. and LA MER, V., "Light scattering as a measure of particle size in aerosols. the production of monodisperse aerosols.," *Chemical Reviews*, vol. 44, no. 2, pp. 245–267, 1949.

[62] THOMPSON, B., WARD, J., and ZINKY, W., "Application of hologram techniques for particle size analysis," *Applied optics*, vol. 6, no. 3, pp. 519–526, 1967.

[63] SEIBER, J., WILSON, B., and MCCHESNEY, M., "Air and fog deposition residues of four organophosphate insecticides used on dormant orchards in the san joaquin valley, california," *Environmental Science & Technology*, vol. 27, no. 10, pp. 2236–2243, 1993.

[64] SUTER, R., STRATTON, G., and MILLER, P., "Taxonomic variation among spiders in the ability to repel water: surface adhesion and hair density," *Journal of Arachnology*, pp. 11–21, 2004.

[65] BEVANGER, K., "Bird interactions with utility structures: collision and electrocution, causes and mitigating measures," *Ibis*, vol. 136, no. 4, pp. 412–425, 1994.

[66] BENDER, J. and DICKINSON, M., "A comparison of visual and haltere-mediated feedback in the control of body saccades in drosophila melanogaster," *Journal of Experimental Biology*, vol. 209, no. 23, pp. 4597–4606, 2006.

[67] GÖTZ, K., "Flight control in drosophila by visual perception of motion," *Biological Cybernetics*, vol. 4, no. 6, pp. 199–208, 1968.

[68] CHENG, B., DENG, X., and HEDRICK, T., "The mechanics and control of pitching manoeuvres in a freely flying hawkmoth (manduca sexta)," *The Journal of Experimental Biology*, vol. 214, no. 24, pp. 4092–4106, 2011.

[69] ARBAS, E., "Control of hindlimb posture by wind-sensitive hairs and antennae during locust flight," *Journal of Comparative Physiology A: Neuroethology, Sensory, Neural, and Behavioral Physiology*, vol. 159, no. 6, pp. 849–857, 1986.

[70] NIEHAUS, M., "Flight and flight control by the antennae in the small tortoiseshell (aglais urticae l., lepidoptera)," *Journal of Comparative Physiology A: Neuroethology, Sensory, Neural, and Behavioral Physiology*, vol. 145, no. 2, pp. 257–264, 1981.

[71] GEWECKE, M. and NIEHAUS, M., "Flight and flight control by the antennae in the small tortoiseshell (aglais urticae l., lepidoptera)," *Journal of Comparative Physiology A: Neuroethology, Sensory, Neural, and Behavioral Physiology*, vol. 145, no. 2, pp. 249–256, 1981.

[72] SANE, S., DIEUDONNÉ, A., WILLIS, M., and DANIEL, T., "Antennal mechanosensors mediate flight control in moths," *Science Signalling*, vol. 315, no. 5813, p. 863, 2007.

[73] SUTCLIFFE, J. F., "Sensory bases of attractancy: morphology of mosquito olfactory sensilla–a review.," *Journal of the American Mosquito Control Association*, vol. 10, p. 309, 1994.

[74] BÖRÖCZKY, K., WADA-KATSUMATA, A., BATCHELOR, D., ZHUKOVSKAYA, M., and SCHAL, C., "Insects groom their antennae to enhance olfactory acuity," *Proceedings of the National Academy of Sciences*, vol. 110, no. 9, pp. 3615–3620, 2013.

[75] FRAENKEL, G. and PRINGLE, J., "Biological sciences: Halteres of flies as gyroscopic organs of equilibrium," *Nature*, vol. 141, pp. 919–920, 1938.

[76] WU, W., WOOD, R., and FEARING, R., "Halteres for the micromechanical flying insect," in *Robotics and Automation, 2002. Proceedings. ICRA'02. IEEE International Conference on*, vol. 1, pp. 60–65, IEEE, 2002.

[77] DICKINSON, M., "Come fly with me," *Engineering and Science*, vol. 66, no. 3, pp. 10–19, 2003.

[78] BARTUSSEK, J., MUTLU, A. K., ZAPOTOCKY, M., and FRY, S. N., "Limit-cycle-based control of the myogenic wingbeat rhythm in the fruit fly drosophila," *Journal of The Royal Society Interface*, vol. 10, no. 80, 2013.

[79] SANE, S. P. and MCHENRY, M. J., "The biomechanics of sensory organs," *Integrative and Comparative Biology*, vol. 49, no. 6, pp. i8–i23, 2009.

[80] SELLKE, K. and OTHERS, "Biological and morphological studies on harmful tipulids.," *Zeitschrift fur wissenschaftliche Zoologie*, vol. 148, no. 4, pp. 465–555, 1936.

[81] PRINGLE, J., "The gyroscopic mechanism of the halteres of diptera," *Philosophical Transactions of the Royal Society of London. Series B, Biological Sciences*, pp. 347–384, 1948.

[82] HEIDE, G., "Neural mechanisms of flight control in diptera," *Biona-report*, vol. 2, pp. 35–52, 1983.

[83] FAYYAZUDDIN, A. and DICKINSON, M., "Convergent mechanosensory input structures the firing phase of a steering motor neuron in the blowfly, calliphora," *Journal of Neurophysiology*, vol. 82, no. 4, pp. 1916–1926, 1999.

[84] BONCHEVA, M., BRUZEWICZ, D. A., WHITESIDES, G. M., and OTHERS, "Millimeter-scale self-assembly and its applications," *Pure and Applied Chemistry*, vol. 75, no. 5, pp. 621–630, 2003.

[85] KOBAYASHI, H., KRESLING, B., and VINCENT, J. F., "The geometry of unfolding tree leaves," *Proceedings of the Royal Society of London. Series B: Biological Sciences*, vol. 265, no. 1391, pp. 147–154, 1998.

[86] FREITAS, L. and SAZIMA, M., "Daily blooming pattern and pollination by syrphids in sisyrinchium vaginatum (iridaceae) in southeastern brazil," *Journal of the Torrey Botanical Society*, pp. 55–61, 2003.

[87] FORBES, W. M., "How a beetle folds its wings," *Psyche*, vol. 31, no. 6, pp. 254–258, 1924.

[88] HAAS, F. and BEUTEL, R. G., "Wing folding and the functional morphology of the wing base in coleoptera," *Zoology*, vol. 104, no. 2, pp. 123–141, 2001.

[89] MOUNTCASTLE, A. M. and COMBES, S. A., "Wing flexibility enhances load-lifting capacity in bumblebees," *Proceedings of the Royal Society B: Biological Sciences*, vol. 280, no. 1759, 2013.

[90] GOSLINE, J., LILLIE, M., CARRINGTON, E., GUERETTE, P., ORTLEPP, C., and SAVAGE, K., "Elastic proteins: biological roles and mechanical properties," *Philosophical Transactions of the Royal Society of London. Series B: Biological Sciences*, vol. 357, no. 1418, pp. 121–132, 2002.

[91] LEHMANN, F.-O., GORB, S., NASIR, N., and SCHÜTZNER, P., "Elastic deformation and energy loss of flapping fly wings," *The Journal of Experimental Biology*, vol. 214, no. 17, pp. 2949–2961, 2011.

[92] GORB, S. N., "Serial elastic elements in the damselfly wing: mobile vein joints contain resilin," *Naturwissenschaften*, vol. 86, no. 11, pp. 552–555, 1999.

[93] COMBES, S. and DANIEL, T., "Flexural stiffness in insect wings ii. spatial distribution and dynamic wing bending," *Journal of Experimental Biology*, vol. 206, no. 17, pp. 2989–2997, 2003.

[94] KESEL, A. B., PHILIPPI, U., and NACHTIGALL, W., "Biomechanical aspects of the insect wing: an analysis using the finite element method," *Computers in Biology and Medicine*, vol. 28, no. 4, pp. 423–437, 1998.

[95] COMBES, S. and DANIEL, T., "Flexural stiffness in insect wings i. scaling and the influence of wing venation," *Journal of Experimental Biology*, vol. 206, no. 17, pp. 2979–2987, 2003.

[96] NEUKIRCH, S., ANTKOWIAK, A., and MARIGO, J.-J., "The bending of an elastic beam by a liquid drop: A variational approach," *Proceedings of the Royal Society A: Mathematical, Physical and Engineering Science*, 2013.

[97] PY, C., REVERDY, P., DOPPLER, L., BICO, J., ROMAN, B., and BAROUD, C., "Capillary origami: spontaneous wrapping of a droplet with an elastic sheet," *Physical Review Letters*, vol. 98, no. 15, p. 156103, 2007.

[98] HONSCHOTEN, J., BERENSCHOT, J., SANDERS, R., ABELMANN, L., TAS, N., and ELWENSPOEK, M., "Fabrication of three-dimensional microstructures using capillary forces," *The 20th Micromechanics Europe Workshop*, 2009.

[99] JUNG, S., REIS, P., JAMES, J., CLANET, C., and BUSH, J., "Capillary origami in nature," *Physics of Fluids*, vol. 21, pp. 91–110, 2009.

[100] BICO, J., ROMAN, B., MOULIN, L., and BOUDAOUD, A., "Adhesion: Elastocapillary coalescence in wet hair," *Nature*, vol. 432, no. 7018, p. 690, 2004.

[101] NEINHUIS, C. and BARTHLOTT, W., "Characterization and distribution of water-repellent, self-cleaning plant surfaces," *Annals of Botany*, vol. 79, no. 6, p. 667, 1997.

[102] BUSH, J. W. M., HU, D. L., and PRAKASH, M., "The Integument of Water-walking Arthropods: Form and Function," *Insect Mechanics and Control: Advances in Insect Physiology*, vol. 176, pp. 117–192, 2007.

[103] TIMACHEFF, S., *Canon EOS digital photography photo workshop*. Wiley Publishing Inc. Indianapolis, Indiana, 2008.

[104] FERRI, F., SMITH, P., LEMMON, M., and RENNÓ, N., "Dust devils as observed by Mars Pathfinder," *J. Geophys. Res*, vol. 108, no. 7, pp. 1–7, 2003.

[105] VAN ROOIJEN, J., "Dust bathing and other comfort behaviours of domestic hens," Animal Management, pp. 110–123, Internationale Gesellschaft fŭr Nutztierhaltung, 2005.

[106] SOKOLOV, V., *Mammal Skin*. Univ of California Press. Berkeley, CA., 1982.

[107] ROMANENKO, E. and SOKOLOV, V., "Wettability of the coat of the northern fur seal," *Doklady Akademii Nauk SSSR*, vol. 297, pp. 990–994, 1987.

[108] FISH, F., SMELSTOYS, J., BAUDINETTE, R., and REYNOLDS, P., "Fur does not fly, it floats: buoyancy of pelage in semi-aquatic mammals," *Aquatic Mammals*, vol. 28, no. 2, pp. 103–112, 2002.

[109] WEISEL, J., NAGASWAMI, C., and PETERSON, R., "River otter hair structure facilitates interlocking to impede penetration of water and allow trapping of air," *Canadian Journal of Zoology*, vol. 83, no. 5, pp. 649–655, 2005.

[110] SPRUIJT, B., VAN HOOFF, J., and GISPEN, W., "Ethology and neurobiology of grooming behavior," *Physiological Reviews*, vol. 72, no. 3, p. 825, 1992.

[111] HALDANE, J., "On being the right size," *The World of Mathematics*, vol. 2, pp. 952–957, 1956.

[112] SANTORI, R., VIEIRA, M., ROCHA-BARBOSA, O., MAGNAN-NETO, J., and GOBBI, N., "Water Absorption of the Fur and Swimming Behavior of Semiaquatic and Terrestrial Oryzomine Rodents," *Journal Information*, vol. 89, no. 5, 2008.

[113] KORHONEN, H. and NIEMELA, P., "Water absorption and the drying and cooling rates in mink (Mustela vison) following simulated diving," *Animal Science*, vol. 74, no. 2, pp. 277–284, 2002.

[114] WEBB, D. and KING, J., "Effects of wetting of insulation of bird and mammal coats," *Journal of Thermal Biology*, vol. 9, no. 3, pp. 189–191, 1984.

[115] BAKKEN, G., "A heat transfer analysis of animals: Unifying concepts and the application of metabolism chamber data to field ecology," *Journal of Theoretical Biology*, vol. 60, no. 2, pp. 337–384, 1976.

[116] SCHMIDT-NIELSEN, K., *Animal Physiology: Adaptation and Environment*. Cambridge Univ Pr, 5 ed., 1997.

[117] DICKERSON, A., SHANKLES, P., MADHAVAN, N., and HU, D., "Mosquitoes survive raindrop collisions by virtue of their low mass," *Proceedings of the National Academy of Sciences*, vol. 109, no. 25, pp. 9822–9827, 2012.

[118] DICKERSON, A., SHANKLES, P., and HU, D., "Raindrops push and splash flying insects," *Physics of Fluids (under review)*, 2013.

[119] DICKERSON, A., SHANKLES, P., BERRY, B., and HU, D., "Fog disrupts mosquito flight due to increased aerodynamic drag on halteres," *Experiments in Fluids (under review)*, 2014.

[120] DICKERSON, A., LIU, X., ZHU, T., and HU, D., "Dew driven folding of insect wings," *Physical Review Letters (to be submitted)*, 2014.

[121] DICKERSON, A. and HU, D., "Mosquito coping mechanisms for fog and dew deposition," *Integrative and Comparative Biology*, 2014.

[122] DICKERSON, A., MILLS, Z., and HU, D., "Wet mammals shake at tuned frequencies to dry," *Journal of The Royal Society Interface*, vol. 9, no. 77, pp. 3208–3218, 2012.

[123] WEIS-FOGH, T., "Quick estimates of flight fitness in hovering animals, including novel mechanisms for lift production," *Journal of Experimental Biology*, vol. 59, no. 1, pp. 169–230, 1973.

[124] ENNOS, A. R., "The kinematics and aerodynamics of the free flight of some Diptera," *Journal of Experimental Biology*, vol. 142, no. 1, pp. 49–85, 1989.

[125] FRY, S. N., SAYAMAN, R., and DICKINSON, M. H., "The aerodynamics of hovering flight in Drosophila," *Journal of Experimental Biology*, vol. 208, no. 12, pp. 2303–2318, 2005.

[126] ELLINGTON, C., "The aerodynamics of hovering insect flight. III. Kinematics," *Philosophical Transactions of the Royal Society of London. Series B, Biological Sciences*, pp. 41–78, 1984.

[127] ELLINGTON, C., "The aerodynamics of hovering insect flight. ii. morphological parameters," *Philosophical Transactions of the Royal Society of London. Series B, Biological Sciences*, pp. 17–40, 1984.

[128] LIU, Y. and SUN, M., "Wing kinematics measurement and aerodynamics of hovering droneflies," *Journal of Experimental Biology*, vol. 211, no. 13, pp. 2014–2025, 2008.

[129] DUDLEY, R., "Extraordinary flight performance of orchid bees (apidae: Euglossini) hovering in heliox (80% he/20% o2)," *Journal of experimental biology*, vol. 198, no. 4, pp. 1065–1070, 1995.

[130] DUDLEY, R. and ELLINGTON, C., "Mechanics of forward flight in bumblebees: I. Kinematics and morphology," *Journal of Experimental Biology*, vol. 148, no. 1, pp. 19–52, 1990.

[131] WILLMOTT, A. P. and ELLINGTON, C. P., "The mechanics of flight in the hawkmoth manduca sexta. ii. aerodynamic consequences of kinematic and morphological variation.," *Journal of Experimental Biology*, vol. 200, no. 21, pp. 2723–2745, 1997.

[132] WILLMOTT, A. P. and ELLINGTON, C. P., "The mechanics of flight in the hawkmoth manduca sexta. i. kinematics of hovering and forward flight.," *Journal of Experimental Biology*, vol. 200, no. 21, pp. 2705–2722, 1997.

[133] CHAI, P. and MILLARD, D., "Flight and size constraints: hovering performance of large hummingbirds under maximal loading.," *Journal of Experimental Biology*, vol. 200, no. 21, pp. 2757–2763, 1997.

[134] ALEXANDER, D. and LIBRETTO, S., "An overview of the toxicology of hfa-134a (1, 1, 1, 2-tetrafluoroethane).," *Human& Experimental Toxicology*, vol. 14, no. 9, p. 715, 1995.

[135] ERASMUS, H., *Determination of Some Blood Parameters in the African Lion (Panthera Leo)*. PhD thesis, University of the Free State, 2008.

[136] STERNDALE, R., *Natural history of the Mammalia of India and Ceylon*. Thacker, Spink, and Co., Bombay, India, 1884.

[137] ROGERS, L., "Effects of mast and berry crop failures on survival, growth, and reproductive success of black bears," in *Transactions, Forty-First North American Wildlife and Natural Resources Conference, March 21-25, 1976, Washington, DC*, p. 431, 1976.

[138] SWENSON, J., SANDEGREN, F., and SO-DERBERG, A., "Geographic expansion of an increasing brown bear population: evidence for presaturation dispersal," *Journal of Animal Ecology*, vol. 67, no. 5, pp. 819–826, 1998.

[139] COSTELLO, C., JONES, D., INMAN, R., INMAN, K., THOMPSON, B., and QUIGLEY, H., "Relationship of variable mast production to american black bear reproductive parameters in new mexico," *Ursus*, pp. 1–16, 2003.

[140] BLANCHARD, B., "Size and growth patterns of the Yellowstone grizzly bear," *Bears: Their Biology and Management*, vol. 7, pp. 99–107, 1987.

[141] NAGY, J., KINGSLEY, M., RUSSELL, R., and PEARSON, A., "Relationship of weight to chest girth in the grizzly bear.," *Journal of Wildlife Management*, vol. 48, no. 4, pp. 1439–1440, 1984.

[142] KOPROWSKI, J., "Response of fox squirrels and gray squirrels to a late spring-early summer food shortage," *Journal of Mammalogy*, vol. 72, no. 2, pp. 367–372, 1991.

[143] BAUMAN, J. and CHANG, Y., "High-speed X-ray video demonstrates significant skin movement errors with standard optical kinematics during rat locomotion," *Journal of Neuroscience Methods*, vol. 186, no. 1, pp. 18–24, 2010.

[144] SAVILE, D. and HAYHOE, H., "The potential effect of drop size on efficiency of splash-cup and springboard dispersal devices," *Canadian Journal of Botany*, vol. 56, no. 1, pp. 127–128, 1978.

[145] GUNN, R. and KINZER, G., "The terminal velocity of fall for water droplets in stagnant air," *Journal of Atmospheric Sciences*, vol. 6, pp. 243–248, 1949.

[146] JEBSON, S., "Fact sheet no. 3: Water in the atmosphere," *National Meteorological Library and Archive*, 2007.

[147] YOUNG, H. and FREEDMAN, R., *University Physics*. Pearson Education Inc., 11 ed., 2004.

[148] CLANET, C., BÉGUIN, C., RICHARD, D., and QUÉRÉ, D., "Maximal deformation of an impacting drop," *Journal of Fluid Mechanics*, vol. 517, pp. 199–208, 2004.

[149] OKUMURA, K., CHEVY, F., RICHARD, D., QUÉRÉ, D., and CLANET, C., "Water spring: A model for bouncing drops," *EPL (Europhysics Letters)*, vol. 62, p. 237, 2003.

[150] GUNDERSON, S. and SCHIAVONE, R., "The insect exoskeleton: a natural structural composite," *Journal of the Minerals, Metals, and Materials Society*, vol. 41, no. 11, pp. 60–63, 1989.

[151] BENNET-CLARK, H. and LUCEY, E., "The jump of the flea: a study of the energetics and a model of the mechanism," *Journal of Experimental Biology*, vol. 47, no. 1, pp. 59–76, 1967.

[152] CLEMENTS, A., "The sources of energy for flight in mosquitoes," *Journal of Experimental Biology*, vol. 32, no. 3, pp. 547–554, 1955.

[153] WALKER, J., *The Flying Circus of Physics*. Wiley, 2007.

[154] HAUSER, D., AMAYENC, P., NUTTEN, B., and WALDTEUFEL, P., "A new optical instrument for simultaneous measurement of raindrop diameter and fall speed distributions," *Journal of Atmospheric and Oceanic Technology*, vol. 1, no. 3, pp. 256–269, 1984.

[155] MCDONALD, J. E., "Collection and washout of airborne pollens and spores by raindrops," *Science*, vol. 135, no. 3502, pp. 435–437, 1962.

[156] STAPP, J. P., "Effects of mechanical force on living tissues," *The Journal of aviation medicine*, vol. 26, no. 4, p. 268, 1955.

[157] PASANDIDEH-FARD, M., QIAO, Y., CHANDRA, S., and MOSTAGHIMI, J., "Capillary effects during droplet impact on a solid surface," *Physics of fluids*, vol. 8, p. 650, 1996.

[158] MUNDO, C., SOMMERFELD, M., and TROPEA, C., "Droplet-wall collisions: experimental studies of the deformation and breakup process," *International journal of multiphase flow*, vol. 21, no. 2, pp. 151–173, 1995.

[159] KELLER, J., "Teapot effect," *Journal of Applied Physics*, vol. 28, no. 8, pp. 859–864, 1957.

[160] DUEZ, C., YBERT, C., CLANET, C., and BOCQUET, L., "Beating the teapot effect," *arXiv preprint arXiv:0910.3306*, 2009.

[161] MCMAHON, T. and BONNER, J., *On size and life*. Scientific American Library New York, 1983.

[162] SCHMIDT-NIELSON, K., *Scaling*. Cambridge University Press, 1984.

[163] ELLINGTON, C., "Limitations on animal flight performance," *Journal of Experimental Biology*, vol. 160, no. 1, pp. 71–91, 1991.

[164] POVAROV, O., NAZAROV, O., IGNAT'EVSKAYA, L., and NIKOL'SKII, A., "Interaction of drops with boundary layer on rotating surface," *Journal of Engineering Physics and Thermophysics*, vol. 31, no. 6, pp. 1453–1456, 1976.

[165] "World malaria report : 2011," tech. rep., World Health Organization, 2011.

[166] PAAIJMANS, K. P. and THOMAS, M. B., "The influence of mosquito resting behaviour and associated microclimate for malaria risk," *Malaria Journal*, vol. 10, no. 1, p. 183, 2011.

[167] PANTALEONE, J. and MESSER, J., "The added mass of a spherical projectile," *American Journal of Physics*, vol. 79, no. 12, p. 1202, 2011.

[168] NALBACH, G. and HENGSTENBERG, R., "The halteres of the blowfly calliphora," *Journal of Comparative Physiology A: Neuroethology, Sensory, Neural, and Behavioral Physiology*, vol. 175, no. 6, pp. 695–708, 1994.

[169] OGATA, K., *System Dynamics*. Pearson Education Inc., 4 ed., 2004.

[170] NACHTIGALL, W. and WILSON, D. M., "Neuro-muscular control of dipteran flight," *Journal of Experimental Biology*, vol. 47, no. 1, pp. 77–97, 1967.

[171] TAYLOR, B., GREEN, J., and FARNDON, J., *The Big Bug Book: Discover the Amazing World of Beetles, Bugs, Butterflies, Moths, Insects and Spiders*. Lorenz Books, 2004.

[172] "Balance disorders," June 2010.

[173] OMAN, C. and YOUNG, L., "The physiological range of pressure difference and cupula deflections in the human semicircular canal: theoretical considerations," *Acta Oto-laryngologica*, vol. 74, no. 1-6, pp. 324–331, 1972.

[174] ALTSHULER, D. and DUDLEY, R., "The physiology and biomechanics of avian flight at high altitude," *Integrative and Comparative Biology*, vol. 46, no. 1, pp. 62–71, 2006.

[175] BUDDENBERG, J. and WILKE, C., "Calculation of gas mixture viscosities," *Industrial & Engineering Chemistry*, vol. 41, no. 7, pp. 1345–1347, 1949.

[176] HOBACK, W. W. and STANLEY, D. W., "Insects in hypoxia," *Journal of Insect Physiology*, vol. 47, no. 6, pp. 533–542, 2001.

[177] HOFFMANN, W. C., WALKER, T. W., FRITZ, B. K., FAROOQ, M., SMITH, V. L., ROBINSON, C. A., SZUMLAS, D., and LAN, Y., "Spray characterization of ultra-low-volume sprayers typically used in vector control 1," *Journal of the American Mosquito Control Association*, vol. 25, no. 3, pp. 332–337, 2009.

[178] ROMAN, B. and BICO, J., "Elasto-capillarity: deforming an elastic structure with a liquid droplet," *Journal of Physics: Condensed Matter*, vol. 22, no. 49, p. 493101, 2010.

[179] JOHNSON, L. and SCHOLZ, D., "On Steffensen's method," *SIAM Journal on Numerical Analysis*, vol. 5, no. 2, pp. 296–302, 1968.

[180] EARLS, K. D., "Kinematics and mechanics of ground take-off in the starling *sturnis vulgaris* and the quail *coturnix coturnix*," *Journal of Experimental Biology*, vol. 203, no. 4, pp. 725–739, 2000.

[181] KIM, H. and MAHADEVAN, L., "Capillary rise between elastic sheets," *Journal of Fluid Mechanics*, vol. 548, pp. 141–150, 2006.

[182] PY, C., BASTIEN, R., BICO, J., ROMAN, B., and BOUDAOUD, A., "3D aggregation of wet fibers," *EPL (Europhysics Letters)*, vol. 77, p. 44005, 2007.

[183] GILET, T., TERWAGNE, D., and VANDEWALLE, N., "Droplets sliding on fibres," *The European Physical Journal E*, vol. 31, no. 3, pp. 253–262, 2010.

[184] ZHAO, Y. and FAN, J., "Clusters of bundled nanorods in nanocarpet effect," *Applied physics letters*, vol. 88, no. 10, pp. 103123–103123, 2006.

[185] TEERINK, B., *Hair of West European mammals: atlas and identification key*. Cambridge University Press, 2004.

[186] KAMATH, Y., DANSIZER, C., and WEIGMANN, H., "Wetting behavior of human hair fibers," *Journal of Applied Polymer Science*, vol. 22, no. 8, pp. 2295–2306, 1978.

[187] LODGE, R. and BHUSHAN, B., "Wetting properties of human hair by means of dynamic contact angle measurement," *Journal of Applied Polymer Science*, vol. 102, no. 6, pp. 5255–5265, 2006.

[188] CARROLL, B., "Droplet formation and contact angles of liquids on mammalian hair fibres," *Journal of the Chemical Society, Faraday Transactions 1*, vol. 85, no. 11, pp. 3853–3860, 1989.

[189] CLANET, C. and LASHERAS, J., "Transition from dripping to jetting," *Journal of Fluid Mechanics*, vol. 383, pp. 307–326, 1999.

[190] MIDDLEMAN, S., *Modeling Axisymmetric Flows: Dynamics of Films, Jets, and Drops*. Academic Press San Diego, 1995.

[191] WALTON, W. and PREWETT, W., "The production of sprays and mists of uniform drop size by means of spinning disc type sprayers," *Proceedings of the Physical Society. Section B*, vol. 62, p. 341, 1949.

[192] DOMBROWSKI, N. and LLOYD, T., "Atomisation of liquids by spinning cups," *The Chemical Engineering Journal*, vol. 8, no. 1, pp. 63–81, 1974.

[193] TATE, T., "On the magnitude of a drop of liquid formed under different circumstances," *Philosophical Magazine Series 4*, vol. 27, no. 181, pp. 176–180, 1864.

[194] RAYLEIGH, L., "The principle of similitude," *Nature*, vol. 95, no. 2368, pp. 66–68, 1915.

[195] HARKINS, W. and BROWN, F., "The determination of surface tension (free surface energy), and the weight of falling drops: the surface tension of water and benzene by the capillary height method.," *Journal of the American Chemical Society*, vol. 41, no. 4, pp. 499–524, 1919.

[196] GROVES, C., "Pongo pygmaeus," *Mammalian species*, pp. 1–6, 1971.

[197] MECKLENBURG, L., LINEK, M., and TOBIN, D., *Hair Loss Disorders in Domestic Animals*. Wiley-Blackwell, 2009.

[198] SCOTT, D., MILLER, W., GRIFFIN, C., and OTHERS, *Muller and Kirk's small animal dermatology*. Saunders, 2001.

[199] SPOTORNO, A., ZULETA, C., VALLADARES, J., DEANE, A., and JIMÉNEZ, J., "Chinchilla laniger," *Mammalian Species*, pp. 1–9, 2004.

[200] WILCOX, H., "Histology of the skin and hair of the adult chinchilla," *The Anatomical Record*, vol. 108, no. 3, pp. 385–397, 1950.

[201] SKINNER, J. and CHIMIMBA, C., *The mammals of the southern African subregion*. Cambridge Univ Pr, 2005.

[202] FEDOSENKO, A. and BLANK, D., "Ovis ammon," *Mammalian Species*, pp. 1–15, 2005.

[203] WEINBERG, P., "Capra cylindricornis," *Mammalian Species*, 2009.

[204] CONLEY, K. and PORTER, W., "Heat loss from deer mice (Peromyscus): evaluation of seasonal limits to thermoregulation," *Journal of Experimental Biology*, vol. 126, no. 1, p. 249, 1986.

[205] CARRAWAY, L., ALEXANDER, L., and VERTS, B., "Scapanus townsendii," *Mammalian Species*, pp. 1–7, 1993.

[206] REAVILL, C., "Ovis aries," *University of Michigan. Museum of Zoology. Animal Diversity Web*, 2000.

[207] MILESKI, A. and MYERS, P., "Capra Hircus," *University of Michigan. Museum of Zoology. Animal Diversity Web*, 2004.

[208] LARIVIÈRE, S. and WALTON, L., "Lontra canadensis," *Mammalian Species*, no. 609, pp. 1–8, 1998.

[209] AUDET, A., ROBBINS, C., and LARIVIÈRE, S., "Alopex lagopus ," *Mammalian Species*, no. 713, pp. 1–10, 2002.

[210] TAYLOR, M., "Ichneumia albicauda," *Mammalian Species*, no. 12, pp. 1–4, 1972.

[211] SIDOROVICH, V., KRUUK, H., and MACDONALD, D., "Body size, and interactions between European and American mink (Mustela lutreola and M. vison) in Eastern Europe," *Journal of Zoology*, vol. 248, no. 4, pp. 521–527, 1999.

[212] VALENCAK, T., ARNOLD, W., TATARUCH, F., and RUF, T., "High content of polyunsaturated fatty acids in muscle phospholipids of a fast runner, the European brown hare (Lepus europaeus)," *Journal of Comparative Physiology B: Biochemical, Systemic, and Environmental Physiology*, vol. 173, no. 8, pp. 695–702, 2003.

[213] WILLNER, G., FELDHAMER, G., ZUCKER, E., and CHAPMAN, J., "Ondatra zibethicus," *Mammalian species*, no. 141, pp. 1–8, 1980.

[214] KREUTZER, J., "Mustela sibirica," *University of Michigan. Museum of Zoology. Animal Diversity Web*, 2003.

[215] OLSEN, P., "Water-rat hydromys chrysogaster," 1983.

[216] KING, C., "Mustela erminea," *Mammalian Species*, no. 195, pp. 1–8, 1983.

[217] PASS, D. and FREETH, G., "The rat," *Anzccart News*, vol. 6, no. 4, pp. 1–4, 1993.

[218] ÁLVAREZ-CASTAÑEDA, S. and CORTÉS-CALVA, P., "Peromyscus eva," *Mammalian species*, no. 738, pp. 1–3, 2003.

[219] FAHEY, B., "Neomys fodiens," *University of Michigan. Museum of Zoology. Animal Diversity Web*, 1999.

[220] MATTERN, M. and MCLENNAN, D., "Phylogeny and speciation of felids," *Cladistics*, vol. 16, no. 2, pp. 232–253, 2000.

[221] ESTES, J., "Enhydra lutris," *Mammalian Species*, no. 133, pp. 1–8, 1980.

[222] MCMANUS, J., "Didelphis virginiana," *Mammalian Species*, no. 40, pp. 1–6, 1974.

[223] JENKINS, S. and BUSHER, P., "Castor canadensis," *Mammalian Species*, no. 120, pp. 1–8, 1979.

[224] PASITSCHNIAK-ARTS, M. and MARINELLI, L., "Ornithorhynchus anatinus," *Mammalian Species*, no. 585, pp. 1–9, 1998.

[225] GIFFIN, J. and GORE, T., *Horse owner's veterinary handbook*. Howell Book House, 1989.

[226] TOMLINSON, J. and RIZY, T., "Measured impacts of high efficiency domestic clothes washers in a community," tech. rep., Oak Ridge National Lab., Energy Div., TN (United States), 1998.

[227] PRESTON, J., NIMAKAR, M., and GUNDAVDA, S., "Capillary and imbibed water in assemblies of moist fibres," *Textile Research Journal*, vol. 42, no. 3, pp. T79–T90, 1951.

[228] DENTON, M., "The extraction of water from cotton-yarn packages by centrifugal force. part i: spinning in a basket centrifuge," *Journal of the Textile Institute*, vol. 65, no. 8, pp. 409–415, 1974.

[229] WELO, L., ZIIFLE, H., and MCDONALD, A., "Swelling capacities of fibers in water. part ii: Centrifuge studies," *Textile Research Journal*, vol. 22, no. 4, pp. 261–273, 1952.

[230] CARTER, D., DRAPER, M., PETERSON, R., and SHAH, D., "Importance of dynamic surface tension to the residual water content of fabrics," *Langmuir*, vol. 21, no. 22, pp. 10106–10111, 2005.

[231] AHMED, A. and TAYLOR, N., "The analysis of drug-induced tremor in mice," *British Journal of Pharmacology and Chemotherapy*, vol. 14, no. 3, pp. 350–354, 1959.

[232] STAHL, W., "Scaling of respiratory variables in mammals," *Journal of Applied Physiology*, vol. 22, no. 3, pp. 453–460, 1967.

[233] CASEY, T., MAY, M., and MORGAN, K., "Flight energetics of euglossine bees in relation to morphology and wing stroke frequency," *Journal of Experimental Biology*, vol. 116, no. 1, p. 271, 1985.

[234] HEGLUND, N. and TAYLOR, C., "Speed, stride frequency and energy cost per stride: How do they change with body size and gait?," *The Journal of experimental biology*, vol. 138, pp. 301–318, 1988.

[235] REYNOLDS, P., "How big is a giant? the importance of method in estimating body size of extinct mammals," *Journal of Mammalogy*, vol. 83, no. 2, pp. 321–332, 2002.

[236] LEGENDRE, S. and ROTH, C., "Correlation of carnassial tooth size and body weight in recent carnivores (mammalia)," *Historical Biology*, vol. 1, no. 1, pp. 85–98, 1988.

VITA

Andrew K. Dickerson was born on May 29, 1987, and spent his first five years of life in Franklin, GA. He graduated from Carrollton High School in 2005 and spent the first two years of undergraduate study at the University of West Georgia. Coming to Georgia Tech as an E.E. student, Andrew quickly saw the light that is mechanical engineering. He graduated with a a B.S.M.E. from Georgia Tech in 2009, and immediately entered graduate school in pursuit of a Ph.D. In June of 2011, Andrew married Jaime Bruder. His first job will be with MPR Associates Inc. in Alexandria, VA.